University of Nevada, Reno

Active Faulting in the Central Walker Lane

A dissertation submitted in partial fulfillment of the requirements for the degree of Doctor of Philosophy in Geology

by

Ian K.D. Pierce

Dr. Steven G. Wesnousky/Dissertation Advisor

December, 2019

THE GRADUATE SCHOOL

We recommend that the dissertation
prepared under our supervision by

Ian K.D. Pierce

Entitled

Active Faulting in the Central Walker Lane

be accepted in partial fulfillment of the
requirements for the degree of

Doctor of Philosophy

Steven Wesnousky, Ph.D. , Advisor

Richard Koehler, Ph.D. , Committee Member

Ken Adams, Ph.D. , Committee Member

William Hammond, Ph.D. , Committee Member

Douglas Boyle, Ph.D. , Graduate School Representative

David W. Zeh, Ph.D., Dean, Graduate School

December-2019

Abstract

Geodetic studies show that ~7–8 mm/yr of right-lateral shear is accumulating across the Central Walker Lane in the absence of major through-going strike-slip faults. To better understand how this fault system accommodates this shear, the timing, rates, and patterns of active faults bounding and within the Walker Lake basin and Carson, Antelope, Smith, and Mason valleys in the western part of the Central Walker Lane are the focus of this dissertation.

The Carson Range fault system is composed of numerous shorter faults extending from Reno, NV to Markleeville, CA. The Carson City and Indian Hills faults are two splays of the Carson Range fault system near Carson City, NV. A trench across the Carson City fault revealed evidence of four earthquakes. Two trenches across the Indian Hills fault revealed evidence of two earthquakes. Combining these paleoseismic data with existing studies of regional faulting shows that the most recent earthquake to rupture the Genoa fault occurred ~516-450 cal yr BP, and likely also ruptured the faults in Carson Valley, but did not extend northwards through Washoe Valley and into Reno.

Lidar data and geomorphic mapping show geomorphic and geometric characteristics such as northwest oriented linear fault traces, up-hill facing scarps, and larger displacements in right-steps, consistent with the accommodation of northwest directed oblique-slip motion along the Wassuk and Smith Valley rangefront faults, while the Mason and Antelope valley rangefront faults appear to be primarily dip-slip. An active dextral strike-slip fault in the southernmost part of Mason Valley has likely produced earthquakes in the Holocene. Vertical displacement rates based on cosmogenic ages of alluvial fans displaced by range-bounding faults in Antelope, Smith, and Mason valleys are $0.5\ ^{+0.5}/_{-0.3}$, $0.5\ ^{+0.7}/_{-0.4}$, and $0.04\ ^{+0.05}/_{-0.03}$ mm/yr, respectively. The vertical rates correspond to dip-parallel slip rates of $0.6\ ^{+0.7}/_{-0.3}$, $0.7\ ^{+1.0}/_{-0.4}$, and <0.05 mm/yr, for the same three faults, respectively, assuming dips on each fault are 55 ± 10°. The along-strike distribution of scarp heights indicates that the most recent and penultimate earthquakes along the range bounding faults of Smith and Antelope valleys produced ~3 m vertical displacements during ~M_w 7 earthquakes. The pattern of faults described here forms a 200-km-long left-stepping en-echelon series of dextral, oblique, and normal faults extending from south of Walker Lake to north of Lake Tahoe, similar to observations of laboratory models of dextral shear.

Contents

List of Tables

List of Figures

Introduction

This dissertation presents the results of investigations of the rates and styles of faulting in the Walker Lane between Lake Tahoe and Walker Lake (**Figure 0.1**). The Walker Lane is a region of discontinuous faults that roughly follows the California-Nevada border from Southern California towards Susanville, CA. These faults accommodate ~20% of the 50 mm/yr of northwest directed dextral shear between the Pacific and North American plates. The Central Walker Lane interrupts the overall northwest grain of right-lateral faulting in the Walker Lane with a series of north-striking normal fault bounded basins and northeast striking left-lateral faults. The focus of this dissertation is on the region of normal fault bounded basins. High resolution topography, paleoseismic trenching, and cosmogenic and optically stimulated luminesence dating are used to study the rates, timing, and style of faulting in each of these basins.

The first chapter is a study of the frequency, recency, and size of prior earthquakes along the Carson Range fault system. Here trenches across the Carson City and Indian Hills faults reveal

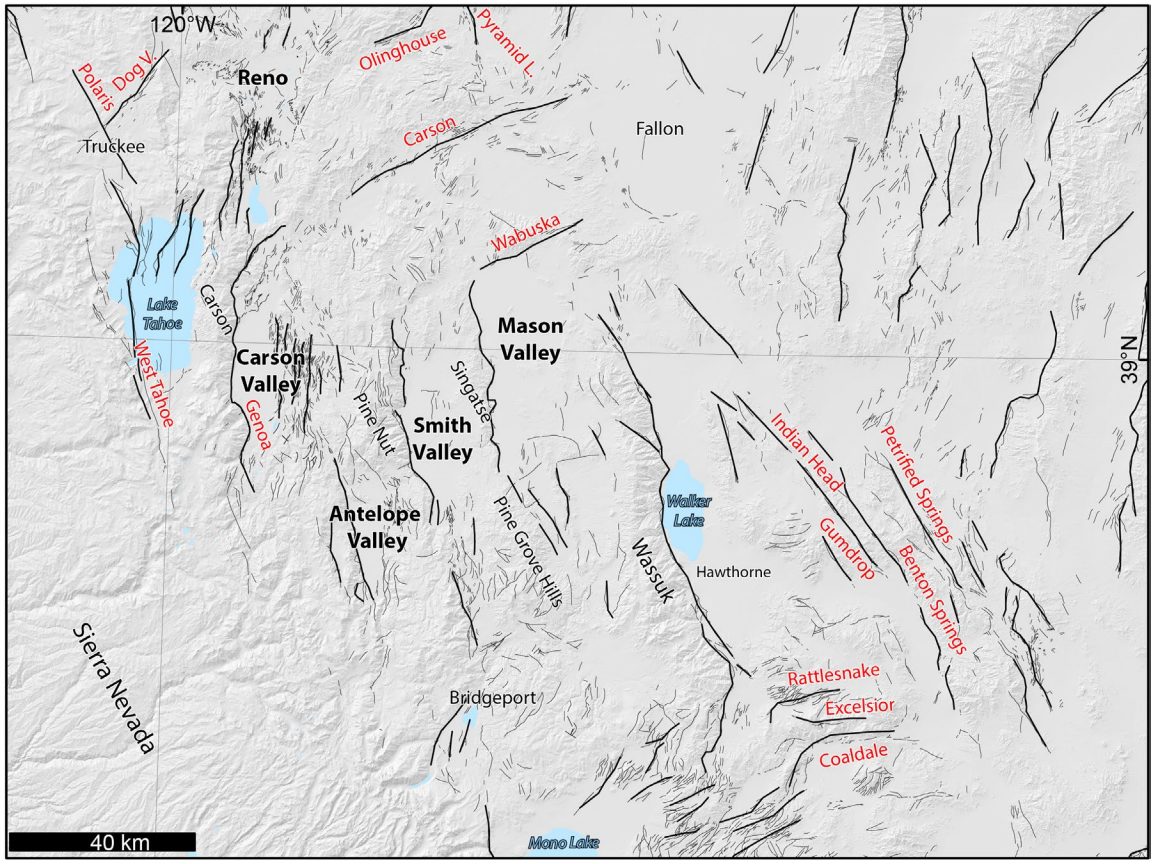

Figure 0.1 Overview map of the Central Walker Lane showing faults (black lines) and names of basins and ranges.

evidence of recent earthquakes that may have also ruptured the neighboring Genoa fault. Combined with the results of other studies, it does not seem likely that these earthquakes also ruptured the faults in Washoe Valley and Reno, placing an upper bound on the size of possible earthquakes that may be expected in the future. This chapter places limitations on multifault ruptures in the Central Walker Lane, which are discussed in more detail in the following chapter.

The second chapter examines how shear is accommodated in the absence of throughgoing strike-slip faults in the Central Walker Lane. Across the Central Walker Lane, 7-8 mm/yr of northwest directed dextral shear is observed, but there are no major strike-slip faults as in other parts of the Walker Lane. Slip rates are determined for the Antelope Valley, Smith Valley, and Mason Valley rangebounding faults. There is evidence of oblique slipping faults in Smith Valley and the Walker Lake basin. There is a strike-slip fault in southern Mason Valley along the Pine Grove Hills. Together these faults form a northwest trending pattern through this part of the Walker Lane composed of a series of short en-echelon strike- and oblique-slip faults, similar to laboratory models and other fault systems with limited total shear. With continued displacement, these faults may organize into a major through-going strike-slip fault.

Chapter I: Occurrence of large magnitude earthquakes and segmentation of the Carson Range fault system, Carson City, NV, USA

Abstract

The Carson City and Indian Hills faults are two splays of the Carson Range fault system near Carson City, Nevada. A trench across the Carson City fault revealed evidence of four earthquakes. Two trenches across the Indian Hills fault revealed evidence of two earthquakes. Combining these paleoseismic data with existing studies of regional faulting shows that the most recent earthquake to rupture the Genoa fault occurred ~516-450 cal yr BP, and likely only ruptured the faults in Carson Valley, not extending northwards through Washoe Valley and into Reno.

Introduction

Here, the goal is to present findings of paleoseismic trenching investigations of two faults within the Carson Range Fault System (CRFS): the Indian Hills and Carson City faults, and to place these findings into the broader context of the CRFS and Reno-Tahoe-Carson area by analyzing the rupture history of all regional faults using available prior paleoseismic studies. The CRFS is a system of east-dipping normal faults extending from Reno, NV nearly 100 km southwards to near Markleeville, CA (red faults in Figure 1.1). The CRFS spans the length of the Reno basin, Washoe Valley, and Carson Valley, and is composed of a number of different faults with lengths ranging from tens of meters to tens of kilometers. Lidar imagery reveal prominent and youthful (i.e. Holocene) fault scarps along the lengths of all the faults of the CRFS, however there are no records of historic surface rupturing earthquakes along this zone. A goal of this study is to examine how this fault system behaves during ruptures, as whether individual fault segments rupture randomly through time, cluster temporally, or rupture together as a single fault is unknown. Constraining the paleoseismic history of this fault system is important for placing bounds on the size and frequency of earthquakes that pose significant seismic hazards to the Reno-Tahoe-Carson urban area. Numerous paleoseismic studies (black dots in Figure 1.1) have been conducted to investigate the timing of these individual fault segments.

Regional Setting

The western Central Walker Lane (e.g. Wesnousky, 2005; Wesnousky et al., 2012; Bormann et al., 2016; Pierce, this dissertation) is to first order composed of a series of west tilted basins and ranges with east-dipping, predominantly normal faults along the western margins of basins. Figure 1.1 shows the westernmost set of these basins including the Reno, Truckee, and Lake Tahoe

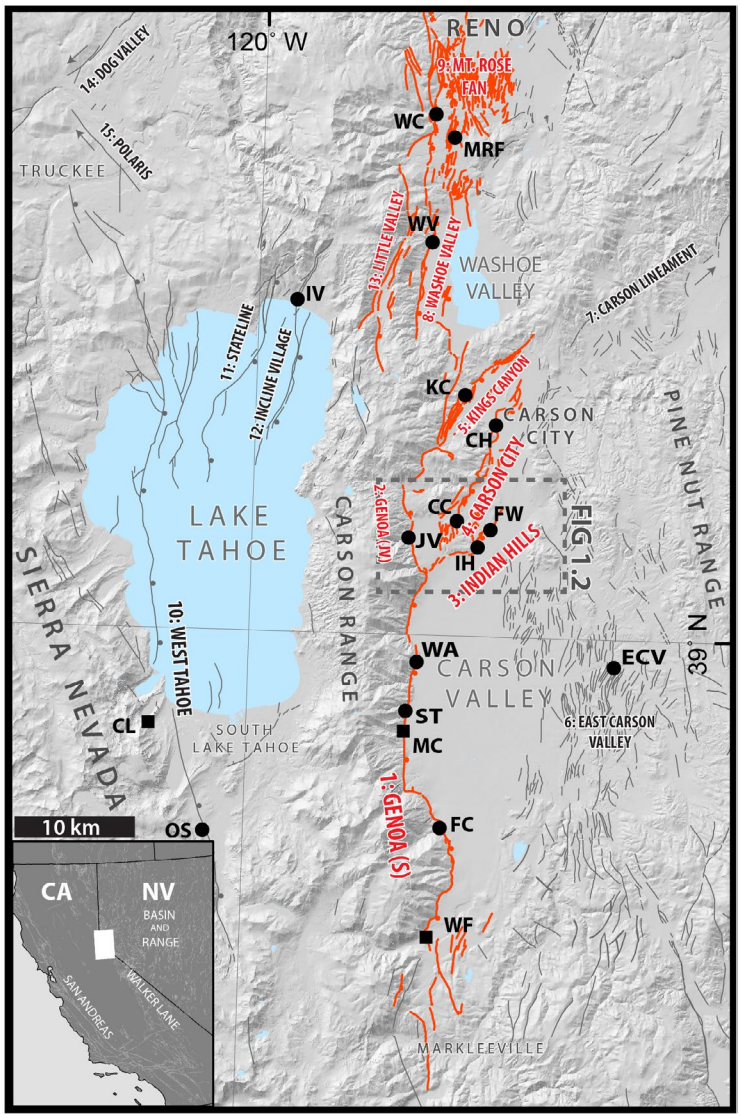

Figure 1.1 Overview map of the Carson Range Fault System (red) and surrounding region. Regional faults in gray modified from USGS Quaternary Fault and Fold Database. Abbreviations (see text for references): ECV (East Carson Valley), WF (Woodfords), FC (Fay Canyon), MC (Mott Canyon), ST (Sturgis), WA (Walleys), IH (Indian Hills), FW (Freeway), JV (Jacks Valley), CC (Carson City), KC (Kings Canyon), CH (C-Hill), WV (Washoe Valley), MRF (Mt. Rose Fan), WC (Whites Creek), IV (Incline Village), CL (Cascade Lake), OS (Osgood Swamp). Area of Figure 1.2 shown in inset map as dashed rectangle.

Fault #	Fault	Trench Sites		M_{Max} Wesnousky	M_{Max} Wells & Coppersmith	Closest neighbor (N)	Step size (N)	Closest neighbor (S)	Step size (S)
1	Genoa (S)	FC, ST, WA	43	6.9	7.0	Genoa (JV) & Indian Hills	0	-	-
2	Genoa (JV)	JV	7	6.5	6.0	Kings Canyon	0	Genoa (S)	0
3	Indian Hills	IH, FW	9	6.6	6.1	Carson City	0	Genoa (S)	0
4	Carson City	CC, CH	16	6.7	6.4	Kings Canyon	3	Indian Hills	0
5	Kings Canyon	KC	16	6.7	6.4	Washoe Valley	4	Genoa (JV)	0
6	East Carson	ECV	26	6.8	6.7	Indian Hills	3	-	0
7	Carson Lineament	-	50	6.9	7.1	-	-	Kings Canyon	5
8	Washoe Valley	WV	11	6.6	6.2	Mt Rose Fan	0	Kings Canyon	4
9	Mt. Rose Fan	MRF, WC	23	6.8	6.7	-	-	Washoe V. & Little V.	0
10	West Tahoe	OS	45	6.9	7.0	Stateline & Polaris	5 & 3	-	-
11	Stateline	-	19	6.7	6.5	Incline Village	2.5	West Tahoe	5
12	Incline Village	IV	20	6.7	6.6	Little Valley	5.5	Stateline	2.5

Table 1.1 Fault trains, trench sites, maximum magnitudes, and step over sizes to neighboring faults. Trench site locations shown on Figure 1.1.

basins, and Washoe and Carson valleys. The faulting within this region is generally composed of short (<50-km-long) discontinuous northwest striking dextral faults (e.g. Polaris fault; Hunter et al., 2011), northeast-striking sinistral faults (e.g. Carson lineament and Dog Valley fault; Li et al., 2017), and north striking primarily normal faults (e.g. Antelope Valley, Smith Valley, Genoa, and West Tahoe faults; Ramelli et al., 1999; Sarmiento et al., 2011; Wesnousky and Caffee, 2011; Pierce et al., 2017) (Figure 1.1).

Carson Valley (Figure 1.1) is a west-tilted half-graben (Cashman et al., 2009). The Genoa fault (e.g. Ramelli et al., 1999; Rood et al., 2011; Wesnousky et al., 2016) is the primary east-dipping normal fault separating the Carson Range from the western margin of Carson Valley. It strikes roughly north-south, extending for ~40 km from near Markleeville, CA towards Carson City, NV (Figure 1.1), and poses a significant seismic hazard to the state capital of Carson City. The late Quaternary slip rate of the Genoa fault is ~0.4-0.6 mm/yr based on the cosmogenic ages of displaced glacial landforms (Rood et al., 2011; Wesnousky et al., 2016).

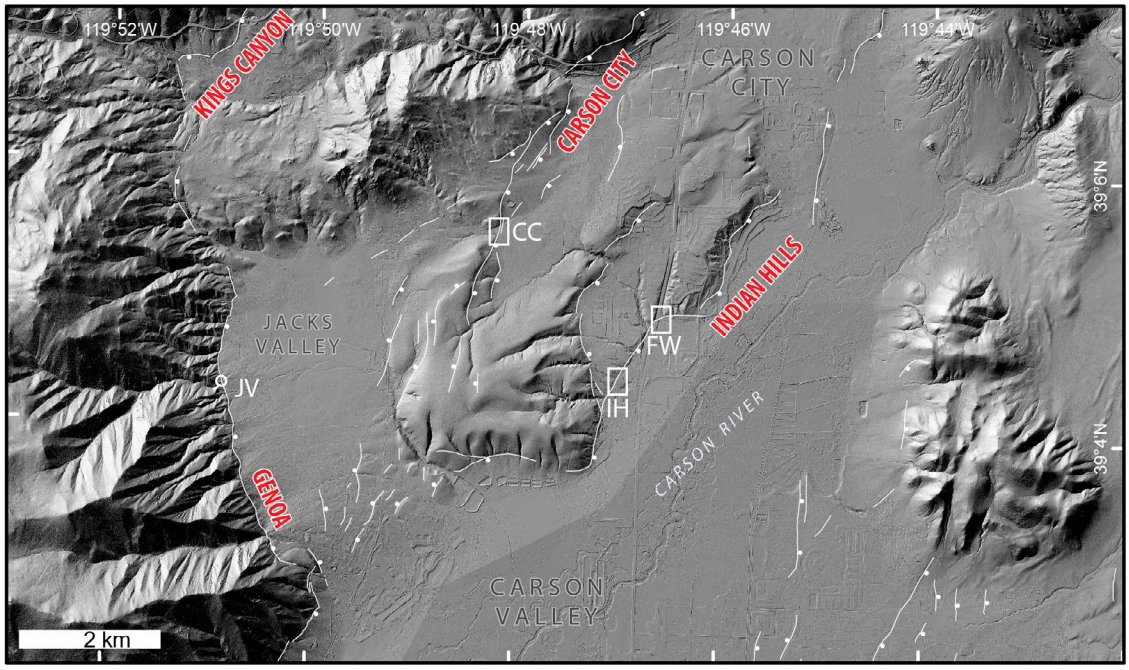

Figure 1.2 Lidar hillshade of the northern part of Carson Valley showing the Jacks Valley section of the Genoa fault, Indian Hills fault, and Carson City fault. Trench sites indicated by labeled circles. White lines are faults modified from the USGS Quaternary Fault and Fold Database, and white rectangles are extents of Figure 1.3.

Figure 1.3 Lidar hillshades of the three trench sites. Dotted white lines are faults, and white bars are approximate extents and orientation of the trenches. IH: Indian Hills site, FW: Freeway site, CC: Carson City site.

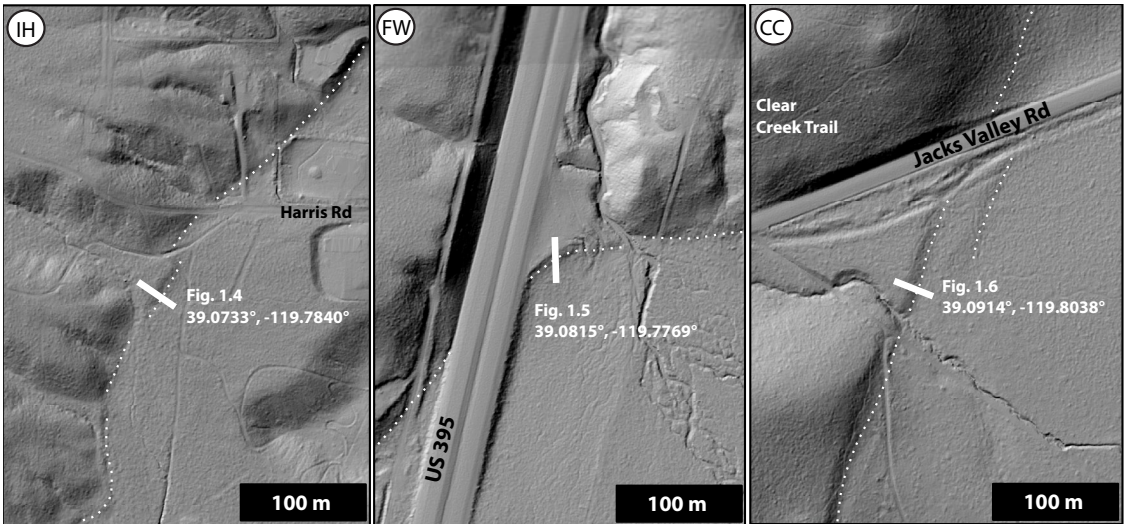

At the northern end of Carson Valley, the Genoa fault forms three major left-stepping splays, from northwest to southeast: the 16-km-long Kings Canyon fault (e.g. dePolo, 2014), the 16-km-long Carson City fault (this study), and the 9-km-long Indian Hills fault (this study). Both the Indian Hills and Carson City faults are separated from the Genoa fault by a <1 km wide step over (Figure 1.2). Each displays prominent southeast-facing scarps that cut young alluvial fan deposits. These scarps are similarly sharp and youthful as those along the Genoa fault. The most recent event (MRE) to rupture the Kings Canyon fault (dePolo, 2014) occurred about ~1800 cal. ybp, and therefore did not rupture during the ~300 cal. ybp MRE of the Genoa fault (Ramelli and Bell, 2009). The paleoseismic history of each of these faults is discussed in detail at the end of this chapter. Determining whether the Carson City and Indian Hills faults may have ruptured simultaneously with the MRE on the Genoa fault is a goal of this study.

Methods

Trench Excavations

Three trenches were excavated, cleaned, photographed, and logged using established paleoseismic methods (e.g. McCalpin, 2009). The logs were drafted on SfM photomosaics produced in Agisoft Photoscan using photos taken with a Pixel 2 cell phone following methods modified after Reitman et al. (2015). The photomosaics were scaled using scale bars placed on the trench walls. Units were divided based on color, composition (grain size, rounding, weathering, sorting, and stratification), interpretation of facies, and cross-cutting relations between stratigraphic deposits and faults. Faults were identified by juxtaposition of units and zones of aligned shears. Upward terminating faults, juxtaposed units, variations in displacements, cross-cutting relations, presence of fissures, and interpretations of scarp derived deposition were interpreted as evidence of past earthquakes.

Geochronology

To determine the ages of deposits, radiocarbon and optically stimulated luminescence (OSL) samples were collected. Where charcoal was able to be found in situ, samples were recovered, cleaned, weighed, and sent to Beta Analytics for analysis. The resulting radiocarbon ages are pend-

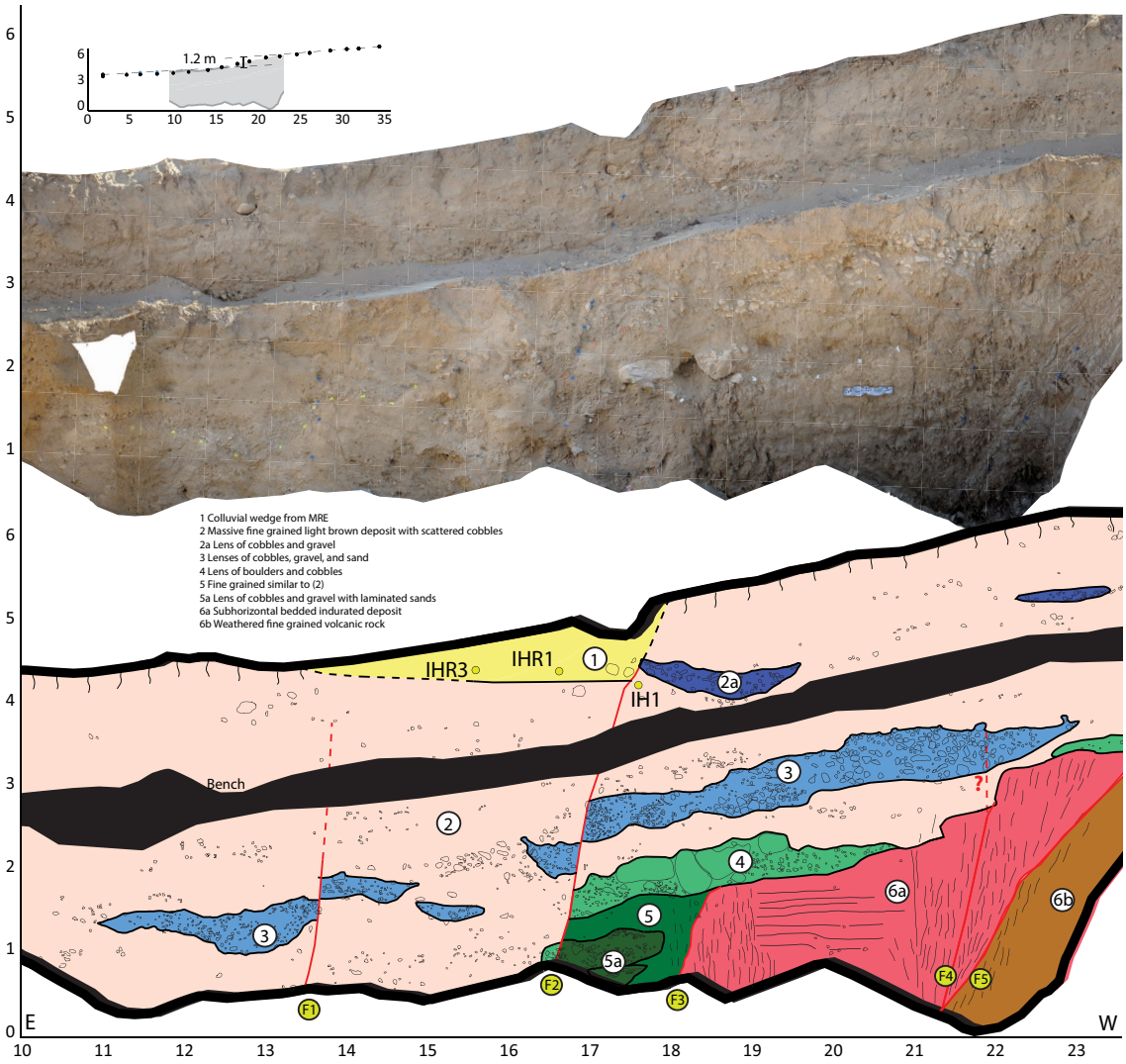

Figure 1.4 Trench log (lower) for the south wall of the Indian Hills site (IH). Upper is photomosaic. This trench is cut across a 1.2 m high fault scarp and contains evidence of at least two earthquakes. Topographic profile of the scarp shown above the trench log (gray shaded area shows extent of trench excavation).

ing. The arid environment and coarse grained alluvium common in these trenches are not ideal for preservation of charcoal, so OSL samples were taken where radiocarbon could not be located. Samples were collected by carefully cleaning the trench walls at the chosen sites, and then hammering in 2" diameter x 10" long opaque metal tubes into the wall. Each tube was then capped and sent to the OSL lab at UCLA for processing and analysis. The resulting ages are pending.

Observations

Indian Hills Trench

The Indian Hills trench (IH on Figures 1.1-1.3) is situated across a sharp, ~1.2-m-high fault scarp in a young alluvial fan along a northeast striking section of the Indian Hills fault (Figure 1.3). The trench (Figure 1.4) exposed a series of discontinuous faulted subhorizontal lenses of debris flows deposits. Units 6a and 6b are the oldest and are only exposed in the footwall at the bottom of the exposure. Unit 6a is an indurated fine grained deposit with subhorizontal tonal banding related to relic original bedding that is faulted by fault F5 (dip: 55°E) against unit 6b, a massive weathered igneous rock. Fault F4 (dip: 70°E) produces a 1 m wide shear zone within unit 6a, and based on a zone of vertically aligned loose cobbles above F4 within overlying unit 3, may extend upwards, however the upper and lower contacts of unit 3 are not displaced.

At the bottom of the trench, unit 6a is in faulted by F3 against units 5 and 5a. Units 5 and 5a are a small sheetwash deposit and lens of laminated fluvial sands and gravels, respectively. F3 (dip: 70°E) forms a ~1 m wide shear zone, and is buried by unit 4. Above unit 6 is a series of discontinuous faulted lenticular coarse debris flows deposits (units 3 & 4) within a weakly stratified silty matrix of sheetwash deposits (unit 2). Unit 3 is offset 30 and 40 cm by faults F1 (dip: 85°E) and F2 (dip: 75°E), respectively. Unit 2a is a small gravel and cobble lens towards the top of the exposure, which is truncated by fault F2. Near the central part of the scarp at the ground surface is unit 1, a dark colored, carbon rich, silty sand, that due to its wedge shape and concentration of cobbles at its base is interpreted to be a scarp derived colluvial deposit.

Interpretation

The stratigraphic and structural relations provide evidence of two earthquakes since the deposition of unit 5. The penultimate earthquake occurred prior to the deposition of units 3 and 4, and ruptured faults F3, F4, and F5. The most recent, scarp forming earthquake is interpreted to have ruptured faults F1 and F2, producing ~70 cm of total displacement. This earthquake occurred after the deposition of unit 2a, and produced the scarp that the colluvial wedge (unit 1) is deposited against.

Two charcoal samples were recovered from near the base of unit 1 (samples IHR1 and IHR3) for radiocarbon dating. Presuming that deposition of unit 1 occurred rapidly following the

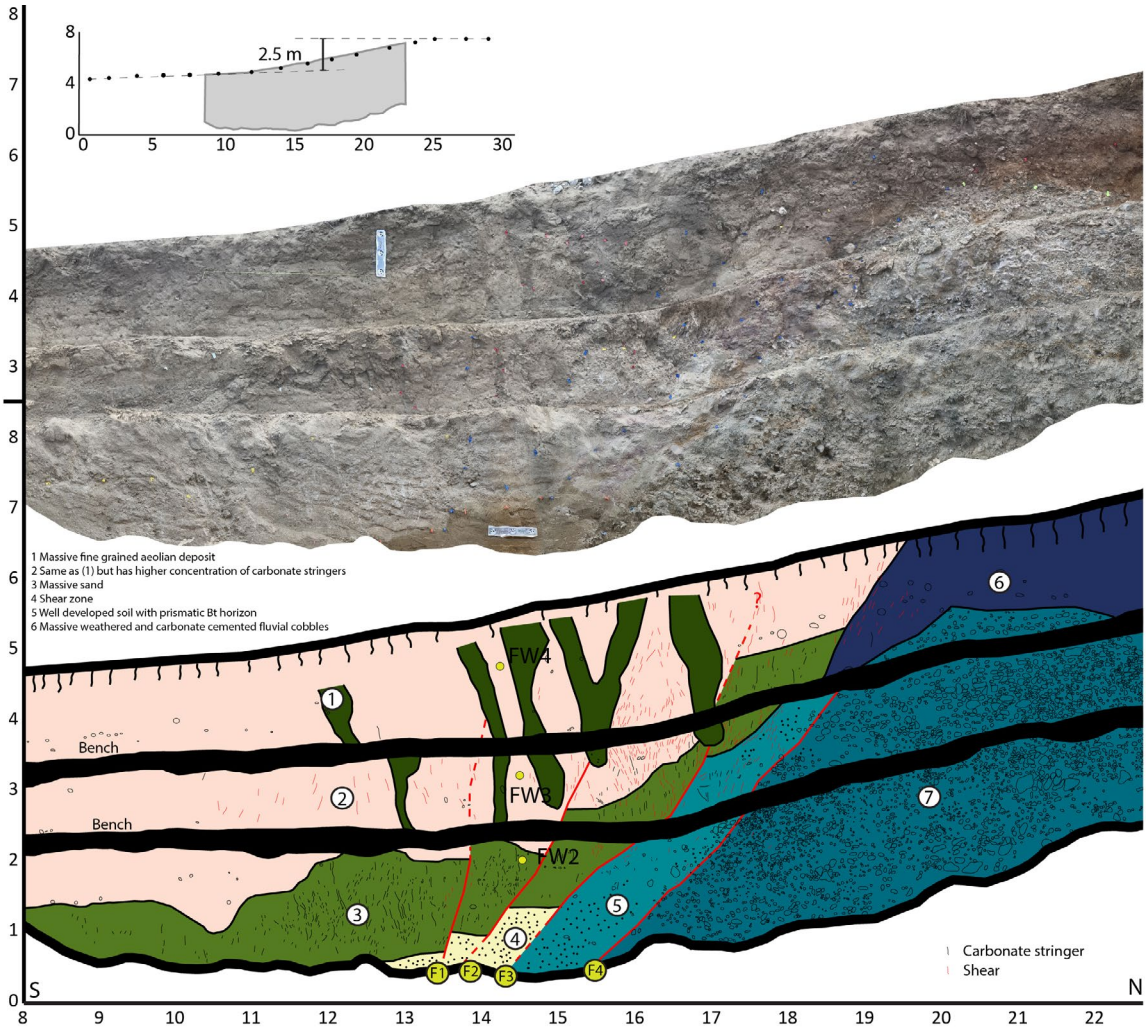

Figure 1.5 Trench log (lower) for the west wall of the Freeway site (FW). Upper is photomosaic. This trench is excavated across a 2.5 m high fault scarp and contains evidence of at least two earthquakes. Topographic profile of the scarp shown above the trench log (gray shaded area shows extent of trench excavation).

MRE, then these ages approximate the time of this earthquake. Two OSL samples (IH1 and IH3) were extracted from silty deposits near the upper portion of unit 2. IH1 was sampled just below unit 2a to ensure that it was from a faulted deposit, while IH3 was extracted from just below the surface soil in an exposure on the footwall fan tread ~10 m beyond the west edge of Figure 1.4. These two OSL samples are from near the top of the section of strata that were faulted during the MRE and thus provide a maximum limiting age on the MRE.

Freeway Trench

The freeway trench (FW on Figures 1.1-1.3) was excavated across a ~2.5 m high east-northeast trending scarp cut by the Indian Hills fault in an alluvial fan close to the Carson River (Figure 1.2). This trench (Figure 1.5) exposed a broad shear zone that juxtaposes young aeolian silt and fluvial sand deposits against fluvial cobbles. There is no correlation of units across this shear zone. The oldest unit exposed in the trench is unit 7, which makes up the majority of the footwall of the fault. Unit 7 consists of massive, highly weathered, grussified, stage 4 carbonate cemented rounded fluvial cobbles that range in size from ~5-20 cm. Above unit 7 on the footwall is a sharp contact with unit 6. Unit 6 is composed of a thick clay rich Bt horizon that breaks apart into ~10 cm long prismatic peds. The degree of weathering and carbonate cementation in unit 7, and the development of the capping soil (unit 6) are consistent with a mid-Pleistocene age (Birkeland, 1984).

Separating the deposits on the lower portion of the hanging wall from the footwall are faults F3 and F4, which bound unit 5, a ~1 m wide, 45° south dipping shear zone of jumbled packages of stratified sands, cobbles, and clay that do not clearly match any of the units exposed in the trench. The oldest unit exposed at the bottom of the hanging wall is unit 4, which is a massive sandy deposit. The upper contact of unit 4 with unit 3 is offset by 30 and 50 cm by faults F1 (dip: 75°S) and F2 (dip: 50°S), respectively. Above unit 4 are units 2 and 3: medium brown, massive, unstratified silty deposits with scattered gravel and cobbles, interpreted to be aeolian/loess deposits that were deposited against a pre-existing scarp. Distinguishing unit 3 from unit 2 is the presence of a significant amount of white carbonate stringers. The contact between units 2 and 3 is undulating, and offset 70 and 115 cm by faults F2 and F3, respectively. Within unit 2 are a series of prominent dark brown fissures (unit 1) that extend close to the ground surface and are filled by fine grained carbon rich silt, similar to the modern soil. These fissures are formed above faults F1-F3. Capping all the exposed units is a thin (~5-10 cm), gray, silty Av horizon.

Interpretation

Evidence of two earthquakes is preserved in the trench. The unit 2-3 contact is interpreted to be the event horizon of a penultimate earthquake because the carbonate stringers in unit 3 are taken as evidence of a fracturing event that occurred prior to deposition of unit 2. The most recent earthquake ruptured faults F1-F3, displacing the unit 2-3 and 3-4 contacts, and producing the fis-

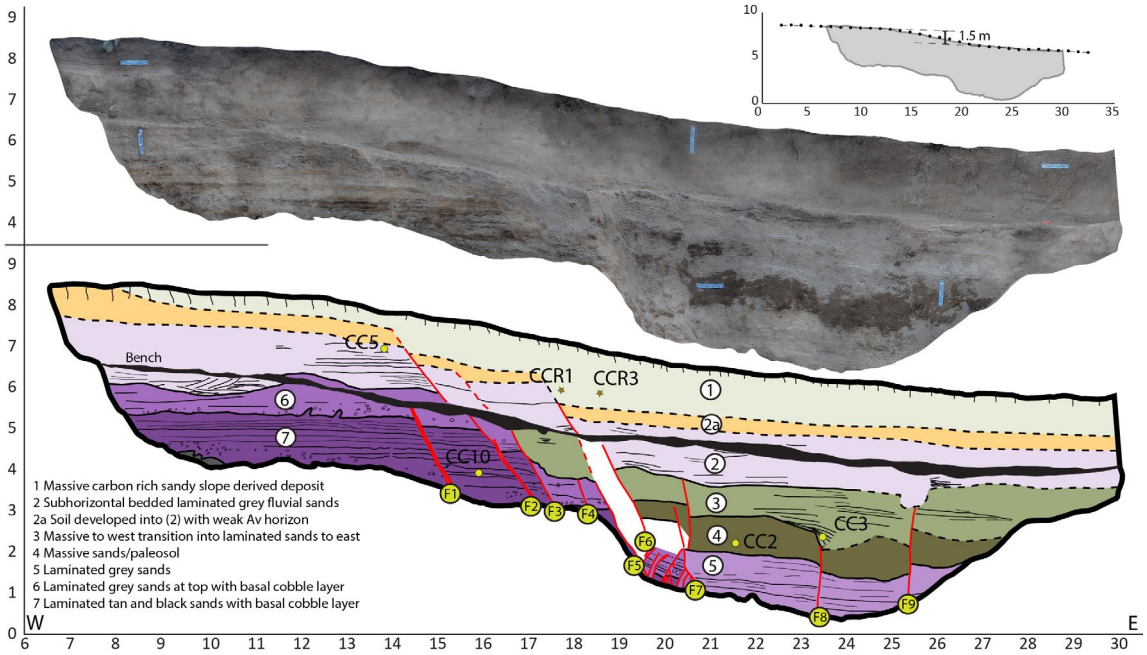

Figure 1.6 Trench log (lower) for the north wall of the Carson City site (CC). Upper is photomosaic. This trench is excavated across a 1.5 m high scarp and contains evidence of at least 3 earthquakes. Topographic profile of the scarp shown above the trench log (gray shaded area shows extent of trench excavation).

sures in unit 2.

Two charcoal samples were recovered from the lower portions of fissures in the hanging wall for radiocarbon dating (FWR-5 and FWR-7). If it is presumed that these fissures were rapidly filled following the MRE, then these ages approximate the timing of this event. A profile of three OSL samples (FW2-4 from bottom to top) were collected from units 2 and 3. FW4 was sampled from unit 2 just outside the top of one of the unit 1 fissures, and therefore is a maximum age of the MRE. FW2 and FW3 are below and above the penultimate event horizon (unit 2-3 contact) and therefore bracket the age of the penultimate earthquake.

Carson City Fault

The trench across the Carson City fault (CC in Figures 1.1-1.3) is located just south of Jacks Valley road near the Clear Creek trailhead (Figure 1.3). Here a small creek has cut a notch in the rangefront and a ~1.5 m east facing scarp is preserved in alluvium. The trench (Figure 1.6) is primarily composed of well sorted laminated fluvial sands cut by a series of east dipping faults. At the bottom of the footwall on the west side of the trench are the oldest units 6 and 7. These units both

consist of a basal gravel layer that grades upward into thinly bedded yellow/tan fine and medium fluvial sands with distinct dark manganese laminae. The contact between units 6 and 7 is faulted 30, 80, 150, and 180 cm by faults F1, F2, F3 and F5/6, respectively, for a total of 450 cm down-dip displacement across the series of ~50-60° east-dipping faults. As units 6 and 7 cannot be traced across F7, additional displacement across fault F7 may be buried in the hanging wall of the trench, and thus this number represents a minimum of total displacement since the deposition of unit 6. Faults 5 and 6 are the same fault, but due to an eastern widening of the trench at F5 created during excavation, appear as separate faults in the lower part of the wall.

A sequence of sandy deposits is exposed in the hanging wall. Unit 5 is exposed at the base of the section and consists of gray medium grained laminated fluvial sands. Unit 4 overlies unit 5 and is a dark gray massive sand that is sharply juxtaposed against unit 6 along faults F5/6 and F7. Unit 4 is buried by unit 3 which transitions eastward from massive gray sands near faults F3-7 to thinly laminated fine to medium grained sands near the eastern edge of the trench. This transition is interpreted to represent a facies change from scarp-derived into fluvial deposition away from the scarp. As both unit 4 and the massive portion of unit 3 are unstratified and adjacent to faults F5/6 and F7, they are interpreted to be scarp derived deposits. Fault F8 cuts units 5 and 4 but does not extend into unit 3, while fault F9 antithetically cuts units 3, 4, and 5.

Deposits exposed in the footwall and hanging wall are overlain by unit 2, which is a laminated light gray sand that is locally cross bedded. The sub-horizontal bedding in unit 2 that extends across both the hanging wall and footwall is consistent with low energy fluvial deposition across a relatively flat surface, and thus it is interpreted that unit 2 planed off any prior fault scarp. Unit 2a is a massive bioturbated sand, interpreted as the soil developed into unit 2 prior to the most recent faulting event. The top of unit 2 is displaced ~85, 45, and 105 cm (total: 235 cm) by faults F2, F3, and F5/6. Unit 1 caps the exposure and consists of massive dark sand with disseminated charcoal that thickens on the hanging wall, consistent with a scarp derived origin. The soil developed into unit 1 is weakly developed with a thin Av horizon. In sum, the stratigraphy in the trench is composed of well-sorted low-energy fluvial sands interrupted by a series of massive scarp derived deposits/ buried soils.

Interpretation

Based on juxtaposition of units, cross cutting relations, and buried soils, the exposure records evidence of at least three earthquakes. As unit 4 is only in the hanging wall and is massive adjacent to fault F5/6, it is interpreted to be the scarp derived deposit from the antepenultimate earthquake. The penultimate earthquake ruptured fault F8, forming a graben-like-structure in the top of unit 4, and F3, which formed a scarp that unit 3 was deposited against. This buried graben above F8 is infilled by a gravel deposit and laminated sands that produce a clinoform structure at the base of unit 3, and thus unit 3 postdates the faulting event along fault F8. Unit 2 then planed off the fault scarp before its upper contact was displaced ~235 cm of displacement along faults F2, F3, and F5/6 during the MRE. Unit 1 was then deposited across this scarp.

Two charcoal samples (CCR1 & CCR3) were collected from the base of unit 1 in the hangingwall of fault F5/6. As it is presumed that unit 1 was deposited shortly following the MRE, the radiocarbon ages of these samples approximate the time of the earthquake. OSL sample CC5 was extracted from near the top of unit 2 and therefore predates the MRE. OSL was also sampled from the base of the graben in unit 3 above fault F8 (CC3) and from unit 4 (CC2). These ages bracket the age of the penultimate earthquake. As unit 4 is interpreted to be a scarp derived deposit from the antepenultimate earthquake, CC2 is younger than this event, while OSL sample CC10, taken from unit 7, predates this event.

Event Timing of the Indian Hills and Carson City faults

All three trenches excavated for this study contain evidence of Holocene earthquakes. Both trenches excavated across the Indian Hills fault have evidence of the most recent earthquake occurring without significant subsequent soil development, suggesting that faulting occurred sometime in the last several millennia. The trench across the Carson City fault contains evidence of a youthful event (MRE) and at least two penultimate events. The MRE on the Carson City fault also occurred in the late Holocene based on the sharpness of the scarp and lack of soil development.

Reevaluation of past paleoseismic studies of the Carson Range fault system

In order place the results from the CC, IH, and FW trenches into context with the rest of the CRFS, I first standardize the timing of events across the CRFS by using OxCal (Bronk Ramsey, 1995;

Fault	Site	Abbreviation	Study	n	MRE Interval	PE Interval
Antelope Valley	Antelope Valley	AV	Sarmiento et al. 2011	2	1403-100	10415-6214
Smith Valley	Smith Valley	CR	Wesnousky & Caffee 2011	2	5926-3818	-
Genoa (S)	Fay Canyon	FC	Ramelli and Bell 2009	17	538-511	2387-2020
Genoa (S)	Sturgis	ST	Ramelli et al., 1999a	7	1435-694	2553-1804
Genoa (S)	Walleys	WA	Ramelli et al., 1999a	2	444-100	
East Carson Valley	ECVF	ECV	dePolo & Sawyer 2005	2	854-572	-
Genoa (Jacks Valley)	Jacks Valley	JV	Ramelli et al., 1999a	8	696-427	2749-1692
Indian Hillls	Indian Hills	IH	this study	4		
Indian Hills	Freeway	FW	this study	5		
Carson City	Carson City	CC	this study	6		
Carson City	C-Hill	CH	Ramelli et al., 1999b	3	2658-450	
Kings Canyon	Kings Canyon t2	KC2	dePolo 2014	4	3749-1643	

Table 1.2 List of trench sites, respective references, number of ages from each trench (n), and calculated MRE and PE intervals based on reevaluating the data from each trench with OxCal.

Lienkaemper and Ramsey, 2009) to reanalyze the ages reported in available paleoseismic studies. The OxCal formatted age data used to constrain the timing of the MRE and PE(s) at each site are listed in the Appendix, and the results for each trench site are listed in Table 1.2. In the following sections I describe the prior and reevaluated paleoseismic interpretations for each fault.

Genoa

Ramelli et al.'s (1999) study of the stratigraphic and structural relations exposed in the Sturgis (ST), Walleys (WA), and Jacks Valley (JV) trenches determined that two events ruptured the entirety of the Genoa fault with displacements on the order of 3-5.5 m per event at 500-600 cal yr BP and 2000-2200 cal yr BP. With the analysis of two additional trenches at Fay Canyon (FC), Ramelli and Bell (2009) revise the timing of the MRE and PE to ~300 and ~1740 cal yr BP, respectively.

The only two radiocarbon ages from the WA trench (Ramelli et al., 1999) can be omitted as they are reported to be burned roots, removing any bounds this site places on event timing. In order

for the MRE to have ruptured from JV to FC requires that both post-MRE ages (samples ST-3 and ST-5) at the intervening Sturgis site (ST- Ramelli et al., 1999) be omitted from modeling. Sample ST-3 is suggested to be reworked by the authors (Ramelli et al., 1999), but there is no justification to remove ST-5. From the FC trenches (Ramelli and Bell, 2009), sample Fl1-26 is omitted as it is out of chronological order. Omitting these ages results in an MRE (~516-427 cal yr BP) and PE (~2553-1804 cal yr BP) that could have ruptured the entire Genoa fault (faults 1 & 2 in Figure 1.1 and Table 1.1).

Carson City

A single trench was excavated at the C-Hill (CH) site by Ramelli et al. (1999). The two interpreted events at this site are bracketed by 2 radiocarbon ages. The youngest detrital charcoal sample was taken from a fissure produced by the MRE and interpreted to approximate the MRE at ~474 cal yr BP. The older (~2750 cal yr BP) sample was taken from alluvium that was deposited prior to the PE at this site.

As there are no intervening ages between the PE and MRE at this site, OxCal models two events that occurred anytime between 2658 and 450 cal yr BP. If the PE is thought to have occurred relatively shortly after the deposition of the older sample, and the MRE shortly before the young sample, then these events occurred at roughly the same time as both events along the Genoa fault.

Kings Canyon

dePolo (2014) excavated three trenches on the Kings Canyon fault (KC on Figure 1.1). Based on a series of colluvial deposits exposed in Trench 3 he considers two-, three-, and four- event models. Despite describing the three-event model as the "model of least astonishment," he only reports the event intervals of the four-event model (and only using ages from Trench 3), which are ~1420, 1630, 1820, and 3960 cal yr BP.

Here the ages from Trenches 2 and 3 are modeled separately, as the stratigraphic relations between the ages from the two trenches are not clear from the report. Modeling the ages from Trench 2 results in an MRE of 3749-1643 cal yr BP. Using a three-event model for Trench 3 results in an antepenultimate, PE, and MRE of 4918-3000, 1790-1550, and 1519-1387 cal yr BP, respectively. All of these events are much older than the MRE of the Genoa fault, however the PE in Trench 3 and

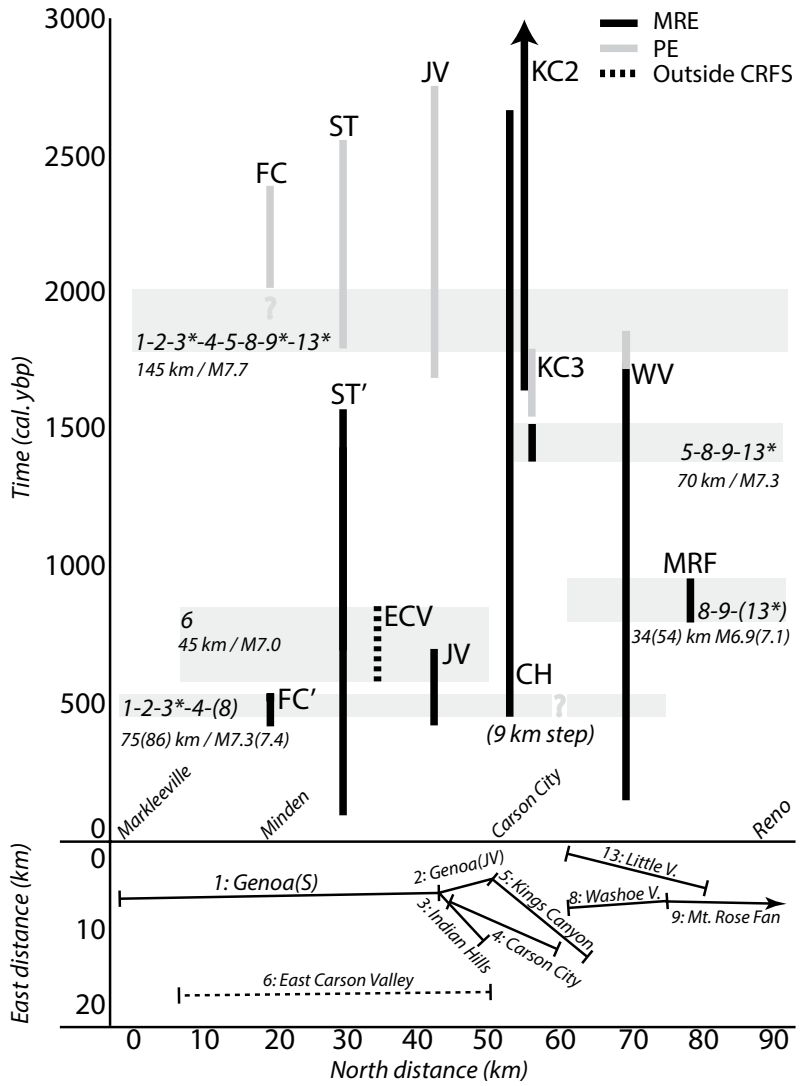

Figure 1.7 Top: Space time diagram combining event horizons calculated from all known paleoseismic studies in the CRFS. See text and tables for source data. ECV: East Carson Valley, FC: Fay Canyon (Genoa), ST: Sturgis (Genoa), WA: Walleys (Genoa), JV: Jacks Valley, CH: C-Hill (Carson City), KC: Kings Canyon, WV: Washoe Valley, MRF: Mt. Rose Fan. *indicates no age constraint. ‘ indicates ages were omitted. Bottom: simplified fault pattern of the CRFS showing fault numbers, names, and geometry.

the MRE in Trench 2 are similar to the age of the Genoa fault's PE.

Washoe Valley

Two trenches were excavated by Ramelli and dePolo (1996) in Washoe Valley. The first trench (DCP-1 in their text or WV on Figure 1.1) revealed evidence of two events in the last 1700 years, however they were unable to better bracket the event timing. The one reported inter-event sample produced a radiocarbon age older than the underlying samples. The second trench did not

reveal any useful data.

If the samples are assumed to be in proper stratigraphic order and as OxCal uses calibrated radiocarbon ages in its modeling of event horizons, the inter-event sample provides constraint on the event timing, This results in a PE and MRE of 1860-1721, and 1742-present cal. ybp, respectively. These are also similar to those of the two events on the Genoa fault.

Mt. Rose Fan

Several trenching studies have unsuccessfully tried to determine event timing of the range bounding fault near Mt. Rose (WC on Figure 1.1 Ramelli et al., 1999; Sarmiento et al., 2011). Bell et al. (1984) recovered a single pre-MRE radiocarbon sample with an age of ~1000 years from a trench at Whites Creek (WC on Figure 1.1). Ramelli et al. (2007) report two ~1000 year ages of samples recovered from fissure fill in consultant trenches excavated across scarps in the Mt. Rose Fan (MRF on Figure 1.1).

If it is assumed that the faults trenched at the WC and MRF sites ruptured simultaneously, then the three ages produce a model with a tight bracket of 955-797 cal. ybp for the MRE on the MRF. Otherwise the time of the MRE on the MRF should be close in age to the fissure fill, or similarly ~1000 ybp. Either result is considerably older than the MRE on the Genoa fault, but may overlap with the MRE in Washoe Valley. Additional trenching should be undertaken in the Mt. Rose Fan to better constrain the event history.

Discussion

Multi-fault ruptures in the Carson Range fault system

While individual lengths of mapped faults may be short, and only capable of sustaining moderate earthquakes, several faults rupturing simultaneously can generate destructive large magnitude earthquakes. Understanding rupture boundaries of faults and whether earthquakes are able to cross them is necessary for determining the length of possible ruptures and potential maximum magnitudes. Historic earthquakes like the 2019 Ridgecrest sequence (Ross et al., 2019), 2008 Wenchuan earthquake (Shen et al., 2009), 1987 Superstition Hills sequence (Hudnut et al., 1989), and the 1934 Cedar Mountain earthquake (Bell et al., 1999) demonstrate that ruptures frequently propagate over multiple faults. The region surrounding the CRFS contains dozens of

closely spaced Quaternary faults (Figure 1.1), yet none have ruptured the ground surface during historic times.

Earthquake ruptures often terminate at structural complexities such as stepovers (Biasi and Wesnousky, 2016), bends (Elliott et al., 2015), asperities (King, 1986), or changes in geometric pattern (Zhang et al., 1991). Biasi and Wesnousky (2016) measured the lengths of stepovers of historical surface ruptures and found that of all 76 ruptures investigated, few ruptures were able to propagate through stepovers > ~6 km. If these terminations form persistent boundaries (i.e. over many earthquake cycles), then for normal faults where displacements commonly taper towards rupture ends (Wilkinson et al., 2014), a repeated slip deficit at a boundary will result in lesser structural relief, and over time produce a bedrock ridge (Wheeler, 1989). In the CRFS, such boundaries may have produced the topographic highs separating the Reno basin from Washoe Valley, and Washoe Valley from Carson Valley. However, verification of the persistence of a rupture boundary for a given fault system requires paleoseismic sites that span multiple earthquake cycles located on both sides of the boundary. Recent work shows that rupture boundaries along the Wasatch range may be non-persistent (Bennett et al., 2015).

To test the presence of rupture boundaries in the CRFS, I combine all known and available paleoseismic data from prior trenches (Table 1.2) along the CRFS in a space-time diagram (Figure 1.7) to show the occurrence of earthquakes along the average northerly strike. The resulting constraints on event timing are not of sufficient resolution to differentiate whether ruptures of multiple faults were simultaneous during single catastrophic events or if earthquakes occurred on neighboring faults over a period of time that could be as long as several centuries, but for the following analyses are considered singular events if (1) the event timing overlaps and (2) the stepover size between neighboring faults is <6 km (Biasi and Wesnousky, 2016).

In Table 1.1 are listed the mapped lengths of all of the labeled faults from Figure 1.1, their expected M_{Max} (calculated using both the regressions with fault length for normal faults of Wesnousky (2008) and Wells and Coppersmith (1994)), and the closest northerly and southerly neighboring faults and corresponding step sizes (to the nearest 0.5 km). The predicted magnitudes from Wells and Coppersmith (1994) are approximately M0.1-0.6 greater than those using the regression of Wesnousky (2008) for the lengths of faults used in this study. For this analysis the Mt. Rose

fan (MRF) and Eastern Carson Valley fault zones (ECV) are both treated as singular faults with lengths equivalent to the north-south length of the respective fault zones, rather than summing their individual scarp lengths. To simplify the analysis the Genoa fault is broken into two segments: a southern segment (Genoa S) and a Jacks Valley segment (Genoa JV) as this segment boundary is a geometric complexity where the IH and CC faults diverge from the main Genoa fault (Figure 1.2).

The timing of the MRE overlaps from ~516-450 cal yr BP for the southern Genoa, JV, Indian Hills (IH), Carson City (CC), and Washoe Valley (WV) faults, but does not overlap with the 1519-1387 cal yr BP MRE of the Kings Canyon (KC) fault (dePolo, 2014). To pass over the KC fault this 86-km-long rupture would have required a stepover of ~9 km, which is the very upper limit of historic precedent (Biasi and Wesnousky, 2016). Thus the KC fault likely formed a rupture boundary during the MRE of the CRFS.

If the KC fault formed a rupture boundary during the MRE of the CRFS, then the southern faults (Genoa, JV, CC, IH) could have produced a 75-km-long M7.0-7.3. The event timing at the Washoe Valley (WV) site overlaps from 955-797 cal yr BP with the Mt. Rose Fan (MRF) and would result in a ~35 km long M6.8-6.9 rupture, or as much as M7.1 were the 20-km-long Little Valley fault to rupture simultaneously (the Little Valley fault currently lacks event age constraints).

While the results of DePolo (2014) show that the KC fault did not rupture with the southern Genoa fault during the Genoa fault's ~500 cal yr BP MRE, the timing of the MRE for the KC fault does overlap with the timing of the PE on the WV, CC, and Genoa faults (~1800 cal yr BP), allowing that a full >100-km-long M7.5+ may have ruptured the CRFS in the past.

In sum, large M7+ events ruptured the faults in Carson Valley ~516-450 cal yr BP., and ~1800-2000 cal yr BP. The recurrence time of large events on each segment of the CRFS is thus on the order of ~1500 years. The timing of the MRE on the East Carson Valley fault zone (854-572 cal yr BP) is close to the timing of this MRE on the CRFS, allowing that there could have been a temporal cluster of earthquakes in this region during the last earthquake cycle ~500 cal yr BP. Future studies should focus on faults that lack age data, especially in Little Valley and the Mt. Rose Fan.

Conclusion

The three trenches reveal evidence of multiple late Holocene earthquakes on both the Carson City and Indian Hills faults near Carson City, NV, similar to trenches of the Genoa fault. Combined with the results of previous studies there are now constraints on the timing of past earthquakes along much of the Carson Range fault system. The most recent event likely ruptured the Genoa, Indian Hills, and Carson City faults and occurred ~516-450 cal yr BP, while the MRE on the Washoe Valley and Mt. Rose Fan faults ruptured earlier (955-797 cal yr BP). The East Carson Valley fault zone ruptured 854-572 cal yr BP. The penultimate earthquake may have ruptured the full >100-km-long CRFS with a ~M7.5 event ~1800 cal yr BP.

Acknowledgements

The author would like to thank James "CJ" McNeil, Annie Kell, Scott Feehan, and Connie De Masi for help cleaning and logging the trenches. Special thanks to Rich Koehler, Seth Dee, and Craig dePolo for useful discussions in the field and lab. Marty Banta provided excellent help excavating the trench, and Dave Risley facilitated the permitting process. Additional thanks to the US Forest Service and Washoe Tribe for allowing access to their lands. USGS Award G19AP00044. Center for Neotectonic Studies contribution no. 79.

References

Bell, J.W., dePolo, C.M., Ramelli, A.R., Sarna-Wojcicki, A.M., Meyer, C.E., 1999. Surface faulting and paleoseismic history of the 1932 Cedar Mountain earthquake area, west-central Nevada, and implications for modern tectonics of the Walker Lane. Geological Society of America Bulletin 111, 791–807. https://doi.org/10.1130/0016-7606(1999)111<0791:SFAPHO>2.3.CO;2

Bell, J.W., Slemmons, D.B., Wallace, R.A., 1984. Reno to Dixie Valley—Fairview Peak earthquake areas, in: Western Geological Excursions. pp. 425–472.

Bennett, S., Gold, R., DuRoss, C., 2015. Evidence for Non-Persistent Rupture Terminations at Central Wasatch Fault Zone Segment Boundaries.

Biasi, G.P., Wesnousky, S.G., 2016. Steps and Gaps in Ground Ruptures: Empirical Bounds on

Rupture Propagation. Bulletin of the Seismological Society of America 106. https://doi.org/10.1785/0120150175

Birkeland, P.W., 1984. Soils and Geomorphology. Oxford University Press, New York.

Bormann, J.M., Hammond, W.C., Kreemer, C., Blewitt, G., 2016. Accommodation of missing shear strain in the Central Walker Lane, western North America: Constraints from dense GPS measurements. Earth and Planetary Science Letters 440, 169–177. https://doi.org/10.1016/j.epsl.2016.01.015

Bronk Ramsey, C., 1995. Radiocarbon Calibration and Analysis of Stratigraphy: The OxCal Program. Radiocarbon 37, 425–430. https://doi.org/10.1017/S0033822200030903

Cashman, P., Trexler, J., Muntean, T., Faulds, J., Louie, J., Oppliger, G., 2009. Neogene Tectonic Evolution of the Sierra Nevada – Basin and Range Transition Zone at the Latitude of Carson City, Nevada. Special Paper of the Geological Society of America 447. https://doi.org/10.1130/2009.2447(10)

dePolo, C., 2014. Collaborative Research between the Nevada Bureau of Mines and Geology and the USGS on the Paleoearthquake History of the Kings Canyon Fault Zone, Nevada. USGS NEHRP.

Elliott, A.J., Oskin, M.E., Liu-Zeng, J., Shao, Y., 2015. Rupture termination at restraining bends: The last great earthquake on the Altyn Tagh Fault. Geophysical Research Letters 42, 2164–2170. https://doi.org/10.1002/2015GL063107

Hudnut, K.W., Seeber, L., Pacheco, J., 1989. Cross-fault triggering in the November 1987 Superstition Hills Earthquake Sequence, southern California. Geophysical Research Letters 16, 199–202. https://doi.org/10.1029/GL016i002p00199

Hunter, L.E., Howle, J.F., Rose, R.S., Bawden, G.W., 2011. LiDAR-Assisted Identification of an Active Fault near Truckee, California. Bulletin of the Seismological Society of America 101, 1162–1181. https://doi.org/10.1785/0120090261

King, G.C.P., 1986. Speculations on the geometry of the initiation and termination processes of earthquake rupture and its relation to morphology and geological structure. PAGEOPH 124, 567–585. https://doi.org/10.1007/BF00877216

Li, X., Huang, W., Pierce, I.K.D., Angster, S.J., Wesnousky, S.G., 2017. Characterizing the Quater-

nary expression of active faulting along the Olinghouse, Carson, and Wabuska lineaments of the Walker Lane. Geosphere 13, 2119–2136. https://doi.org/10.1130/GES01483.1

Lienkaemper, J.J., Ramsey, C.B., 2009. OxCal: Versatile Tool for Developing Paleoearthquake Chronologies--A Primer. Seismological Research Letters 80, 431–434. https://doi.org/10.1785/gssrl.80.3.431

McCalpin, J., 2009. Paleoseismology, 2nd ed. Academic Press.

Pierce, I., Wesnousky, S.G., Owen, L.A., Li, X., Caffee, M., 2020. Accommodation of plate motion in an incipient strike-slip system: the Central Walker Lane. Tectonics.

Pierce, I.K.D., Wesnousky, S.G., Owen, L.A., 2017. Terrestrial cosmogenic surface exposure dating of moraines at Lake Tahoe in the Sierra Nevada of California and slip rate estimate for the West Tahoe Fault. Geomorphology 298, 63–71. https://doi.org/10.1016/j.geomorph.2017.09.030

Ramelli, A.R., Bell, J.W., 2009. Spatial and Temporal Patterns of Fault Slip Rates on the Genoa Fault. USGS NEHRP.

Ramelli, Alan R., Bell, J.W., dePolo, C.M., Yount, J.C., 1999. Large-magnitude, late Holocene earthquakes on the Genoa fault, west-central Nevada and eastern California. Bulletin of the Seismological Society of America 89, 1458–1472.

Ramelli, A.R., dePolo, C.M., 1996. Trenching and Related Studies of the Northern Sierra Nevada Range-front Fault System. USGS NEHRP.

Ramelli, A.R., dePolo, C.M., Bell, J.W., 2007. Paleoseismic studies of the Little Valley fault. USGS NEHRP.

Ramelli, A.R., dePolo, C.M., Bell, J.W., 1999. Paleoseismic studies of the Northern Sierra Nevada frontal fault zone (Final Technical Report), U.S. Geological Survey National Earthquake Hazards Reduction Program.

Reitman, N.G., Bennett, S.E.K., Gold, R.D., Briggs, R.W., DuRoss, C.B., 2015. High-Resolution Trench Photomosaics from Image-Based Modeling: Workflow and Error Analysis. Bulletin of the Seismological Society of America 105, 2354–2366. https://doi.org/10.1785/0120150041

Rood, D.H., Burbank, D.W., Finkel, R.C., 2011. Spatiotemporal patterns of fault slip rates across

the Central Sierra Nevada frontal fault zone. Earth and Planetary Science Letters 301, 457–468. https://doi.org/10.1016/j.epsl.2010.11.006

Ross, Z.E., Idini, B., Jia, Z., Stephenson, O.L., Zhong, M., Wang, X., Zhan, Z., Simons, M., Fielding, E.J., Yun, S.-H., Hauksson, E., Moore, A.W., Liu, Z., Jung, J., 2019. Hierarchical interlocked orthogonal faulting in the 2019 Ridgecrest earthquake sequence 7.

Sarmiento, A.C., Wesnousky, S.G., Bormann, J.M., 2011. Paleoseismic Trenches across the Sierra Nevada and Carson Range Fronts in Antelope Valley, California, and Reno, Nevada. Bulletin of the Seismological Society of America 101, 2542–2549. https://doi.org/10.1785/0120100176

Shen, Z.-K., Sun, J., Zhang, P., Wan, Y., Wang, M., Bürgmann, R., Zeng, Y., Gan, W., Liao, H., Wang, Q., 2009. Slip maxima at fault junctions and rupturing of barriers during the 2008 Wenchuan earthquake. Nature Geosci 2, 718–724. https://doi.org/10.1038/ngeo636

Wells, D.L., Coppersmith, K.J., 1994. New empirical relationships among magnitude, rupture length, rupture width, rupture area, and surface displacement. Bulletin of the seismological Society of America 84, 974–1002.

Wesnousky, S.G., 2008. Displacement and Geometrical Characteristics of Earthquake Surface Ruptures: Issues and Implications for Seismic-Hazard Analysis and the Process of Earthquake Rupture. Bulletin of the Seismological Society of America 98, 1609–1632. https://doi.org/10.1785/0120070111

Wesnousky, S.G., 2005. Active faulting in the Walker Lane. Tectonics 24, 35 pp. https://doi.org/10.1029/2004TC001645

Wesnousky, S.G., Bormann, J.M., Kreemer, C., Hammond, W.C., Brune, J.N., 2012. Neotectonics, geodesy, and seismic hazard in the Northern Walker Lane of Western North America: Thirty kilometers of crustal shear and no strike-slip? Earth and Planetary Science Letters 329–330, 133–140. https://doi.org/10.1016/j.epsl.2012.02.018

Wesnousky, S.G., Briggs, R.W., Caffee, M.W., Ryerson, F.J., Finkel, R.C., Owen, L.A., 2016. Terrestrial cosmogenic surface exposure dating of glacial and associated landforms in the Ruby Mountains-East Humboldt Range of central Nevada and along the northeastern flank of the Sierra Nevada. Geomorphology 268, 72–81. https://doi.org/10.1016/j.geo-

morph.2016.04.027

Wesnousky, S.G., Caffee, M., 2011. Range-Bounding Normal Fault of Smith Valley, Nevada: Limits on Age of Last Surface-Rupture Earthquake and Late Pleistocene Rate of Displacement. Bulletin of the Seismological Society of America 101, 1431–1437. https://doi.org/10.1785/0120100238

Wheeler, R.L., 1989. Persistent segment boundaries of Basin-Range normal faults. USGS, pp. 432–444.

Wilkinson, M., Roberts, G.P., McCaffrey, K., Cowie, P.A., Faure Walker, J.P., Papanikolaou, I., Phillips, R.J., Michetti, A.M., Vittori, E., Gregory, L., Wedmore, L., Watson, Z.K., 2014. Slip distributions on active normal faults measured from LiDAR and field mapping of geomorphic offsets: an example from L'Aquila, Italy, and implications for modelling seismic moment release. Geomorphology. https://doi.org/10.1016/j.geomorph.2014.04.026

Zhang, P., Slemmons, D.B., Mao, F., 1991. Geometric pattern, rupture termination and fault segmentation of the Dixie Valley—Pleasant Valley active normal fault system, Nevada, U.S.A. Journal of Structural Geology 13, 165–176. https://doi.org/10.1016/0191-8141(91)90064-P

Chapter II: Accommodation of plate motion in an incipient strike-slip system: the Central Walker Lane

Abstract

Geodetic studies show that ~7–8 mm/yr of right-lateral shear is accumulating across the Central Walker Lane. The rates and patterns of active faults bounding and within the Walker Lake basin and Antelope, Smith, and Mason valleys in the western part of the Central Walker Lane are the focus of this study. Lidar data and geomorphic mapping show geomorphic and geometric characteristics such as northwest oriented linear fault traces, up-hill facing scarps, and larger displacements in right-steps, consistent with the accommodation of northwest directed oblique-slip motion along the Wassuk and Smith Valley rangefront faults, while the Mason and Antelope valley rangefront faults appear to be primarily dip-slip. An active dextral strike-slip fault in the southernmost part of Mason Valley has likely produced earthquakes in the Holocene. Vertical displacement rates based on cosmogenic ages of alluvial fans displaced by range-bounding faults in Antelope, Smith, and Mason valleys are $0.5\ ^{+0.5}/_{-0.3}$, $0.5\ ^{+0.7}/_{-0.4}$, and $0.04\ ^{+0.05}/_{-0.03}$ mm/yr, respectively. The vertical rates correspond to dip-parallel slip rates of $0.6\ ^{+0.7}/_{-0.3}$, $0.7\ ^{+1.0}/_{-0.4}$, and <0.05 mm/yr, for the same three faults, respectively, assuming dips on each fault are 55 ± 10°. The along-strike distribution of scarp heights indicates that the most recent and penultimate earthquakes along the range bounding faults of Smith and Antelope valleys produced ~3 m vertical displacements during ~M_w 7 earthquakes. The pattern of faults forms a 200-km-long left-stepping en-echelon series of dextral, oblique, and normal faults extending from south of Walker Lake to north of Lake Tahoe, similar to observations of laboratory models of dextral shear.

Introduction

Geodetic observations have brought to light a problem in the Central Walker Lane: while 7–8 mm/yr of northwest directed dextral shear is observed with GPS measurements across this part of the Walker Lane (Thatcher et al., 1999; Hammond and Thatcher, 2005, 2007; Hammond et al., 2011; Bormann et al., 2016), over half of this total shear cannot be accounted for by summing the

geologic slip rates of the few known strike-slip faults in this region that is otherwise largely dominated by normal faulting (Wesnousky et al., 2012). I use lidar data to analyze the tectonic geomorphology of Antelope, Mason, and Smith valleys, and a part of the Walker Lake basin to help understand how 7-8 mm/yr of geodetically observed shear is accommodated within the Central Walker Lane between Lake Tahoe and Walker Lake (**Figures 2.1 and 2.2**). Boulder and sediment samples from displaced alluvial surfaces are analyzed for terrestrial cosmogenic nuclide (TCN) and optically stimulated luminescence (OSL) to better constrain the slip rates of range-bounding primarily normal faults. This dissertation summarizes prior work and my new observations bearing on style and rate of faulting for each basin. Here evidence is presented consistent with a model of deformation where left-stepping right-lateral strike-slip faults work in concert with normal faults and transverse left-lateral faults to form a fault system that accommodates significant crustal shear across the Central Walker Lane in the absence of major through-going strike-slip faults.

Field studies and laboratory models show that as strike-slip systems increase in total displacement, the width of the shear zone decreases, while faults become longer, less complex, more continuous, and more efficient at accommodating strain (Wilcox et al., 1973; Aydin and Nur, 1982; Wesnousky, 1988; An and Sammis, 1996; Stirling et al., 1996; Schreurs, 2003; Faulds et al., 2005; Atmaoui et al., 2006; Zinke et al., 2015; Hatem et al., 2017; Zuza et al., 2017). While many of the transform plate boundaries of the world may be considered mature and capable of producing large earthquakes along well organized fault traces that have accommodated hundreds of kilometers of total slip (e.g., the San Andreas, Altyn Tagh, Sagaing, Denali, or Alpine faults), comparably few immature strike-slip systems have been studied in similar detail (e.g., the Walker Lane, Sicily, the Shan Plateau of Myanmar, or the Shanxi Rift of China). These less well-developed systems have, by this definition, accommodated lesser amounts of total slip, and as a result often lack major through-going faults. Instead these systems form broad regions of faulting and deformation along complex systems of numerous short, discontinuous faults, which are often only capable of producing moderate earthquakes. Studying these complex fault systems in nature offers unique insight into the development of fault systems at a plate boundary scale that can otherwise typically only be understood in a laboratory.

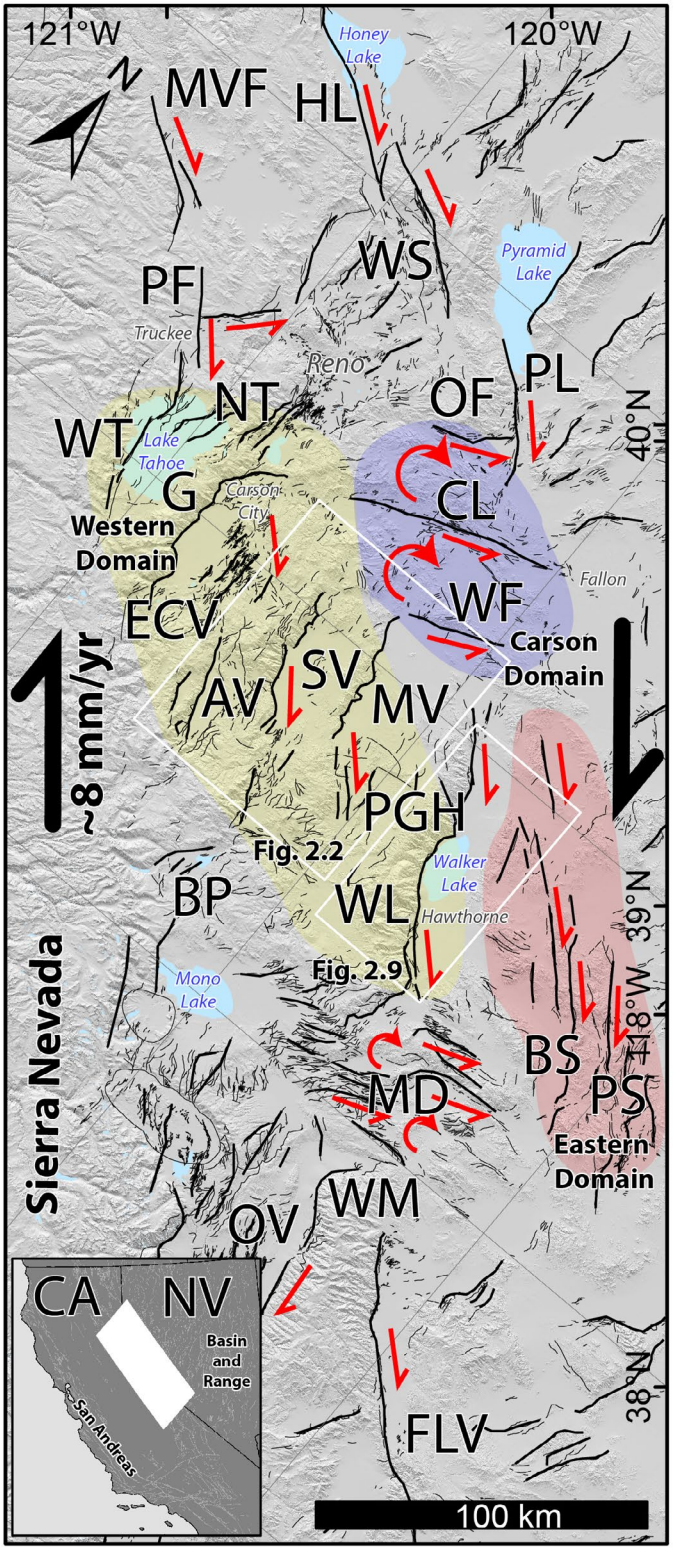

Figure 2.1 Overview map of Walker Lane. Extent of Figures 2.2 and 2.9 are indicated by white boxes. Major faults are thicker while thin faults are from USGS Quaternary fault and fold database. The Central Walker Lane can be divided into the Carson domain (purple), western domain (yellow), and eastern domain (pink). Major faults: MVF- Mohawk Valley, HL-Honey Lake, WS- Warm Springs, PF- Polaris, PL Pyramid Lake, OF-Olinghouse, WT-West Tahoe, NT- North Tahoe (from west to east: Stateline, Incline Village, Little Valley, Washoe Lake), G-Genoa, ECV-East Carson Valley, AV-Antelope Valley, SV-Smith Valley, CL-Carson Lineament, WF-Wabuska, MV-Mason Valley, PGH-Pine Grove Hills, BP-Bridgeport Valley, WL-Walker Lake, BS-Benton Springs, PS-Petrified Springs, MD- Mina Deflection (Rattlesnake, Excelsior, Coaldale), OV-Owens Valley, WM- White Mountains, FLV-Fish Lake Valley.

Regional Context

The Walker Lane (**Figure 2.1**) is an approximately 500-km-long by 100-km-wide northwest trending transtensional intracontinental shear zone composed of discontinuous active faults, basins, and mountain ranges that accommodates up to ~20% of the ~50 mm/yr of dextral shear between the Pacific and North American plates (Bennett et al., 2003; Dixon et al., 2000; Thatcher et al., 1999; Unruh et al., 2003). The Walker Lane sits between the Sierra Nevada Mountains to the west and the north-northeast trending normal faults and ranges of the Basin and Range to the east, roughly following the California-Nevada border. The disorganization of faults in the Walker Lane has been cited as evidence of the youthful expression of an incipient transform boundary (e.g., Faulds et al., 2005; Faulds and Henry, 2008). The Walker Lane is well defined geodetically by a zone of ~9 mm/yr of northwest directed right-lateral shear in the southern part, decreasing to ~7 mm/yr in the Northern Walker Lane (e.g., Hammond et al., 2011; Wesnousky et al., 2012; Bormann et al., 2016), while the San Andreas fault system accommodates ~40 mm/yr of dextral shear, west of the Sierra Nevada (Unruh et al., 2003). Throughout the Walker Lane, dextral shear is expressed as transtension, accommodated as strike-slip along well defined faults (e.g., Benton Springs; Wesnousky 2005), as series of left-lateral, transverse "bookshelf faults" (e.g., Cashman and Fontaine, 2000), partitioned into normal faults at range fronts with separate strike-slip faults along the interiors of basins (e.g., Owens Valley; Beanland and Clark, 1994), and has been hypothesized within portions of the Central Walker Lane to be taken up by rotations of crustal blocks bounded by major range-bounding normal faults (e.g., Wesnousky et al., 2012).

The Walker Lane is divided into several regions that display distinctly different fault systems (**Figure 2.1**). The Northern Walker Lane is composed of the predominantly northwest-striking dextral strike-slip Pyramid Lake (Briggs, 2004; Angster et al., 2016), Warm Springs (Gold et al., 2013), Honey Lake (Gold et al., 2017), Polaris (Hunter et al., 2011), and Mohawk Valley (Gold et al., 2014) faults. The Southern Walker Lane is composed of predominately northwest striking strike-slip and normal faults, including the Owens Valley (Beanland and Clark, 1994; Lee et al., 2001; Kirby et al., 2008; Haddon et al., 2016), Fish Lake Valley (Frankel et al., 2007; Ganev et al., 2010; Frankel et al., 2011), and White Mountains (Stockli et al., 2003; Kirby et al., 2006) faults. The Central Walker Lane interrupts this northwest structural grain with a series of north-striking range-bounding faults with

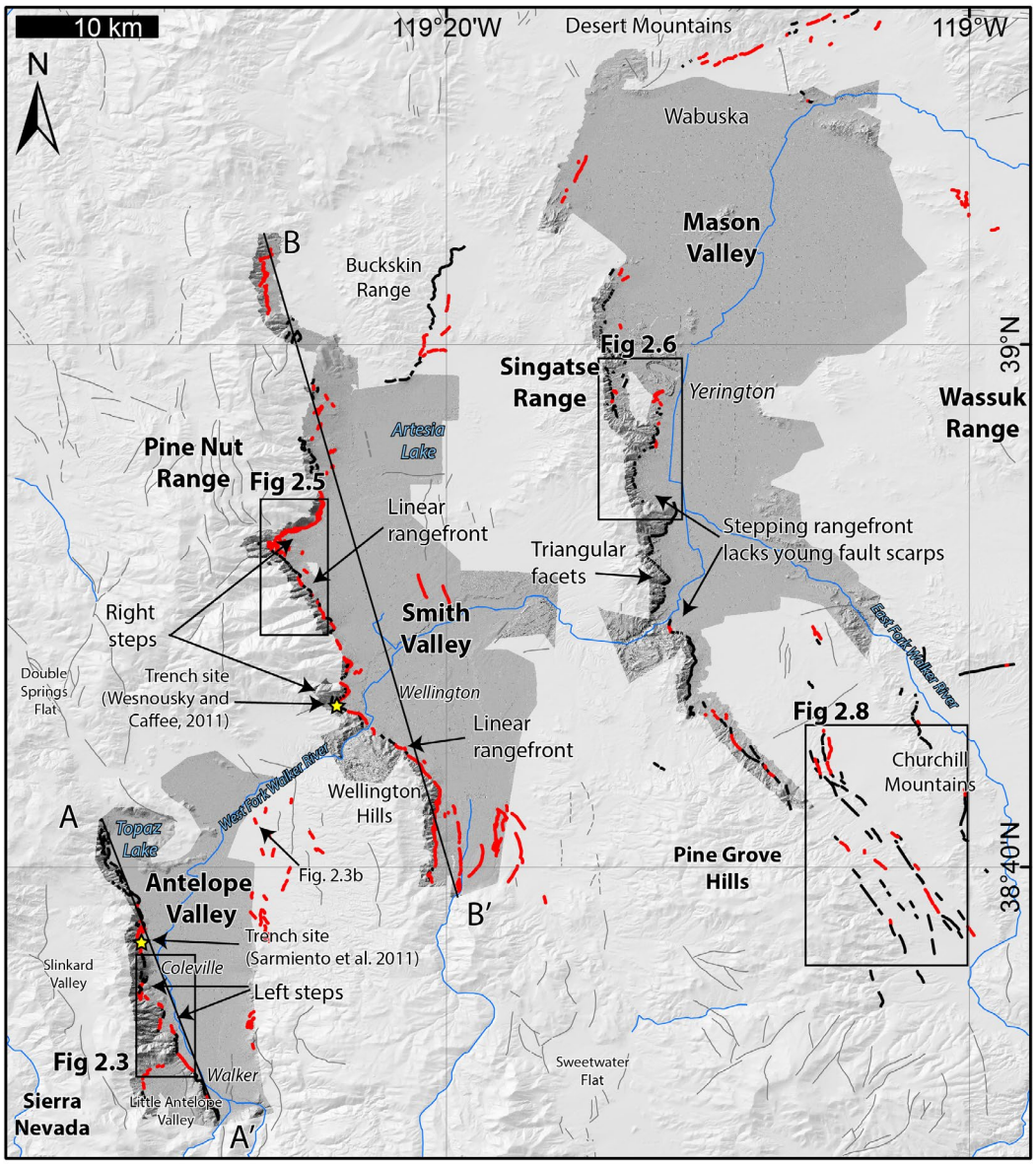

Figure 2.2 Overview of study area. Dark grey hillshades indicate extent of lidar data. Red lines are faults mapped in this study and observed cutting alluvial deposits, and dark black faults are bedrock-alluvial active fault contacts. Light black lines are faults from USGS Quaternary fault and fold database. Black boxes indicate the extent of Figures 2.3, 2.5, 2.6, and 2.8. Profiles A-A' and B-B' are plotted in Figure 2.10.

large normal components, transverse left-lateral faults, and some northwest-striking dextral faults.

The Central Walker Lane can be further subdivided into three domains (**Figure 2.1**). The eastern domain or Walker Lake block is composed of the northwest striking dextral strike-slip Benton Springs, Indian Head, Gumdrop, and Petrified Springs faults (Wesnousky, 2005; Angster et al., 2019). The northerly Carson domain (e.g. Cashman and Fontaine, 2000; Wesnousky, 2005; Li et

al., 2017) is composed of the transverse, northeast-striking, sinistral Wabuska, Olinghouse (Briggs, 2005), and Carson faults and lineaments. The western domain is composed of the basins and their range-bounding faults that are the focus of this dissertation, including the Tahoe (Kent et al., 2005; Maloney et al., 2013; Pierce et al., 2017) and Walker Lake (Bormann et al., 2012; Dong et al., 2014; Surpless and Kroeger, 2015) basins, and Carson (Ramelli et al., 1999; dePolo and Sawyer, 2005), Smith (Wesnousky and Caffee, 2011), Mason, and Antelope (Sarmiento et al., 2011) valleys.

The western domain of the Central Walker Lane is defined by a series of subparallel north-striking/east-dipping active range-bounding faults each dividing a mountain range to the west from a half-graben holding a basin to the east. These north-strike of the ranges contrast sharply with the northeast-striking ranges of the Basin and Range to the east of this region, and the continuous high topography of the Sierra Nevada to the west. Most of these range-bounding faults are ~30–45 km long (except for the ~85 km long Wassuk rangefront fault) and form a rough left stepping en-echelon pattern, with faults spaced ~20–35 km apart from east to west. The westward stratigraphic tilt of these ranges decreases to the northwest from 60° in the Wassuk and Singatse ranges, to <20° in the Carson Range, and <5° in the Sierra Nevada, and likewise the southeasterly Singatse and Wassuk ranges have considerably higher amounts of total extension (>150%) than the ranges to the west (Surpless et al., 2002), which has been cited as evidence of the progressive westward encroachment of faulting into the Sierra Nevada. Thermochronologic data show that many of the mountain ranges in the region have undergone two phases of exhumation: an initial period ~14–15 Ma, and a younger period sometime between 3 and 10 Ma (Surpless et al., 2002). This second phase was initially attributed by Surpless et al. (2002) to be a result of Basin and Range extension, yet this timing coincides with the imitation of the Walker Lane at these latitudes (e.g., Faulds and Henry, 2004), so may be a result of the encroachment of Walker Lane deformation, while the earlier phase may be attributed to Basin and Range extensional faulting (Surpless et al., 2002).

The problem of missing slip in the Central Walker Lane

Both cumulative lateral displacements and the geodetically measured shear rates across the Walker Lane decrease from south to north. Guest et al. (2007) state that as much as ~110 km of right-lateral slip has been accommodated across the Stateline, Owens Valley, Panamint Valley,

and Death Valley-Fish Lake Valley faults of the Southern Walker Lane since the mid-Miocene. In the Northern Walker Lane, Faulds et al. (2005) show that only ~20–30 km of net dextral shear has been accommodated by strike-slip faults. Cashman and Fontaine (2000) and Carlson (2017) present paleomagnetic evidence of >50° of clockwise vertical axis rotations that have accumulated in some of the Miocene volcanic rocks of the Carson domain. Across the Central Walker Lane, GPS profiles measure ~7–8 mm/yr of northwest directed dextral shear (Hammond et al., 2011; Wesnousky et al., 2012; Bormann et al., 2016). This magnitude of shear and rotation appears to have been largely accommodated in the absence of major through going northwest-directed dextral strike-slip faults in the western domain of the Central Walker Lane, and as Wesnousky et al. (2012) show, profiles can be drawn perpendicular to the trend of the Walker Lane without crossing any major faults in the Central Walker Lane.

Optimally-oriented, closely-spaced right-lateral strike-slip faults of the Walker Lake block of the Central Walker Lane accommodate ~4 mm/yr of dextral shear (Angster et al., 2019). Aside from a short fault segment observed along the eastern margin of the Wassuk Range (Dong et al., 2014), there are no previously reported right-lateral strike-slip faults in the western or Carson domains that accommodate the remaining >3 mm/yr of dextral shear. GPS transects show that the observed shear is evenly spaced across the Central Walker Lane, and is not isolated to the Walker Lake block (Bormann et al., 2016).

Wesnousky et al. (2012) suggested that range scale block rotations and asymmetric, northward-opening basins accommodate the observed geodetic shear across the western domain of the Central Walker Lane. Geodetic block models (e.g. Bormann et al., 2016) suggest that as much as ~1.5 mm/yr of dextral oblique slip is accommodated by each of these range-bounding normal faults, in addition to clockwise vertical axis rotations of crustal blocks. However, the paleomagnetic work of Carlson (2017) suggests that while significant block rotations have occurred in the Carson domain, there has been little rotation of the ranges in the western domain. Thus, strike-slip faulting in the western domain may play a larger role in accommodating Walker Lane shear than has been previously recognized. Such strike-slip faulting may be either (1) diffused across scattered, discontinuous faults (similar to the 1932 M_s 7.2 Cedar Mountain earthquake, e.g., Bell et al., 1999), (2) accommodated by off-fault deformation that is not preserved or readily observed by available

paleoseismic methods (e.g., Gold et al., 2015; Personius et al., 2017), or (3) accommodated along previously unrecognized major strike-slip faults (e.g., Dong et al., 2014), all of which are hypotheses addressed in this dissertation.

Resources and Methods

Quaternary mapping and high resolution topographic data sources

Descriptions of faulting characteristics along each of the faults and lineaments are derived from the analysis of large-scale (~1:12,000) low-sun-angle black and white aerial photographs, Google Earth satellite imagery, structure-from-motion models, and lidar data (three existing datasets from the USGS, Desert Research Institute, and National Wildlife Service are merged with the ~334 sq km of new data that was acquired for this project through the National Center for Airborne Laser Mapping). Lidar datasets are merged into a seamless dataset for each basin and then contour, and hill- and slope-shade maps are generated for geomorphic analysis. Structure-from-motion elevation models are generated using Agisoft Photoscan Pro with images collected using a DJI Phantom 3+ quadcopter. Images are georeferenced from sites located in a target region using a Trimble R10 dGPS unit, resulting in ~25 cm/pixel resolution models.

Generalized surficial maps based on interpretations of lidar data and satellite imagery at a scale of 1:12,000 are constructed for Mason, Smith, and Antelope valleys using a modification of the methods outlined in Bull (1991) as used in various other studies in this region (e.g., Bell et al., 2004; Wesnousky, 2005; Koehler and Wesnousky, 2011; Sarmiento et al., 2011; Wesnousky and Caffee, 2011; Li et al., 2017). In the figures in this dissertation, deposits are divided into units based on relative age and type of geomorphic landform/sediment: fluvial (Qfl), basin fill (Qbf), playa/lacustrine (Qp), aeolian (Qd), and four alluvial fan units (Qa, Qy, Qi, and Qo). Land obscured by anthropogenic activity (anth) and undivided bedrock (bx) are also mapped. Alluvial fan units are divided by relative age primarily using height above modern stream grade, amount of dissection, height of fault scarp (if present), and textural differences in imagery and lidar data. Fault traces in this dissertation are divided as either fault scarps that are clearly expressed in Quaternary deposits (red lines) or as inferred faults and/or fault contacts between Quaternary deposits and bedrock (black lines).

Surfaces of the oldest alluvial fan units (Qo) are composed of weathered boulders with soils

that have well-developed Bt and carbonate horizons. These form the highest and oldest alluvial fan units that are often incised >10 m with well-rounded interfluves. These Qo alluvial fans are considered to be early to middle Pleistocene. Intermediate alluvial fans (Qi) are moderately incised with well-developed drainage networks and are modified by shoreline deposits when near the high stand of Lake Lahontan. Qi alluvial fans are considered middle to late Pleistocene in age. Qy alluvial fans are low lying, and have smooth surfaces in lidar, and a dark tone in imagery. Qy alluvial fans are Holocene and latest Pleistocene. Qa alluvial fans represent active washes and alluvial fans, and are differentiated from Qy alluvial fans by lighter tone on imagery and well-defined channel morphology. Where faults are present, Qy alluvial fans are sometimes differentiated from Qa alluvial fans by fault scarps that do not cut the younger Qa alluvial fans.

Geochronology

Surficial ages are estimated using measurements of in-situ terrestrial cosmogenic nuclide (TCN) ^{10}Be and ^{36}Cl concentrations of surface boulders, TCN ^{10}Be concentrations of soil depth profiles, and optically stimulated luminescence (OSL) of buried sand lenses. Both ^{10}Be and ^{36}Cl concentrations are measured at the PRIME lab at Purdue. All ^{10}Be samples are processed in the Geochronology Laboratories at the University of Cincinnati following the methods of Kohl and Nishiizumi (1992). The OSL analyses are also performed at the University of Cincinnati. The ^{36}Cl samples are processed and analyzed at the PRIME lab. Detailed descriptions of sample preparation and analysis are in the Appendix.

Boulder sampling focuses on the largest boulders from alluvial fan surfaces. Approximately 500 g samples are taken from the upper 2–5 cm of each of these boulders. Photographs of each of the sampled boulders are provided in the Appendix. ^{10}Be concentrations and laboratory data are listed in the Appendix. The ^{10}Be TCN boulder exposure ages are calculated using the Cosmic Ray Exposure Program (CREp) of Martin et al. (2017) and are listed in **Table 2.1**. The ages reflect the increased concentrations of ^{10}Be that occur in rock as a function of the time they are exposed to cosmic rays at Earth's surface. The calculator requires input describing the geographic coordinates and elevation of the samples, local shielding of the sample, density of the sample, and estimation of the boulder erosion rates resulting from processes such as boulder grussification and spalling (Gosse

and Phillips, 2001). These values are listed for each sample in the Appendix. The calculations are made using no erosion rate. The age estimates are also dependent on the assumption of particular scaling models designed to estimate the long-term production rate of cosmogenic ^{10}Be. The ^{10}Be ages in **Table 2.1** use a production rate of 44.0 ± 0.3 at/g SiO_2/yr determined at Twin Lakes, which is located at a higher elevation than the fan surfaces here, but is within 100 km of all study sites (Balco et al., 2008; Borchers et al., 2016; Nishiizumi et al., 1989), the ERA40 atmosphere model of Uppala et al. (2005), the Lifton-VDM2016 geomagnetic database (Lifton, 2016), and the time-dependent scaling model of Lal (1991) and Stone (2000). The ^{36}Cl boulder ages are calculated using the CRONUS calculator for ^{36}Cl, and are listed in **Table 2.1**, with laboratory details in the Appendix.

To determine the age of a surface using a cosmogenic depth profile, a ~2-m-deep profile is excavated and the exposed sediment is sampled at varying depths for ^{10}Be analysis. The resulting ^{10}Be concentrations as a function of depth are modeled using the Hidy et al. (2010) MATLAB code, which uses a Monte-Carlo simulation to find the best fit of the data and resulting surface age. Soil textural grain size analysis is performed by A&L Great Lakes Laboratories, Inc.

OSL samples are extracted using 20-cm-long plastic tubes from sand lenses exposed in a hand excavated pit. All tubes are packed and wrapped double-bagged in opaque media for transport. OSL samples are processed and analyzed at the luminescence dating laboratories at the University of Cincinnati in subdued sodium lighting (588 nm). Quartz grains are isolated from heavy minerals and feldspars using pretreatment with H_2O_2, HCl and HF, and magnetic separation. Modified single-aliquot regeneration (SAR) protocols (Wintle and Murray, 2006) were employed on small aliquots (200–500 grains; 100–150 μm in diameter) to estimate equivalent doses using a Risø OSL DASH measurement system. U, Th, Rb, and K are measured at Activation Laboratories Limited Ancaster, Ontario Canada to determine sediment dose rates and estimations of the contribution of cosmic dose rate accounted for geographic position, elevation, and depth, burial depth, and water content as outlined in the Appendix.

Scarp height measurements

Fault scarp vertical heights are determined by extracting topographic profiles from lidar data. Topographic profiles are extracted approximately orthogonal to fault scarps where both hang-

ing and footwall surfaces are similar and show minimal to no modification by geomorphic and anthropogenic processes unrelated to faulting (e.g., road cuts, younger fan deposition, fluvial modification, etc.). Profiles are analyzed using a python code written for this study (see Appendix) that fits linear regressions to points selected by the user that are representative of the hanging wall, foot wall, and fault scarp surfaces. The vertical separation between the footwall and hanging wall regressions is then measured at the horizontal midpoint of the intersections between the fault scarp and each of the hanging and foot walls (e.g. Rood et al., 2011).

Slip Rate Calculations

Vertical slip rates are determined by dividing the probability distributions of the displacement of a surface by the age of the displaced surface using the MATLAB code of Zechar and Frankel (2009). The probability distribution of the age of a surface is the sum of the uncertainties of all of the samples from a single surface. This approach is taken to reduce the uncertainty of scattered sample ages resulting from inheritance or erosion. With this method all samples are treated equally. The uncertainty of the displacement is assumed to be Gaussian, described by the mean and standard deviation of the scarp heights of a number of profiles extracted perpendicular to a fault scarp in a deposit of a single age. A Gaussian distribution is used to better estimate the actual average fault offset from a number of measurements of fault scarps, modified unknown amounts by erosion on the hanging wall, deposition on the footwall, and the natural variability of the earthquake displacement along fault strike. The approach is thus aimed at determining an "average" slip rate, rather than a maximum or minimum bound, along a particular fault section where numerous measurements of age and displacement are recorded.

Study Areas

Antelope Valley

Antelope Valley is a west tilted half-graben with a northwest striking, east-dipping active rangefront fault along its western margin separating the basin from the mountains to the west (**Figure 2.2**). The West Fork of the Walker River flows from south to northeast through the basin, generally following the western side, and likely obscuring any long-term evidence of faulting along its

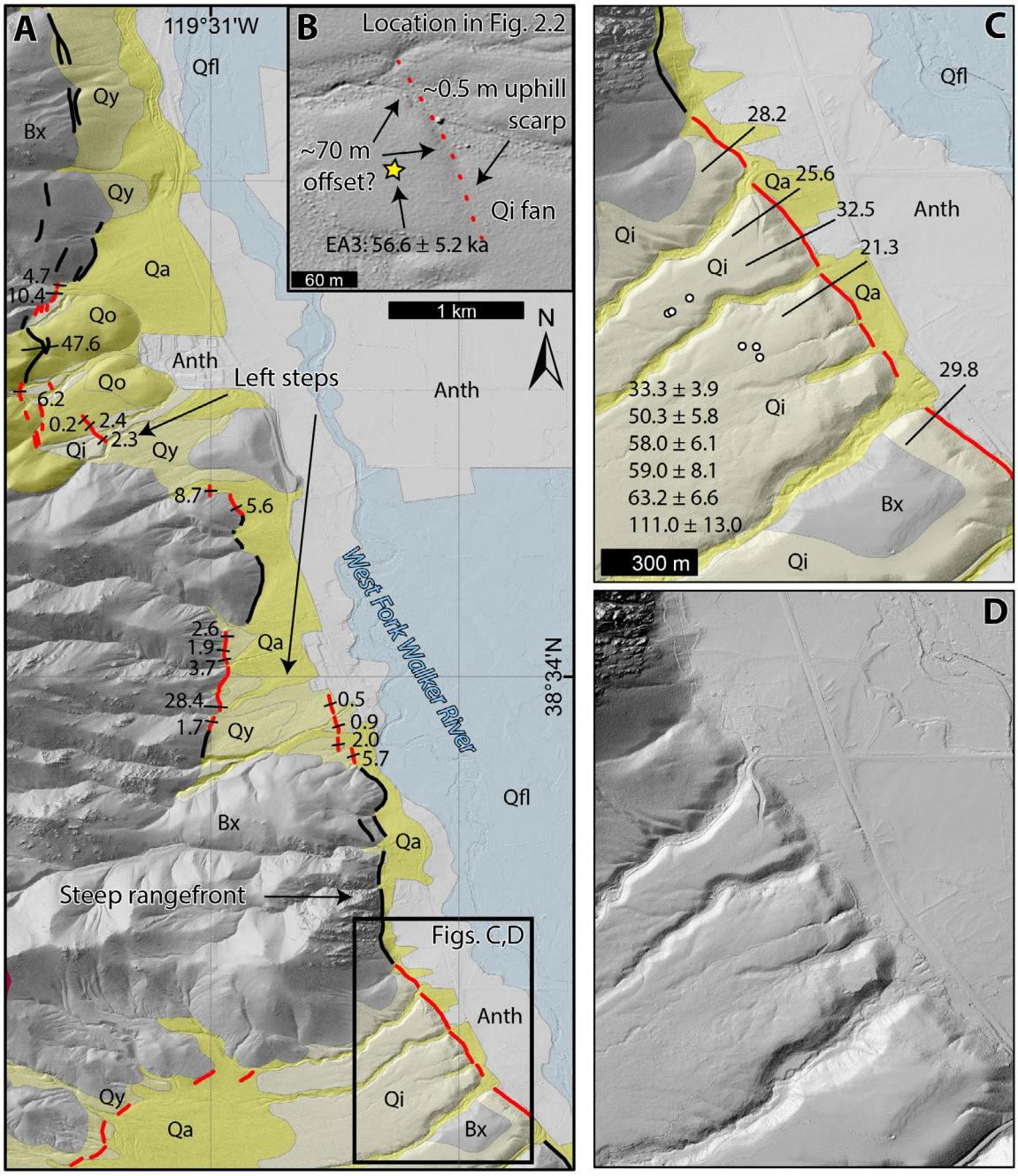

Figure 2.3 Section of Antelope Valley rangefront showing left-stepping pattern (A) and location of Walker slip rate site (c). (b) is a section of eastern Antelope Valley (location in Fig. 2.2) where a Qi alluvial fan is apparently offset ~70 m. Location of OSL samples EA1-3 with minimum age of 56.6 ± 5.2 ka are indicated. Black faults are bedrock-alluvial fault contacts. Red faults are fault scarps in alluvial deposits. Straight black lines are scarp profiles and values are scarp heights in (m). Walker slip rate site interpreted (c) and bare lidar hillshade (d). Scarp profiles (black lines), heights (in m), and ages (ka) of boulder samples (white dots) are shown in (c).

path within the valley. The rangefront exhibits frequent, prominent triangular facets, and forms ~800 m of relief above the valley floor. While the overall trend of the fault follows a ~23-km-long northwest trace, fault scarps are only expressed in intermediate and young alluvial deposits for ~15 km of that length, and generally form a left-stepping pattern of discontinuous mostly north-trending fault scarps **(Figure 2.3)**. Fault scarps in late Quaternary alluvial deposits that range in height from ~1–3 m to >20 m commonly occur at the mouths of drainages (**Figure 2.3**), demonstrating the repetition of late Quaternary earthquakes. Topaz Lake obscures any evidence of the rangefront fault along the northwestern portion of Antelope Valley. North of Topaz Lake, and outside of my lidar

Method	Sample name	Location		Elevation above sea level (m)	Age (ka)	1σ error (ka)
		latitude (°N)	longitude (°W)			
Mason Valley	*Upper Yerington Fan*					
^{10}Be Boulder	MVS1	38.9669	119.2012	1424	451.1	37.2
^{10}Be Boulder	MVS2	38.9661	119.2019	1430	93.3	6.6
^{10}Be Boulder	MVS3	38.9660	119.2034	857	183.5	13.5
^{10}Be Boulder	MVS4	38.9653	119.2028	1431	90.5	6.9
^{10}Be Depth Profile	M1-Pit	38.9669	119.2012	1425	173.1	$^{38.7}/_{-32.5}$
Smith Valley	*Artesia Fan - intermediate surface*					
^{10}Be Boulder	SF1	38.8908	119.4158	1494	30.2	2.6
^{10}Be Boulder	SF2	38.8909	119.4163	1497	19.3	1.6
^{10}Be Boulder	SF3	38.8903	119.4158	1491	40.4	2.8
	Artesia Fan - intermediate surface (Wesnousky and Caffee, 2011)					
^{10}Be Boulder	CWL-2	38.8907	119.4150	1480	32.5	3.0
^{10}Be Boulder	CWL-3	38.8907	119.4148	1470	40.7	3.7
^{10}Be Boulder	CWL-4	38.8907	119.4148	1480	69.9	6.3
	Artesia Fan – upper younger surface					
^{10}Be Boulder	SF4	38.8892	119.4164	1494	21.3	2.0
^{10}Be Boulder	SF5	38.8892	119.4165	1494	12.1	1.7
^{10}Be Boulder	SF6	38.8893	119.4171	1500	34.7	2.9
	Artesia Fan - lower younger surface					
^{10}Be Boulder	SF8	38.8892	119.4149	1468	27.4	2.6
^{10}Be Boulder	SF9	38.8892	119.4148	1472	26.6	3.0
^{10}Be Boulder	SF10	38.8894	119.4145	1458	13.4	2.1
^{10}Be Boulder	SF11	38.8888	119.4142	1450	10.3	1.3
Antelope Valley	*Walker Fan*					
^{36}Cl Boulder	CWL-5	38.54039	119.5023	1654	58.0	6.1
^{36}Cl Boulder	CWL-6	38.54071	119.5025	1650	111.0	13.0
^{36}Cl Boulder	CWL-7	38.54069	119.5024	1649	59.0	8.1
^{36}Cl Boulder	CWL-8	38.54164	119.5049	1657	63.2	6.6
^{36}Cl Boulder	CWL-9	38.54169	119.5048	1659	50.3	5.8

Table 2.1 Geochronology. Details are in Appendix

data, there are discontinuous scarps approaching Double-Springs Flat (**Figure 2.2**).

Walker Slip Rate Site

A large uplifted alluvial fan terrace is present just northwest of the town of Walker (**Figure 2.3**). Five profiles measured across different parts of the fault scarp at this site (**Figure 2.3c**) have vertical separations ranging from 21.3 to 32.5 m, with a mean value of 27.5 ± 4.3 m. The surface here forms a ~1-m-thick alluvial cap exhibiting numerous boulders on a bedrock pediment surface that is incised over 20 m by drainages (**Figure 2.3c).** The faulted surface exhibits a bench of slightly lower elevation adjacent to the fault. The surface of this bench contains a thin scattered rounded

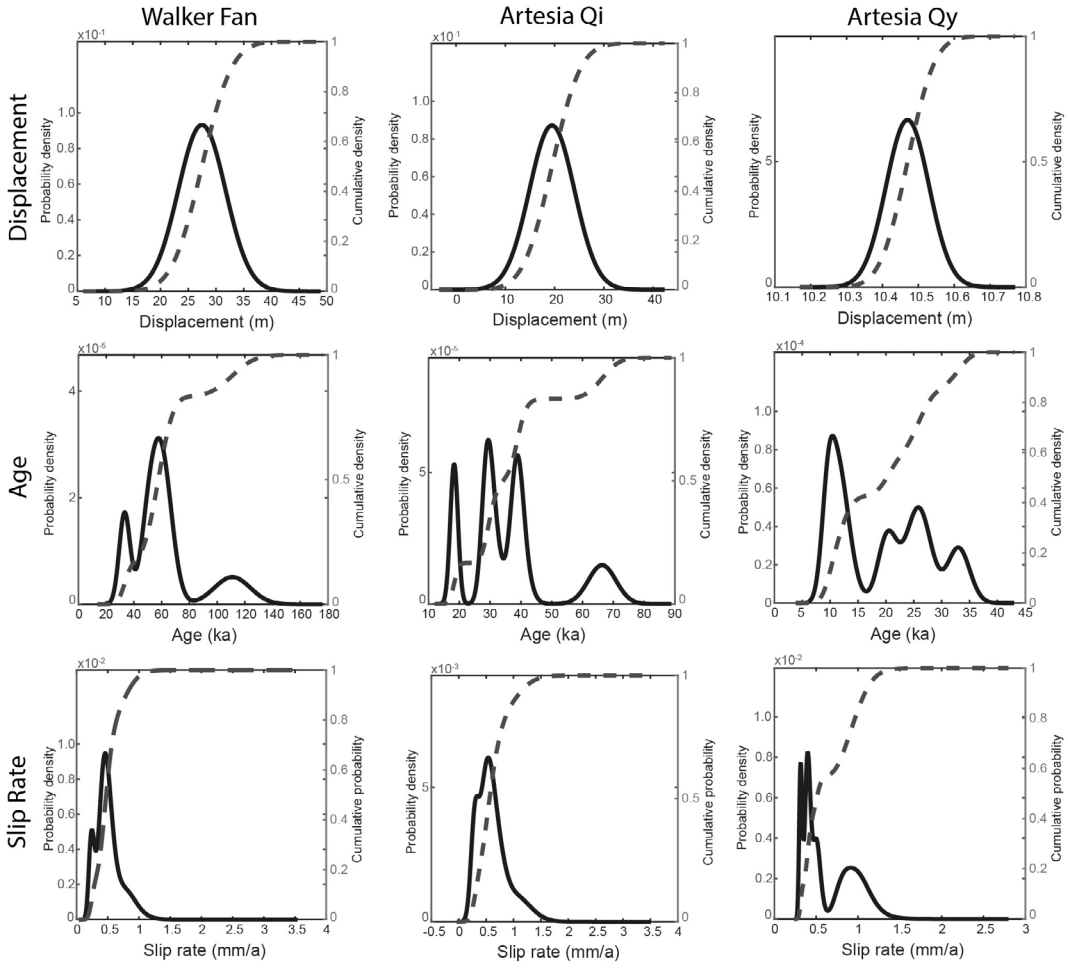

Figure 2.4 Displacement, age, and vertical slip rate probability distributions for the Antelope Valley and Smith Valley range bounding faults. For each plot, probability densities are the solid lines (left axis), while cumulative probabilities are the dashed lines (right axis).

cobble deposit that was likely deposited by the Walker River. Not only does the scarp itself appear to be modified by the Walker River, but the lower surface here is buried by younger fan activity and fluvial deposition from the nearby Walker River, and thus this measured displacement is a minimum. Boulders on the Qi surface here are heavily weathered, mostly volcanic rocks sourced from the nearby Sierra Nevada. Here, I collected six boulder samples for ^{36}Cl cosmogenic analysis (**Table 2.1**). Resulting ages range from 33.3 to 111.0 ka (**Figure 2.3c**). Combining the average vertical separation with this age distribution results in a vertical separation rate of $0.5\ ^{+0.5}/_{-0.3}$ mm/yr (**Figure 2.4**). The section of rangefront immediately adjacent and north of this site is composed of a several hundred meter tall granite bedrock escarpment with slopes ranging from 50 to >70° (**Figure 2.3a**), which may reflect a steep dip of the range front fault.

Faulting in east Antelope Valley

The east side of the basin contains a series of uplifted, faulted, and tilted alluvial surfaces that appear to grade into pediment surfaces extending westward from the crest of the Wellington Hills (**Figure 2.2**). The surfaces are mostly outside of the extent of the available lidar data. Google Earth imagery shows a series of discontinuous both north and northwest trending fault scarps. Many of the fault scarps are uphill (east) facing with some exhibiting right-lateral deflections of drainages, which may be a result of strike-slip faulting. The alluvial surfaces in the eastern part of the valley are incised by numerous small drainages and appear to be intermediate and old. The scarps within the surfaces are generally small and likely do not rupture frequently.

At one location in eastern Antelope Valley a channel incised into a broad Qi alluvial fan is obliquely cut by a short ~300-m-long fault trace of relatively weak geomorphic expression (**Figure 2.3b**). The fault forms a slight (~0.5 m) uphill-facing fault scarp in the Qi fan and appears to laterally displace this channel ~70 m. Three samples were extracted from sand lenses exposed in a pit dug into the Qi surface and were dated using OSL. Samples EA1 and EA2 were saturated, with a likely age of >51 ka, and EA3 resulted in an age of 56.6 ± 5.2 ka. Combining this minimum age of 56.6 ± 5.2 ka with this displacement of ~70 m results in a maximum right-lateral slip rate of 1.2 ± 0.4 mm/yr. The estimated slip rate seems anomalously high in relation to the short length of the fault strand, the relatively weak geomorphic expression of the scarp, and the lack of offsets in the younger depos-

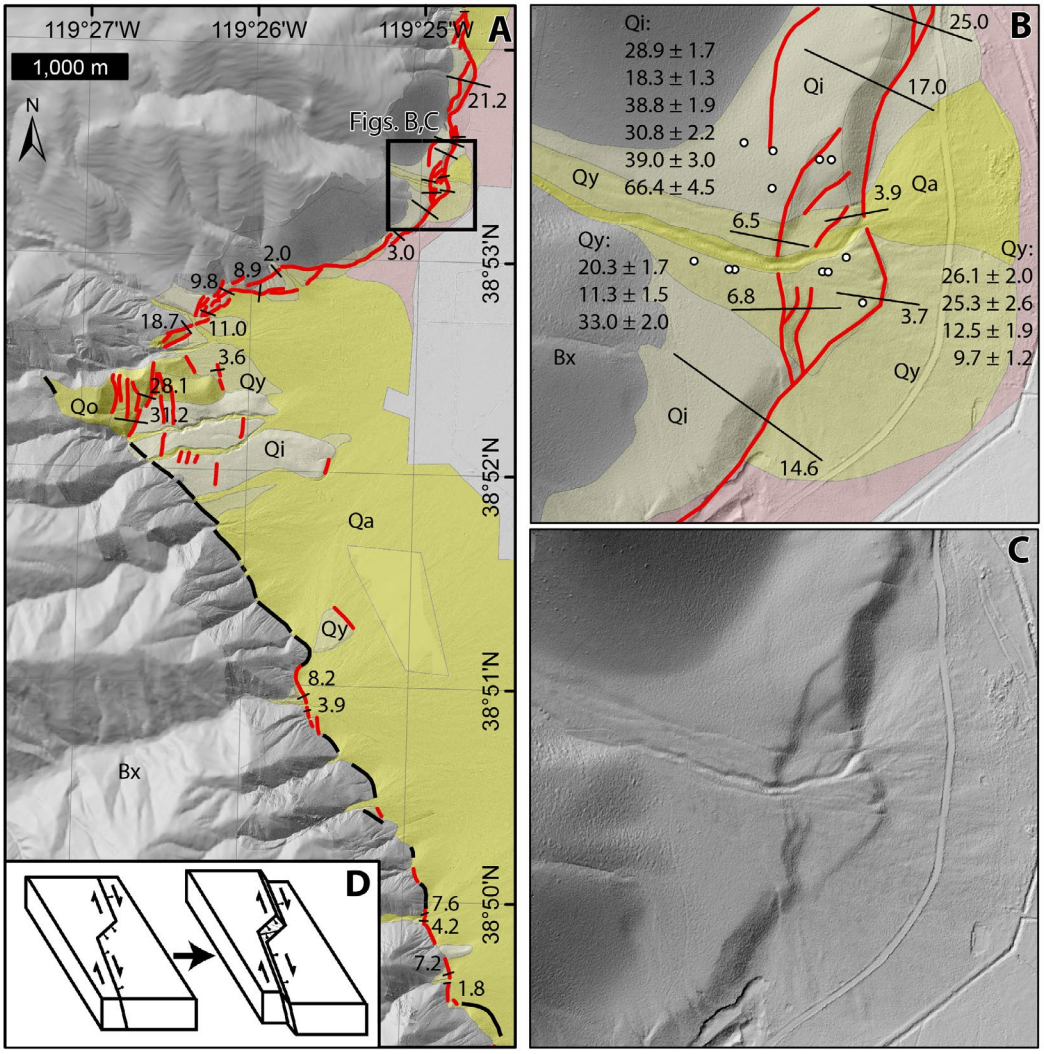

Figure 2.5 Section of Smith Valley rangefront showing geometry of large right step (a) and location of Artesia fan slip rate site (b, c). Black faults are bedrock-alluvial fault contacts, while red faults are fault scarps in alluvial deposits. Values in (a) are scarp heights (in m). Artesia fan rate site interpreted (b) and bare lidar hillshade (c). Scarp profiles, heights (in m), and ages (ka) of boulder samples (white dots) are shown in (b). (d) Simplified block diagram of a right-bend in a right-lateral oblique fault system provided to explain relatively larger vertical displacements in the step.

its farther along strike closer to the Walker River. Nonetheless, I present the observation to illustrate the only possible direct evidence I observed for strike-slip motion along the east side of the valley. If this >57 ka age is assumed for the rest of the Qi alluvial fan surfaces in eastern Antelope Valley, then the lack of geomorphic expression of significant faulting suggests that the few discontinuous fault scarps here are not accommodating a significant amount of the regional strain.

Smith Valley

Smith Valley is a half-graben with a NNW-striking active rangefront fault bounding the Pine Nut Range to the west **(Figure 2.2)**. The half graben is ~50-km-long, and 15-km-across at its widest. The total vertical relief from the valley floor to the crest of the Pine Nut Range is over 1400 m. The West Fork of the Walker River enters Smith Valley through a narrow canyon near the town of Wellington (**Figure 2.2**). It bends northeastward here and meanders across the basin through a canyon of increasing depth before it exits the valley on the eastern side, cutting through the Singatse Range. This canyon is cut into lacustrine and fluvial deposits, likely deposited by Pluvial Lake Wellington, which reached a highstand of 1477 m above sea level (asl) between 60 and 80 ka (Stauffer, 2003; Wesnousky and Caffee, 2011). In the central part of the basin, just north of the Walker River, there are a pair of left-stepping, north striking, en-echelon fault strands that form 1–2-m-high scarps in stabilized aeolian/dune deposits (**Figure 2.2**). The faults do not cut any of the younger floodplain deposits closer to Walker River. Artesia Lake, a small playa remnant of pluvial Lake Wellington (Stauffer, 2003), is present in the northern part of Smith Valley, and is hydrologically isolated from the Walker River.

The range bounding fault in Smith Valley forms an abrupt rangefront with triangular facets, scarps in young alluvial fans, and uplifted alluvial terraces. The rangefront fault generally strikes northwest and makes several northeast-striking right steps separating otherwise long, northwest striking linear sections (**Figure 2.2**). When the strike of the fault changes from north-northwest to northeast within these right-steps, both the frequency of scarps and their heights increase dramatically from less frequent ~6–8-m-high scarps in the linear NNW sections to >20-m-scarps along the largest of these northeast striking step overs near the Artesia Fan **(Figure 2.5)**. The fault primarily exhibits down to the east/southeast vertical displacement, and nowhere did I observe laterally displaced stream channels recording right-lateral strike-slip motion. The faulting in the southernmost portion of the basin near the Wellington Hills forms a horsetail splay (**Figure 2.2**) of numerous large (~5–10-m-high) scarps. These scarps are generally sub-parallel to the northward drainage of the basin in this area and thus may be modified by fluvial processes. The northern portion of Smith Valley is occupied by the Buckskin Range, which is bounded by an active fault on its east flanks. This fault forms a fairly continuous north-northeast striking scarp in young, intermediate, and older alluvial

fan deposits. To the west of the Buckskin Range, there is a continuation of the Smith Valley range-front fault, and here I observe frequent grabens, en-echelon fault scarps, and vertically displaced Holocene Qy alluvial deposits.

Artesia Fan slip rate site

At the eastern edge of a ~1.4-km-long right-step over in the north-northwest striking range-front fault **(Figure 2.5)**, older fan surfaces exhibit progressively larger vertical scarps than younger surfaces. Three alluvial fan surfaces are mapped in **Figure 2.5b:** Qa are the active alluvial fan deposits, forming a narrow active channel cut into young Qy deposits, and on the basin floor form a small fan overtopping Qy deposits. These Qy deposits form an alluvial fan on the hanging wall of the fault as well as on the margins of the main Qa channel on the footwall, and are composed of light gray, rounded, unweathered granitic boulders in a poorly-sorted matrix. Intermediate Qi deposits are only found on the footwall of the fault and are redder in color, with a smoother, less bouldery surface than Qy. The fault has an anastomosing pattern in **Figure 2.5b** that, from south to north, starts as a single strand, splits into two, then three strands, before coalescing into a single strand again. A maximum age of the Qi fan here is constraint by a 60–80 ka tephra exposed in a road cut in the fault scarp (Stauffer, 2003; Wesnousky and Caffee, 2011). I collected 10 boulder samples for ^{10}Be analysis on the Qi and Qy displaced alluvial fan units and combined these with 3 recalculated ^{10}Be boulder ages at this site from Wesnousky and Caffee (2011) (**Figure 2.5b**). Six boulder samples were collected from the footwall of the intermediate unit (Qi, **Figure 2.5b**), and range in age from 18 to 66 ka (mean age of 37.0 ± 16.3 ka), and seven samples from both the hanging and footwalls of a younger aged alluvial fan unit (Qy, **Figure 2.5b**) range in age from 10 to 33 ka (mean age of 19.7 ± 8.9 ka) (**Table 2.1**). While these ages are scattered, the mean ages of the young surface are roughly half of that from the intermediate surface. The average of four profiles measured from the available lidar data (**Figure 2.5**) show that scarp height in the single strand that cuts the intermediate unit is 19.5 ± 4.5 m, while two profiles of each of the two scarps in the younger unit measure 3.8 ± 0.1 and 6.6 ± 0.2 m, respectively, or 10.5 ± 0.1 m combined (**Figure 2.5**). Dividing these scarp heights by the ages of the boulder samples from each surface leads to a vertical separation rate of $0.6\ ^{+0.8}/_{-0.2}$ mm/yr for the intermediate surface and $0.5\ ^{+0.7}/_{-0.2}$ mm/yr for the young surface **(Figure 2.4)**. The two rates

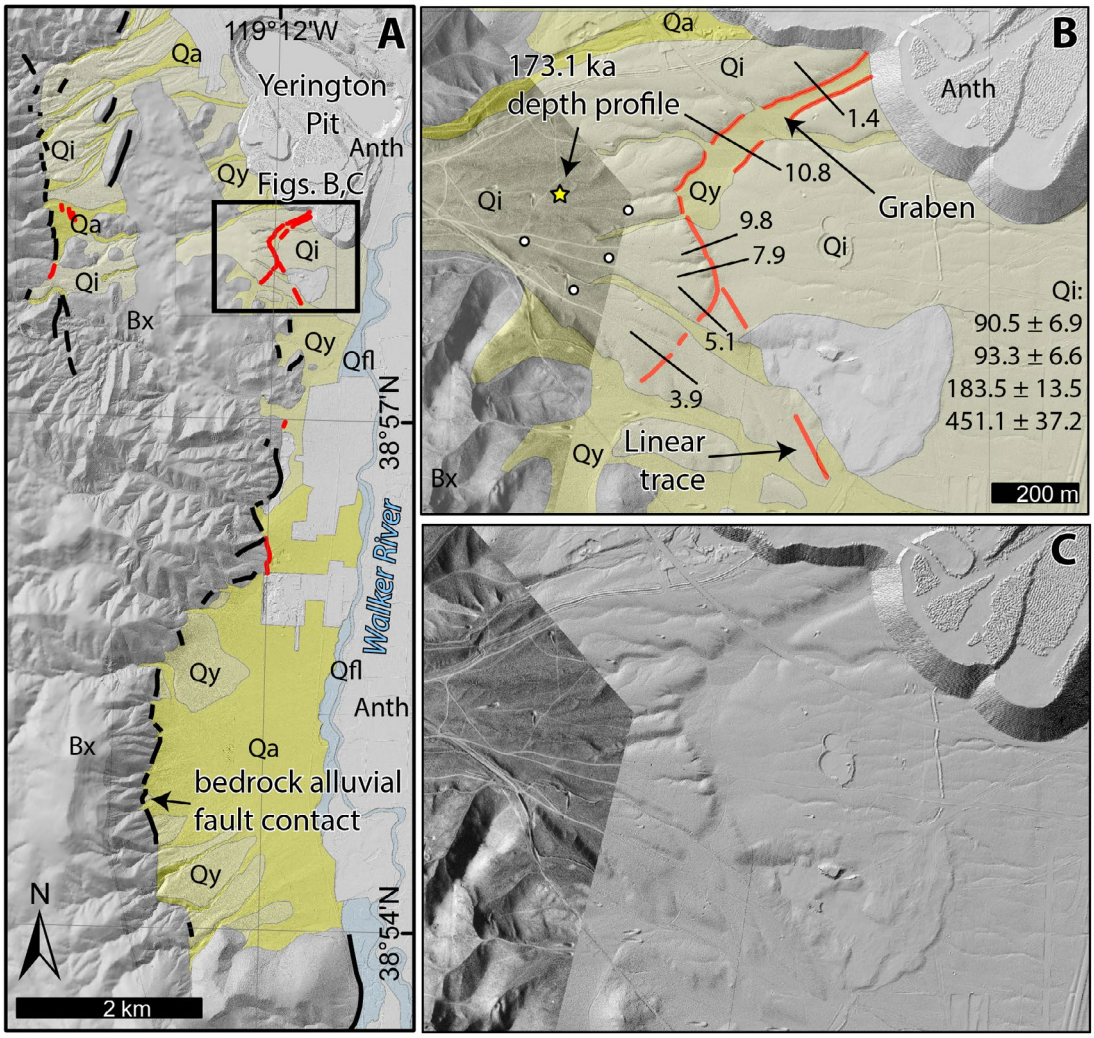

Figure 2.6 Section of Mason Valley rangefront (a) showing lack of fault scarps preserved in alluvium (red) and location of Yerington fan slip rate site (b). Yerington fan rate site interpreted (b) and bare lidar hillshade / low sun angle aerial photo composite (c). Scarp profiles, heights (in m), and ages (ka) of boulder samples (white dots) are shown in (b), while the age and location of the depth profile (Figure 2.7) is indicated by the star.

over different timescales generally agree.

Both the linearity and strike of the long northwest striking segments of the rangefront in Smith Valley suggest that a component of strike-slip is accommodated along the rangefront fault. The Artesia fan is located on the edge of the largest right-step in the Smith Valley rangefront, where scarps are both more frequent and larger than elsewhere along the rangefront (**Figure 2.5**), and the strike in this step is nearly perpendicular to the primary northwest strike of the rangefront. In a right-lateral fault system, right-steps produce extension parallel to the trace of the right-lateral fault

(**Figure 2.5d**). The vertical displacement at the Artesia Fan is attributed to the kinematics of a right-step in a northwest striking fault with a large component of right-lateral strike-slip. For an obliquely slipping rangefront like Smith Valley, a low rate of lateral-slip may lead to the burial/obfuscation of possible geomorphic indicators of discrete lateral earthquake offsets.

Mason Valley

Mason Valley is a 55-km-long by 20-km-wide half-graben bounded by active faults separating the basin from the Singatse Range to the west and the Pine Grove Hills to the southwest **(Figure 2.2)**. The Desert Mountains bound the northern margin of Mason Valley where the northeast-striking left-lateral Wabuska fault is located (Li et al., 2017). The Singatse Range is considerably smaller in topographic expression than the other ranges in this region, forming only ~700 m of relief above the valley floor. The northern portion of the basin was occupied by pluvial Lake Lahontan during its high stand ~14.5 ka (Adams and Wesnousky, 1998; Reheis, 1999), and prominent wave-cut shoreline benches and beach deposits are preserved on Qy deposits that are below the ~1332 m elevation of the high stand. Evidence for any pre-Holocene faulting in much of the northern portion of the basin may be obscured by lacustrine processes associated with Lake Lahontan and evidence of more recent faulting in the central portion of the basin may be obscured by agricultural activity.

The region to the east/southeast of Mason Valley, and east of the Churchill Mountains in **Figure 2.2**, forms a series of complicated small basins and mountain ranges composed of incised Qi aged and older fan/pediment surfaces, short discontinuous faults, and disrupted bedrock (Gilbert and Reynolds, 1973). These basins are both oriented north-south and east-west. The faults in this part of the basin strike both north-northwest and east-northeast, and are generally only traceable for a maximum of ~5 km.

The fault at the base of the Singatse Range forms a sinuous trace with frequent left and right steps and bends from ~5 km south of where the west fork of the Walker River enters the basin for ~35 km northward (**Figure 2.2**). The Singatse range front is composed of prominent triangular facets, suggestive of active normal faulting, however the fault along the Singatse Range is almost always only expressed as a bedrock alluvium contact, except for the site described in the following section, and forms a sharp contrast with other major range bounding faults in the area that often exhibit

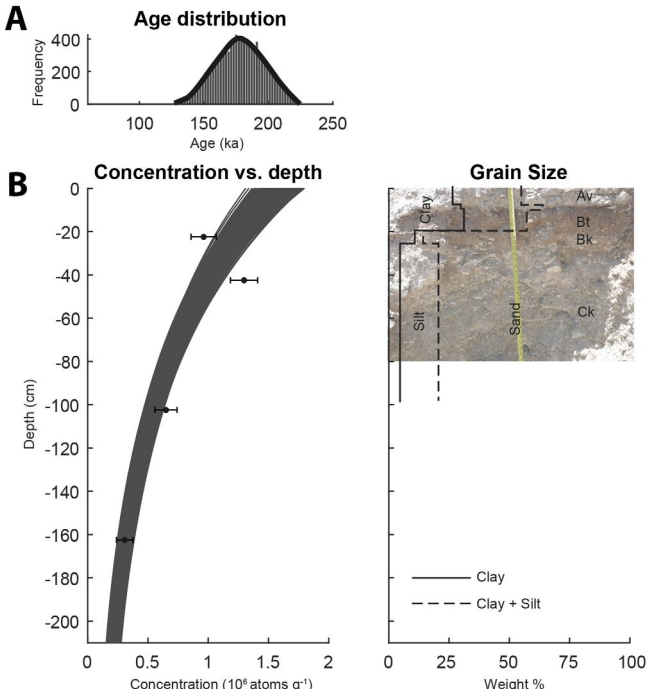

Figure 2.7 Results for the Mason Valley depth profile sampled at the Yerington fan, modeled using the Hidy et al. (2010) MATLAB code. The resulting age is 173.1 $^{+38.7}/_{-32.5}$ ka. (a) distribution of modeled results for the age of the depth profile. (b) Monte Carlo solutions (left) of concentration of 10Be vs. depth and soil textural analysis with well-developed Bt horizon (right) overlain on a photograph of the upper portion of the depth profile.

scarps in young alluvial deposits. In several places along the rangefront small antithetic grabens are observed, yet there is a dearth of uplifted fan surfaces.

The character of rangefront faulting in Mason Valley abruptly changes ~5 km south of where the west fork of the Walker River enters the southwestern margin of the basin (**Figure 2.2**) The southern part of the basin is bound by the Pine Grove Hills, and instead of forming a rangefront composed of sharp triangular facets, the rangefront is subdued and is composed of a series of uplifted old alluvial fans and pediments. Here, satellite imagery and lidar data show a discontinuous series of linear, northwest-striking faults and lineaments that extend for ~22 km until the southernmost extent of the basin. Generally these faults have a northeast down sense of motion, and locally right-laterally displace fan deposits and channels.

Yerington Fan slip rate site

Adjacent to the Yerington Pit (**Figure 2.6**) a northwest striking fault scarp merges with a

northeast striking fault scarp to form a large northeast striking graben cutting intermediate age alluvial fan deposits (**Figure 2.6**). The alluvial fan is incised up to ~6 m by channels and forms broad smooth interfluve surfaces with infrequent highly weathered granitic and volcanic boulders. Depending on where fault profiles are measured (**Figure 2.6**), vertical separation varies from as little as 1.4 m across the graben at the northeastern extent of the fault scarp to as much as 10.8 m, with an average of 6.5 ± 3.6 m for the 6 profiles. Here, I collected a depth profile of 4 samples as well as 4 surficial boulder samples for cosmogenic ^{10}Be analysis to constrain the age of the faulted surface. Boulder ages sampled from the Qo surface here range from 90.5 ± 6.9 ka to 451.1 ± 37.2 ka with a mean of 204.6 ± 169.9 ka, and modeling the depth profile results in an age of 173.1 $^{+38.7}/_{-32.5}$ ka (**Figure 2.7**). The well-developed soil, with a thick Bt horizon, (**Figure 2.7b**) is consistent with the modeled age of the depth profile. Combining the 173.1 $^{+38.7}/_{-32.5}$ ka age of the depth profile with the 6.5 ± 3.6 m average displacement of the surface results in a vertical slip rate of <0.04 mm/yr. The

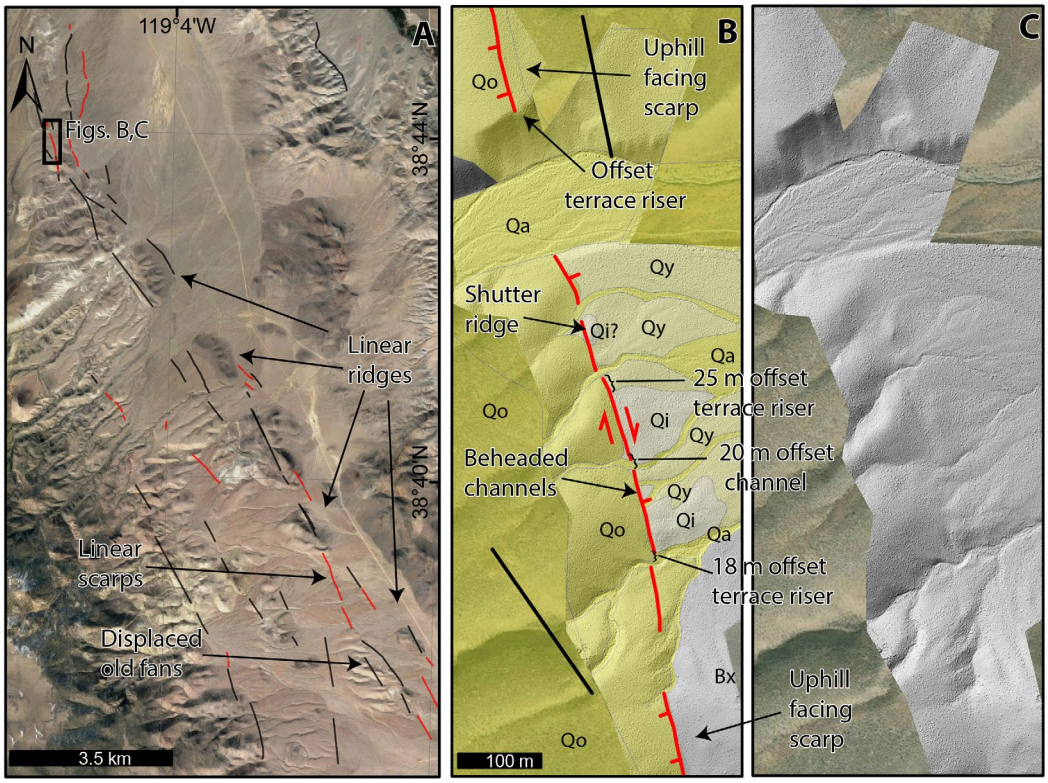

Figure 2.8 Satellite image of the Pine Grove Hills fault zone in southern Mason Valley (a). Location indicated in Figure 2.2. Red lines indicate faults in alluvial deposits, while black are fault traces in bedrock. (b) shows an interpreted SfM model (c) of a section of this fault zone that demonstrates right-lateral displacements.

geometry of the linear northwest striking fault segment associated with a large northeast striking graben is consistent with northwest-directed dextral motion, however the measured slip rate is very low and thus this fault does not likely accommodate a significant amount of the regional strain.

Pine Grove Hills fault zone

Figure 2.8a is a Google Earth satellite image of a portion of the southern part of Mason Valley (**Figure 2.2**). Here, several subparallel fault traces are well expressed as a series of linear bedrock ridges and scarps in different ages of alluvial fans. The linear bedrock ridges are primarily composed of Mio-Pliocene sedimentary and volcanic rocks, including the Morgan Valley and Coal Valley formations (Gilbert and Reynolds, 1973). **Figure 2.8b** is a Quaternary map based on a hill-shade of a 0.25 m/pixel resolution structure-from-motion model of a part of one of these northwest striking fault-lineaments, where a linear fault trace right-laterally displaces Qy and Qi deposits. Two Qi terrace risers are displaced ~25 and ~18 m right-laterally, and a channel is dextrally offset ~20 m by this fault. Additionally along the strike of this fault are two beheaded channels, two right-laterally deflected channels, and a small shutter ridge (**Figure 2.8b).** Additionally, the direction of the scarp produced by the fault changes from west facing, to east facing, to west facing again along strike, demonstrating the strike-slip nature of this fault. The morphology of the Pine Grove Hills fault is similar to other active strike-slip faults in the region with slip rates ranging from ~0.5 to 1.5 mm/yr (e.g., Wesnousky, 2005; Angster et al., 2019). No age estimates of the offset surfaces are available to determine a slip rate for the Pine Grove Hills fault.

Walker Lake Basin

The Walker Lake basin (**Figure 2.9**) is the largest basin of those examined and is ~100-km-long by 20-km-wide. The western margin of the basin is bound by the Wassuk range, which hosts a prominent active east-dipping normal fault, forming more than 2200 m of vertical relief. The vertical slip rate (>0.3–0.4 mm/yr) and paleoseismic history of this fault zone are described by Bormann et al. (2012). Dong et al. (2014) describe an active strike-slip fault in the northern part of the basin that displaces Lahontan aged shoreline deposits at a right-lateral slip rate of ~1 mm/yr (**Figure 2.9b**). Here observations are focused on additional evidence of strike-slip faulting and fault

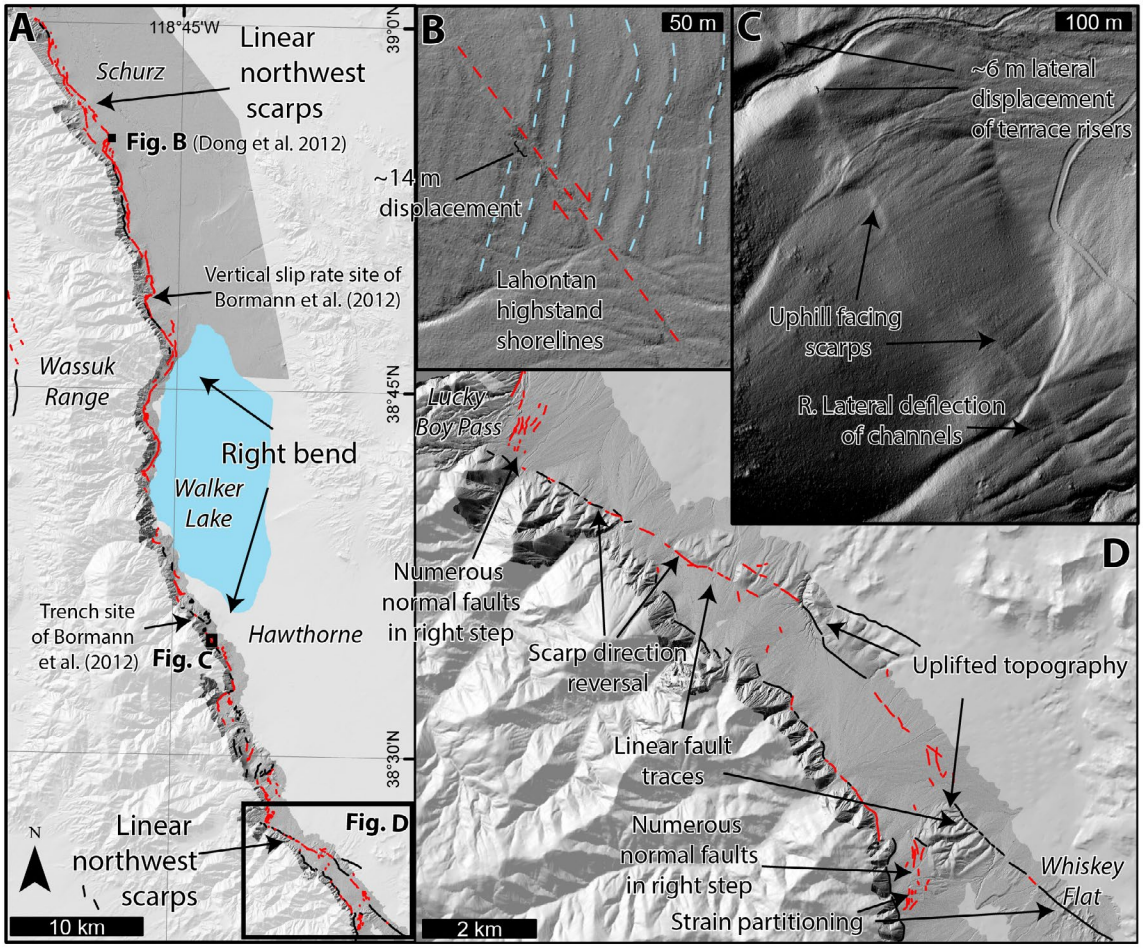

Figure 2.9 Fault map (a) of the Wassuk fault zone. Lidar hillshades are darker gray, light gray background is a hillshaded 10 m DEM. Red lines are fault scarps in alluvial deposits, black are inferred and/or bedrock-alluvial fault contacts. The fault geometry forms two northwest striking segments separated by a large right step coincident with Walker Lake and the deepest part of the basin. The northwest striking segments contain alternating scarp directions, linear scarps, and right-lateral displacements, all consistent with strike-slip faulting. Right-stepping segments locally exhibit greater degrees of normal faulting. Locations of (b-d) are indicated on (a). (b) Blowup of site from Dong et al. (2014) showing 14 m right-lateral displacement of ~14.5 ka Lahontan shorelines with slip rate of ~1 mm/yr. (c) Segment of fault near Hawthorne where an uphill facing linear scarp deflects a number of channels and offsets a pair of terrace risers ~6 m. (d) shows the southern portion of the Wassuk fault zone. Here strain is partitioned into a linear basin-ward strike-slip fault and a normal fault against the range.

geometry (**Figure 2.9**).

The geometry of the Wassuk rangefront in **Figure 2.9a** provides a basis to divide the fault into 3 segments. From north to south, a linear northwest striking segment extending northwest from near Schurz, a central sinuous roughly north and northeast striking segment along the western shore of Walker Lake, and a southern northwest striking linear segment from Hawthorne to

Whiskey Flat (**Figure 2.9d**). This central section forms a right-step in the fault system. The deepest portion of the basin, Walker Lake, is located in the right-step. This geometry of the Walker Lake fault system has been previously described as a rhomboidal pull-apart in a strike-slip system (Mann, 2007), with Walker Lake itself situated in the depocenter of this pull-apart (Link et al., 1985). This geometry is similar to the step-over observed in Smith Valley, but on a larger scale (**Figures 2.2 and 2.4**).

Directly west of Hawthorne (**Figure 2.9c**) is a northwest-trending, linear, uphill-facing fault scarp that right laterally displaces two terrace risers as well as a series of gullies. From this area south to Lucky Boy Pass (**Figure 2.9d**), the fault forms a right-stepping pattern of north and northeast trending normal fault scarps and northwest trending linear scarps.

North of Lucky Boy pass are a series of north-striking grabens and prominent vertical fault

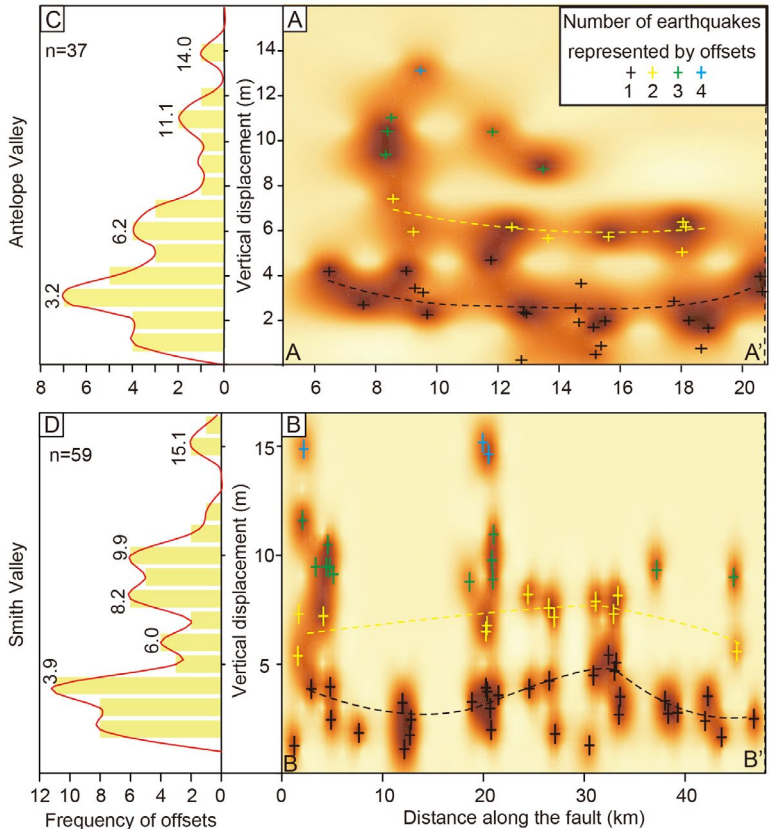

Figure 2.10 Slip distribution plots (a, b) and displacement histograms (c, d) for Antelope Valley (a, c) and Smith Valley (b, d). Locations of cross sections indicated on Figure 2.2. The displacement of the most recent and penultimate earthquakes for each fault can be estimated by looking at the smallest two peaks of each histogram. For the slip distributions (a, b), darker colors indicate higher probabilities. The colored crosses represent our interpretation of the number of earthquakes which produced each displacement measurement.

scarps (**Figure 2.9d**). From Lucky Boy pass to the southeast is a linear northwest striking fault segment that extends for ~10 km. The first ~3 km of this fault segment forms a north facing fault scarp along the rangefront. The strike-slip fault trace then continues to the southeast linearly away from the rangefront forming subdued uphill-facing fault scarps. The remainder of this fault segment forms two fault traces that form south and north facing scarps and a prominent pop-up, pressure ridge-like feature of uplifted bedrock, fan, and pediment surfaces. South from here the fault bends to the southeast more and forms subdued scarps in a large distal fan, before again forming a second popup feature, similar in scale to the first. The rangefront southward from here is more northerly striking and forms a number of east facing scarps at canyon mouth drainages. The faulting mapped along a portion of the rangefront in **Figure 2.9d** is an example of strain partitioning: where a basin-ward strike-slip fault is separated from a rangefront normal fault.

The ~30-km-long series of fault segments extending from the southern margin of Walker Lake to Whiskey Flat (**Figure 2.9d**) is generally northwest striking. Normal displacements observed in north-striking bends are systematically larger than observed along the northwest-striking linear segments. The linearity of the fault traces, the alternating-facing fault scarps, and the several beheaded channels and lateral displacements in the northwest-striking portions of the fault zone, and the magnitude of scarps in the north-striking right-steps are all consistent with northwest directed dextral faulting.

Discussion

Displacement distributions, recurrence intervals, expected magnitudes of earthquakes, and "short" faults in the Central Walker Lane

Scarp heights are measured along the lengths of the Smith and Antelope valley rangefront faults to produce displacement distribution plots (**Figures 2.2 and 2.10**). These scarp heights are fitted to a linear approximation of each rangefront fault. The distance along this line of each of these measurements is plotted against the height of each measurement to demonstrate the distribution of scarp heights along the strike of the fault. Additionally, histograms with 1.0 m vertical displacement bins are presented to analyze the displacement distribution for clusters that might be attributable to individual paleoseismic events (**Figure 2.10**). Combining these displacement distribution plots

(**Figure 2.10)** with the length of the faults and the slip rates (**Figure 2.4)** for the range-bounding faults in Smith and Antelope valleys allows for an estimation of the magnitude of paleoearthquakes as well as anticipated average return times for earthquakes.

The smallest two peaks of each of the histograms of vertical displacements for Antelope and Smith valleys (**Figure 2.10**) are interpreted as the vertical displacements resulting from the most recent event (MRE) and penultimate earthquakes. These displacements are 3.9 and 2.1 m for Smith Valley and 3.2 and 3 m for Antelope Valley. Displacements observed in prior paleoseismic trench studies on the two faults are similar: 3.5 m for the MRE in Smith Valley (Wesnousky and Caffee, 2011) and 3.6 and 2 m (Sarmiento et al., 2011) for the MRE and penultimate earthquakes in Antelope Valley.

For Smith Valley, dividing the 3.9 and 2.1 m MRE and penultimate events by the ~0.6 mm/yr vertical separation rate determined for the fault in this study results in estimated earthquake return times ranging from 3500 to 6500 years. The result is in general accord with the report of the single earthquake ~3000 years ago reported by the paleoseismic trench study of Wesnousky and Caffee (2011) for the fault. For Antelope Valley, dividing the 3.2 and 3 m displacements by the 0.5 mm/yr vertical separation rate results in earthquake return times ranging from 6000 to 6400 years. Sarmiento et al.'s (2011) trenching study in Antelope Valley showed an inter-event time between the most recent and penultimate earthquakes equal to ~5000 years, which is also similar to the ~6000 year estimate based on the slip rate and displacement distribution.

The definition of moment magnitude is (modified after Hanks and Kanamori, 1979):

$$M_w = 2/3 \ \log(\mu A d) - 10.7$$

where, here I assume that the fault area (A) is equivalent to the fault width (15 km estimated here) multiplied by the measured map view length of each fault (50- and 22-km for Smith and Antelope valleys, respectively), the average displacement (d) is measured for the MRE from the displacement distributions, and the shear modulus (μ) is 3×10^{11} dynes/cm^2. These inputs result in an expected M_w 7.3 for Smith Valley and M_w 7.0 for Antelope Valley for the most recent events on each fault, respectively. Surficial displacements are less than fault displacement at depth, and fault rupture lengths are poorly constraint by mapped fault scarps, so these are likely underestimates of magnitude.

Using the relation of fault length to moment magnitude from Wesnousky (2008) results in expected magnitudes of 6.9 and 6.7 for the 50- and 22-km-long faults in Smith and Antelope valleys, respectively. These estimates are approximately a quarter magnitude less than estimated using the moment magnitude equation above. Likewise, for the mapped fault lengths, the expected displacements for these faults should be on average 1.5 and 0.7 m, with maxima of 4.5 and 2.0 m, respectively (Wesnousky, 2008). These average values are roughly half and a quarter of what is observed along the Smith and Antelope valley rangefront faults, respectively. Average displacements of ~3 m, similar to values observed on each of these faults, are typically associated with a normal fault surface rupture length of ~100 km (Wesnousky, 2008). Two hypotheses can explain the observation that observed fault lengths appear insufficient to produce the observed offsets: (1) faults in this part of the Walker Lane rupture with other nearby faults producing longer total rupture lengths, or (2)

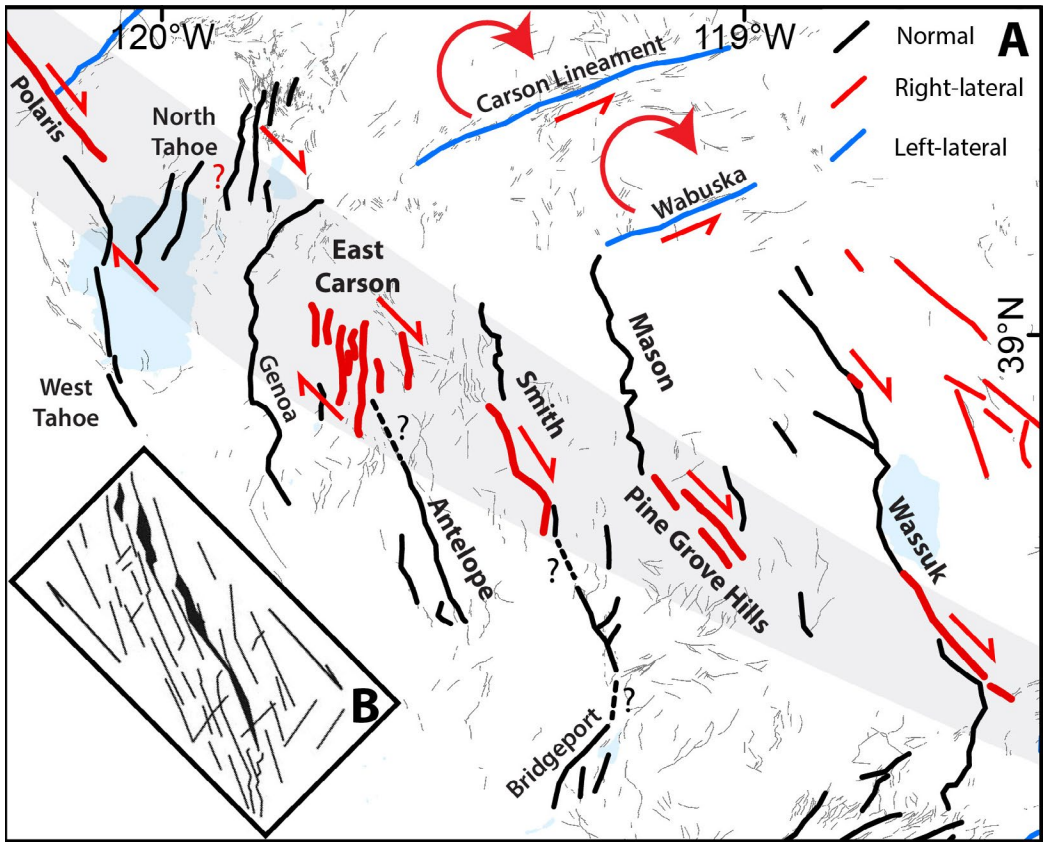

Figure 2.11 (a) Fault pattern of the Central Walker Lane. The grey band demonstrates a well-defined zone of en-echelon left-stepping dextral strike-slip faulting. Queried dashed lines indicate possible connections between faults as discussed in text. (b) Sketch of a clay model copied from Atmaoui et al. (2006) produces a similar pattern of left stepping en echelon faults and basins as is observed in the Central Walker Lane.

these faults rupture independently and produce high-stress drop earthquakes.

The size of the observed single event displacements on a number of other faults in this region (e.g., the Incline Village, Little Valley, Stateline, Pine Grove Hills, Bridgeport Valley, and the unnamed faults of eastern Mason Valley) are also greater than expected from historical observations relating fault rupture length to displacement (Wesnousky, 2008; Seitz and Kent, 2014). The traces of several of these faults are less than 20 km yet some have been demonstrated to have produced single event displacements of ~3 m. Faults in the Central Walker Lane may produce complicated, multi-segment ruptures with multiple shorter fault strands (including previously unrecognized fault strands) supporting larger (M_w 7+) earthquakes, not dissimilar to the 1891 M_w 7.5 Nobi, Japan (Kaneda and Okada, 2008), 1932 M_s 7.2 Cedar Mountain, Nevada (Bell et al., 1999), 1970 M_s 7.2 Gediz, Turkey (Ambraseys and Tchalenko, 1972), or 2016 M_w 7.8 Kaikoura, New Zealand (Hamling et al., 2017) earthquakes. In Smith Valley, for example, the rangefront fault may produce ruptures extending further south along strike towards Strawberry Flat, or even as far as Bridgeport Valley, where numerous large normal fault scarps are preserved in these two small (~15-km-long) basins (**Figure 2.11a**). This would result in a total rupture length of ~75-100 km, as one might expect based on the measured displacements and the relations in Wesnousky (2008). Antelope Valley might rupture along with faults to the north in the East Carson Valley fault zone, increasing rupture length from ~20 to ~65 km (**Figure 2.11a**).

It is also possible that the earthquake ruptures in this region are indeed limited to these short mapped fault traces, as normal faults have historically produced large displacements with

	Vertical	Dip Parallel (55± 10° normal fault)	Extension		GPS	GPS Strike-Slip[a]
Artesia Qy	0.5 +0.7/-0.2	0.6 + 0.9/-0.2	0.4 +0.5/-0.1	0.4?	0.4 ± 0.5	0.5 ± 0.4
Artesia Qi	0.6 +0.8/-0.4	0.7 + 1.0/-0.5	0.4 +0.6/-0.3	0.4?	0.4 ± 0.5	0.5 ± 0.4
Antelope Valley	0.5 +0.5/-0.3	0.6 + 0.6/-0.4	0.4 +0.4/-0.2	-	0.7 ± 0.5	1.1 ± 0.4
Mason Valley (Singatse)	0.05 ± 0.01	0.06 ± 0.01	0.04 ± 0.01	-	0.6 ± 0.5	0.4 ± 0.4
Pine Grove Hills	-	-	-	-	0.2 ± 0.6	0.6 ± 0.5

Table 2.2 Slip Rates from this study compared to block modeled rates from Bormann et al. (2016).

short rupture lengths in the Basin and Range (e.g. the 1959 M_w 7.2 Hebgen Lake earthquake produced an average displacement of 2.9 m over a 27-km-long rupture; Myers and Hamilton, 1964). If fault ruptures in this part of the Walker Lane are indeed "short", then to produce the same displacements as earthquakes with typically longer ruptures implies that these earthquakes have a high stress-drop. Hecker et al. (2010) show that faults with low slip rates and little cumulative slip, like those in the Central Walker Lane, produce particularly high static stress-drop earthquakes. Perhaps this is evidence that faults in this part of the Walker Lane are stronger than faults elsewhere in the Cordillera, which is counterintuitive to what one might expect based on the high geothermal gradient and shallow crust of this region.

Geodetic vs. geologic rates and off-fault deformation in the Central Walker Lane

In this dissertation two different methods of estimating geodetic shear are compared to geologic slip rates. The first geodetic method measures the total geodetically observed shear in a profile across a region (**Figure 2.12a**), and the second method uses the individual slip rates assigned to faults by a block model (**Table 2.2**). **Figure 2.12a** is a compilation of my dextral slip rate estimates and published geologic right-lateral slip rates across the Walker Lane (small numbers), compared to profiles of geodetic rates (rectangles) measured across the entire Walker Lane (modified after Bormann in Redwine et al., 2015). The percentages are the ratio of the sum of the geologic strike-slip rates of all of the known faults (first large number) to the total shear across a profile measured geodetically (second large number). The ratio can be thought of as the kinematic efficiency as defined by Hatem et al. 2017 and directly compared to the results of laboratory studies.

Geodetic block models generally only consider the horizontal component of the GPS velocity when solving for fault slip rates, and are therefore most reliable for measuring the horizontal strike-slip and extensional (or compressional) slip rates. Thus, an assumption of fault dip must be made to directly compare geodetic rates to the vertical separation rates measured in this study. To calculate the extensional components and down-dip slip rates of the range bounding faults in Mason, Smith, and Antelope valleys I assume that they have a simple normal fault geometry with a dip of 55 ± 10°.

The vertical separation rates and resulting extension and dip-parallel slip rates for the Walk-

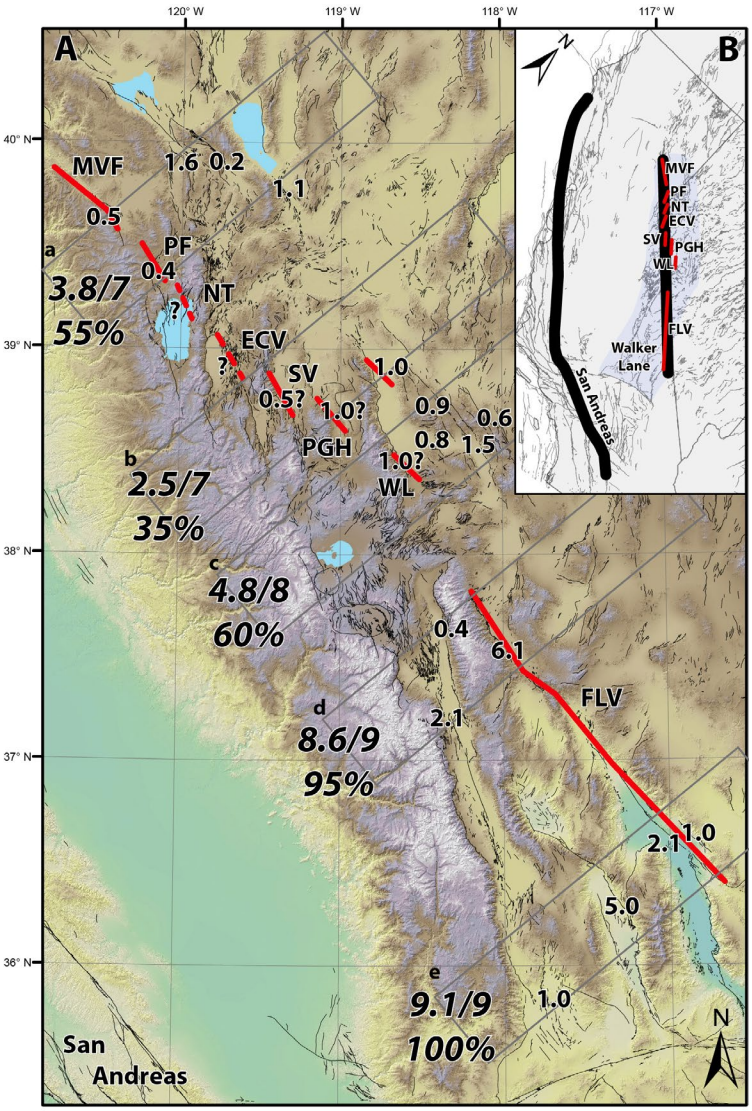

Figure 2.12 (a) Comparison of dextral shear rates measured across the Walker Lane in various profiles (gray boxes) by GPS (bold numbers), and on individual faults (smaller numbers), in mm/yr (fault slip rates from: Kirby et al., 2006; Guest et al., 2007; Frankel et al., 2011; Hunter et al., 2011; Amos et al., 2013; Gold Ryan D. et al., 2013; Dong et al., 2014; Gold et al., 2014; Angster et al., 2016; Choi, 2016; Frankel et al., 2016; Haddon et al., 2016; Gold et al., 2017). These GPS rates were provided by J. Bormann and are contained in Redwine et al. (2015). The percentages are taken by summing the rates of individual faults in each profile and dividing those by the total geodetic rate in each profile. There is good agreement between geodetic and geologic observations in the Southern Walker Lane, but less so in the Central and Northern Walker Lane. Major strike-slip fault zone discussed in this paper is highlighted by bold red lines with fault abbreviations: FLV-Fish Lake Valley, WL-Walker Lake, PGH-Pine Grove Hills, SV-Smith Valley, ECV-East Carson Valley, NT-North Tahoe, PF- Polaris Fault, MVF-Mohawk Valley. (b) Oblique oriented map of California and Nevada showing the trend of these faults as a bold black line (right) that is subparallel to the San Andreas (left black line).

er Lake and Mason, Smith, and Antelope valley range-bounding faults are listed in **Table 2.2** along with the block modeled rates for the same faults from Bormann et al. (2016). The geologic and geodetic extension rates for the Wassuks and Smith and Antelope valleys are very similar. The block modeled right-lateral rate for the Wassuk range is ~0.6 mm/yr which is similar to the geologic rate of ~1 mm/yr (Dong et al., 2014). However, the geodetic right lateral strike-slip rate of 1.1 ± 0.4 mm/yr in Antelope Valley is among the fastest rates in the region, yet lacks any observable geomorphic expression of strike-slip. The small faults on the east side of Antelope Valley with right-lateral dis-

placements do not appear sufficiently active to account for this rate. The normal slip rate estimate in Antelope Valley of $0.6\ ^{+0.6}/_{-0.4}$ mm/yr is similar to the 0.7 mm/yr estimate that Sarmiento et al. (2011) made based on the displacement measured in their trench and the inter-event time. The extension rate in Antelope Valley of $0.4\ ^{+0.4}/_{-0.2}$ is slightly less but similar to the block model rate of 0.7 ± 0.5 mm/yr (Bormann et al., 2016).

In Smith Valley, the GPS block model predicts ~0.4 mm/yr of extension and ~0.5 mm/yr of right-lateral strike-slip (Bormann et al., 2016). The geologic extension rate measured at the Artesia fan is ~0.4 mm/yr (**Table 2.2**), similar to this geodetic estimate. As this rate was measured on the edge of a large right-bend that is nearly perpendicular to the overall trend of the rangefront fault (**Figure 2.5**), this extension rate may be directly recording the lateral component of motion along the fault. Furthermore, the overall Smith Valley rangefront is much less sinuous than many normal faults in the region (**Figure 2.11**), suggesting it accommodates lateral slip.

In Mason Valley, the geologic rates of <0.05 mm/yr are an order of magnitude less than the geodetic estimate of ~0.5 mm/yr, and while the fault geometry at the Yerington Pit site allows for the accommodation of right-lateral slip, the measured geologic slip rates are close to zero. As the Singatse Range is much more subdued in topographic expression than other ranges in this region, and the rangefront generally lacks the uplifted, faulted fan surfaces common to the other faults in the region with slip rates of ~0.5 mm/yr, it seems possible that the geodetic models have not correctly partitioned the amount of slip on faults across the region, and that the much lower geologic rate seems more likely. In contrast, the fault morphology observed between the Pine Grove Hills and the southernmost part of Mason Valley appears sufficiently developed to satisfy the geodetically predicted slip rate of ~0.6 ± 0.5 mm/yr, despite any age control on displaced surfaces.

The discrepancies between geologic and geodetic slip rates in Mason and Antelope valleys may be a result of the limitations of the block model. Block models assume that all of the deformation between two adjacent blocks is constraint to a singular fault trace, which is often the only trace measurable using paleoseismic methods. However, laboratory shear models of fault systems with discontinuous geometries similar to the Walker Lane accommodate a significant portion of their total shear strain through diffused, off-fault deformation in the intervening regions between and around well-defined faults (e.g., Hatem et al., 2017), which cannot be accurately modeled as bound-

aries between rigid blocks. The laboratory models of Hatem et al. (2017) show that even mature through-going fault systems are only ~80% efficient, with ~20% of total shear accommodated by off-fault deformation, while immature systems like the Walker Lane can be less than 40% efficient, with >60% of the total shear accommodated off of faults. In the Walker Lane kinematic efficiencies vary from as little as 35% in the Central Walker Lane to ~100% in the Southern Walker Lane (**Figure 2.12a**). In this perspective, it may be speculated that the geologic slip rates in the Southern Walker Lane may be overestimated, as they do not leave any of the shear budget for off-fault deformation.

Geologically accounting for this off-fault coseismic deformation generally requires detailed pre- and post-earthquake observations of a fault system, and is therefore difficult to account for in the paleoseismic record by measuring multiple-event fault scarps (e.g., Oskin et al., 2012; Herbert et al., 2014; Gold et al., 2015; Personius et al., 2017). This deformation may manifest in different ways for each earthquake, or may be sufficiently limited in scale or diffuse that it is unlikely to be preserved on the landscape over multiple earthquake cycles. Furthermore, the orientation of some of the normal faults in the western Central Walker Lane allow for the accommodation of some of the regional shear. Thus, while only ~35% of the total shear across the Central Walker Lane is currently accounted for by summing the slip rates of known strike-slip and oblique faults, and some "on-fault" shear may still be missing, it does not appear that the sum of the lateral slip rates of the individual faults must necessarily equal the total geodetic shear across a fault system, and that both distributed shear and complex fault relationships can accommodate a significant portion of "off-fault" shear, especially in immature systems such as the Walker Lane.

Many studies of faults in the Walker Lane have shown evidence of significant temporal and spatial variations in fault geometries, slip rates, and styles of faulting (e.g., Kirby et al., 2006; Frankel et al., 2007; Gourmelen et al., 2011; Gold et al., 2013; Rittase et al., 2014). Geodetic rates are measured on a decadal timescale, whereas most geologic slip rates are over 10^4–10^5 year time scales, and if slip rates have fluctuated with time, the geodetic rates may not be representative of longer term crustal deformation. At the current ~7-8 mm/yr rate of dextral crustal shear across the Central Walker Lane, it would have taken ~4 Ma to accumulate the estimated ~30 km of total shear. This estimate fits with geologic estimates on the timing of the initiation of shear in the Northern Walker Lane occurring between 10 and 3 Ma (Faulds and Henry, 2008), and is likely a young estimate if the

rate of shear has accelerated since initiation. Few studies of geologic slip rates on timescales longer than 10^5 years have been conducted in this region, but Surpless and Kroeger (2015) show that for the Wassuk Range, slip rates have been fairly constant since ~4 Ma, are similar to the geodetic estimates, and thus decadal scale modern geodetic rates may be an accurate measure of longer term deformation in this region. As most of the block-modeled geodetic rates are in general accord with the geologic slip rates presented here, it may be suggested that the slip rates of the faults studied have been relatively constant over the Late Quaternary.

On the lack of strike-slip in the Central Walker Lane

A paleomagnetic survey of the region completed by Carlson (2017) suggests that little rotation has occurred between Antelope, Smith, and Mason valleys, while considerable rotations have accumulated in the Carson domain. The lack of rotation between Antelope and Mason valleys is further supported by the displacement distribution plots in **Figure 2.10**: if mountain ranges were actively rotating in a clockwise direction, and this rotation were accommodated by the rangefront faults, it might be expected that slip during earthquakes along the ranges would be distributed such that the largest displacements would occur near the northernmost or southernmost parts of the ranges with lesser displacements in the central portions. Repeated earthquakes with this distribution would result in greater structural relief at the northern and southern parts of ranges, but neither of these patterns are observed, and instead displacement distributions are relatively uniform with the highest relief being generally near the central portions of ranges. Strike-slip faulting should therefore accommodate any shear between these basins in the absence of significant rotations.

Well defined active strike-slip faults are observed in the Walker Lake basin (e.g. Dong et al., 2014), Truckee basin (Polaris fault; Hunter et al., 2011) and in the southern part of Mason Valley (**Figure 2.11a**). Despite the absence of discrete measurable offsets, the geometry of the Smith Valley range front fault allows that the rangefront fault accommodates a significant portion of right-lateral shear (**Figure 2.5**). DePolo and Sawyer (2005) report observing strike-slip faulting in the East Carson Valley fault zone (**Figure 2.11a**), though the rate of slip across this broad and complex zone of discontinuous faults remains undefined. The short, northeast-striking faults of the North Tahoe fault system (labeled North Tahoe in **Figure 2.11a**, including the Stateline, Incline Village, Little

Valley, and Washoe Valley faults) form an en-echelon right stepping pattern (**Figure 2.11a**) and may be considered book-shelf faults (e.g., Tapponnier et al., 1990), accommodating northwest-directed dextral shear. Thus, while slip rate indicators are not consistently preserved or recognized along all rangefronts and adjacent valleys, the geometry and pattern of faulting along with the distribution of late Quaternary slip as a function of fault strike indicates that there is a significantly larger portion of shear being accommodated by active strike-slip fault displacements than I have yet been able to quantify.

Geometry of an incipient strike-slip system

The grey band in **Figure 2.11a** highlights the series of fault systems described in the preceding section. Each of these six fault systems is ~25-km-long, and is separated from its neighboring strike-slip faults by left steps ranging in size from ~15 to 25 km. Together these fault systems form a clear en-echelon left-stepping ~25-km-wide pattern of active dextral faults extending for ~200 km from south of Walker Lake to north of Lake Tahoe.

The pattern of faults presented in **Figure 2.11a** is consistent with the early stages of models of distributed strike-slip fault systems (e.g., Schreurs, 2003; Hatem et al., 2017) such as shown in **Figure 2.11b**. This model produces a discontinuous pattern of left-stepping Riedel shears that form en-echelon extensional basins and dextral faults similar to what is observed in the Central Walker Lane (Atmaoui et al., 2006). All of the faults in these models begin as extensional cracks. Aydin and Nur (1982) show that pull-apart basins in a strike-slip system are largely a result of step overs of en-echelon strike-slip faults, which is consistent with the pattern of faulting observed in the Central Walker Lane. Thus, the majority of north-striking normal faulting along a number of the ranges in this region is driven by northwest directed dextral shear along discrete faults, similar to these experimental models (e.g., Aydin and Nur, 1982; Atmaoui et al., 2006). In this light the westward decrease in inception age and total magnitude of extension and normal faulting from the Wassuk Range to the Sierra Nevada may be evidence for the encroachment of strike-slip faulting through this region.

When viewed in large scale the pattern of strike-slip faulting in the Central Walker Lane falls on strike with both the Mohawk Valley and the Death Valley/Fish Lake Valley faults (**Figures 2.1 and 2.12**), which are among the most active strike-slip faults of the Northern and Southern

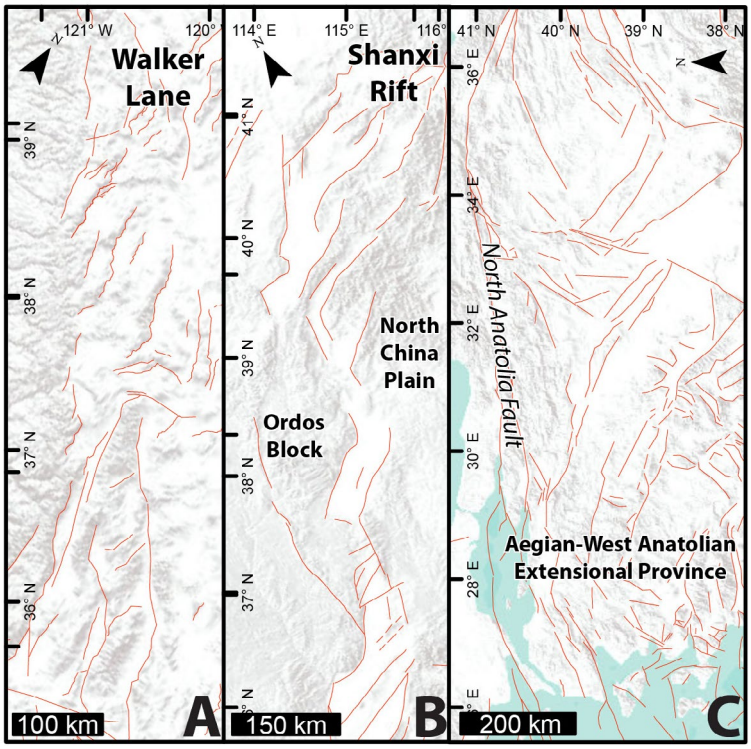

Figure 2.13 Fault pattern of the Walker Lane (a) compared to the Shanxi Rift of China (b) and the Aegian-West Anatolian Extensional Province of Turkey (c). All maps are oriented so that the major dextral shear directions are subparallel.

Walker Lane, respectively. Laboratory models predict that as displacement accumulates across fault systems, initial distributed faulting will eventually organize into a single through going strike-slip fault. The trend of faults illustrated by the right bold line in **Figure 2.12b** forms a linear, >500-km-long fault zone that is nearly parallel to the San Andreas fault, and eventually this may be the trace of a continuous strike-slip fault, accommodating much of the strain across the Pacific-North American plate boundary. However, fault complexity is not solely a result of total shear accumulated across a fault zone, as faults largely take advantage of pre-existing crustal weaknesses (e.g., Molnar, 1988; Ziegler et al., 1998; Matenco et al., 2007; Dyksterhuis and Müller, 2008; Aitken et al., 2013; Raimondo et al., 2014; Calzolari et al., 2016), which in the Walker Lane may have been inherited from an earlier episode of Basin and Range extension, prior to initiation of the current Walker Lane strain regime (Surpless et al., 2002), or even earlier structural irregularities (e.g. Faulds and Henry, 2008).

The nuances in the structural evolution of transtensional systems are highlighted here by two other transtensional fault systems that are analogous to the Walker Lane: the Shanxi Rift system of China, and the Aegean-West Anatolian extensional province of Turkey (**Figure 2.13**). The Shanxi

Rift forms a ~650-km-long by 100-km-wide zone of discontinuous northeast trending normal and strike-slip faults, where the relatively stable Ordos block is moving obliquely relative to the North China plain (**Figure 2.13b**) at a current relative geodetic rate of ~2 mm/yr (Zhao et al., 2017). While the Shanxi Rift has only accumulated ~10 km of total shear (Xu et al., 1993), much less than the Walker Lane, these two systems have similar fault patterns of discontinuous, en-echelon strike-slip and normal faults. The Aegean-West Anatolian extensional province (**Figure 2.13c**) of Turkey is a complex series of strike-slip and normal faults extending to the south of the North Anatolia fault (e.g. Faulds et al., 2009). A north-south oriented GPS profile across this province shows that ~5-10 mm/yr of east-directed dextral shear and ~20 mm/yr of north-direct extension is accommodated over a width of ~300 km (Figure 9b in Aktug et al., 2009). Although I are unaware of any estimates of cumulative shear across this broad province, and the rate of extension is an order of magnitude higher than the Walker Lane, the pattern of faulting and rate of distributed shear in this province are both analogous to the Walker Lane (**Figure 2.13**). Total cumulative slip in all three of these systems is limited, and the transtension accommodated by each system forms a similar pattern of broad, complex, discontinuous faulting.

Conclusions

- Slip rates of normal faulting for the Antelope, Smith, and Mason valley rangefront faults are $0.6\ ^{+0.7}/_{-0.3}$, $0.7\ ^{+1.0}/_{-0.4}$, and <0.05 mm/yr, respectively.
- Preservation of geomorphic features indicating strike-slip faulting are lacking along the Antelope and Mason valley rangefront faults.
- A large component of strike slip is indicated along the Smith Valley fault by a correlation of scarp size and preservation to variations in fault strike.
- Scarp height distributions measured from lidar along the Smith and Antelope valley range bounding faults agree well with observations from previous paleoseismic trenches, with single event displacements of ~3 m for both faults that correspond with earthquakes of ~M_w 7.
- Discrete strike-slip faults previously unrecognized are described in the southern parts of Mason Valley and the Walker Lake basin.

- Significant geodetically observed shear remains unaccounted for by summing geologic slip rates, but is likely accommodated by off-fault deformation and complex rupture patterns.
- Shear in the western part of the Central Walker Lane is accommodated along a system of short, left-stepping en-echelon dextral and normal faults extending from south of Walker Lake to north of Lake Tahoe. Together this system of faults forms a pattern similar to the initial stages of laboratory models of dextral shear, and may evolve into a through-going strike-slip fault in the future.

Acknowledgements

This research was supported in part by National Science Foundation grant EAR-1419724 and EAR-1419789 and by USGS grant G15AP00088. Any use of trade, firm, or product names is for descriptive purposes only and does not imply endorsement. I thank Paula Figueiredo and Sarah Hammer for assistance in processing and calculating TCN ages, and the National Center for Airborne Laser Mapping (NCALM) for collecting lidar data. Thanks to Steve Angster, Tabor Reedy, Chad Carlson, Noah Abramson, Annie Kell, Colin Chupik, Jayne Bormann, Bill Hammond, Ken Adams, and Rachel Hatch for assisting in the field, lab, and numerous enlightening discussions. Thanks to the 2017 UNR Neotectonics class for assistance in the field. Thanks to Rich Koehler for editing an early version of this dissertation. This is Center for Neotectonics Studies contribution number 78.

References

Adams, K.D., Wesnousky, S.G., 1998. Shoreline processes and the age of the Lake Lahontan high-stand in the Jessup embayment, Nevada. Geol. Soc. Am. Bull. 110, 1318–1332.

Aitken, A.R.A., Raimondo, T., Capitanio, F.A., 2013. The intraplate character of supercontinent tectonics. Gondwana Res. 24, 807–814. https://doi.org/10.1016/j.gr.2013.03.005

Aktug, B., Nocquet, J.M., Cingöz, A., Parsons, B., Erkan, Y., England, P., Lenk, O., Gürdal, M.A., Kilicoglu, A., Akdeniz, H., Tekgül, A., 2009. Deformation of western Turkey from a com-

bination of permanent and campaign GPS data: Limits to block-like behavior. J. Geophys. Res. Solid Earth 114. https://doi.org/10.1029/2008JB006000

Ambraseys, N.N., Tchalenko, J.S., 1972. Seismotectonic Aspects of the Gediz, Turkey, Earthquake of March 1970. Geophys. J. R. Astron. Soc. 30, 229–252. https://doi.org/10.1111/j.1365-246X.1972.tb05811.x

Amos, C.B., Brownlee, S.J., Rood, D.H., Fisher, G.B., Burgmann, R., Renne, P.R., Jayko, A.S., 2013. Chronology of tectonic, geomorphic, and volcanic interactions and the tempo of fault slip near Little Lake, California. Geol. Soc. Am. Bull. 125, 1187–1202. https://doi.org/10.1130/B30803.1

An, L.-J., Sammis, C.G., 1996. Development of strike-slip faults: shear experiments in granular materials and clay using a new technique. J. Struct. Geol. 18, 1061–1077. https://doi.org/10.1016/0191-8141(96)00012-0

Angster, S., Wesnousky, S., Figueiredo, P., Owen, L.A., Hammer, S., 2019. Late Quaternary slip rates for faults of the Central Walker Lane: Spatiotemporal strain release in a strike-slip fault system. Geosphere 57.

Angster, S., Wesnousky, S., Huang, W., Kent, G., Nakata, T., Goto, H., 2016. Application of UAV Photography to Refining the Slip Rate on the Pyramid Lake Fault Zone, Nevada. Bull. Seismol. Soc. Am. 106, 785–798. https://doi.org/10.1785/0120150144

Atmaoui, N., Kukowski, N., Stöckhert, B., König, D., 2006. Initiation and development of pull-apart basins with Riedel shear mechanism: insights from scaled clay experiments. Int. J. Earth Sci. 95, 225–238. https://doi.org/10.1007/s00531-005-0030-1

Aydin, A., Nur, A., 1982. Evolution of pull-apart basins and their scale independence. Tectonics 1, 91–105. https://doi.org/10.1029/TC001i001p00091

Balco, G., Stone, J.O., Lifton, N.A., Dunai, T.J., 2008. A complete and easily accessible means of calculating surface exposure ages or erosion rates from 10Be and 26Al measurements. Quat. Geochronol. 3, 174–195. https://doi.org/10.1016/j.quageo.2007.12.001

Beanland, S., Clark, M.M., 1994. The Owens Valley Fault Zone, Eastern California, and Surface Faulting Associated with the 1872 Earthquake (U.S. Geological Survey Bulletin No. 1982). U.S. Geological Survey.

Bell, J.W., Caskey, S.J., Ramelli, A.R., Guerrieri, L., 2004. Pattern and rates of faulting in the central Nevada seismic belt, and paleoseismic evidence for prior beltlike behavior. Bull. Seismol. Soc. Am. 94, 1229–1254.

Bell, J.W., dePolo, C.M., Ramelli, A.R., Sarna-Wojcicki, A.M., Meyer, C.E., 1999. Surface faulting and paleoseismic history of the 1932 Cedar Mountain earthquake area, west-central Nevada, and implications for modern tectonics of the Walker Lane. Geol. Soc. Am. Bull. 111, 791–807. https://doi.org/10.1130/0016-7606(1999)111<0791:SFAPHO>2.3.CO;2

Bennett, R.A., Wernicke, B.P., Niemi, N.A., Friedrich, A.M., Davis, J.L., 2003. Contemporary strain rates in the northern Basin and Range province from GPS data. Tectonics 22, 31 pp. https://doi.org/10.1029/2001TC001355

Borchers, B., Marrero, S., Balco, G., Caffee, M., Goehring, B., Lifton, N., Nishiizumi, K., Phillips, F., Schaefer, J., Stone, J., 2016. Geological calibration of spallation production rates in the CRONUS-Earth project. Quat. Geochronol. 31, 188–198. https://doi.org/10.1016/j.quageo.2015.01.009

Bormann, J.M., Hammond, W.C., Kreemer, C., Blewitt, G., 2016. Accommodation of missing shear strain in the Central Walker Lane, western North America: Constraints from dense GPS measurements. Earth Planet. Sci. Lett. 440, 169–177. https://doi.org/10.1016/j.epsl.2016.01.015

Bormann, J.M., Surpless, B.E., Caffee, M.W., Wesnousky, S.G., 2012. Holocene Earthquakes and Late Pleistocene Slip-Rate Estimates on the Wassuk Range Fault Zone, Nevada. Bull. Seismol. Soc. Am. 102, 1884–1891. https://doi.org/10.1785/0120110287

Briggs, R.W., 2005. Late Pleistocene and Holocene Paleoearthquake Activity of the Olinghouse Fault Zone, Nevada. Bull. Seismol. Soc. Am. 95, 1301–1313. https://doi.org/10.1785/0120040129

Briggs, R.W., 2004. Late Pleistocene fault slip rate, earthquake recurrence, and recency of slip along the Pyramid Lake fault zone, northern Walker Lane, United States. J. Geophys. Res. 109. https://doi.org/10.1029/2003JB002717

Calzolari, G., Rossetti, F., Seta, M.D., Nozaem, R., Olivetti, V., Balestrieri, M.L., Cosentino, D., Faccenna, C., Stuart, F.M., Vignaroli, G., 2016. Spatio-temporal evolution of intraplate

strike-slip faulting: The Neogene–Quaternary Kuh-e-Faghan Fault, central Iran. GSA Bull. 128, 374–396. https://doi.org/10.1130/B31266.1

Carlson, C., 2017. Kinematics and Transfer Mechanisms of Strain Accommodation at the Transition between the Northern and Central Walker Lane, Western Nevada (Doctoral Dissertation). University of Nevada, Reno, Reno, NV.

Cashman, P.H., Fontaine, S.A., 2000. Strain partitioning in the northern Walker Lane, western Nevada and northeastern California. Tectonophysics 326, 111–130.

Choi, N.H., 2016. Late Pleistocene Slip Rate along the Panamint Valley Fault System, Eastern California (Masters Thesis). Oregon State University.

dePolo, C.M., Sawyer, T., 2005. Paleoseismic studies along the Eastern Carson Valley fault system (Final Technical Report), U.S. Geological Survey National Hazards Reduction Program.

Dixon, T.H., Miller, M., Farina, F., Wang, H., Johnson, D., 2000. Present-day motion of the Sierra Nevada block and some tectonic implications for the Basin and Range province, North American Cordillera. Tectonics 19, 1–24.

Dong, S., Ucarkus, G., Wesnousky, S.G., Maloney, J., Kent, G., Driscoll, N., Baskin, R., 2014. Strike-slip faulting along the Wassuk Range of the northern Walker Lane, Nevada. Geosphere 10, 40–48.

Dyksterhuis, S., Müller, R.D., 2008. Cause and evolution of intraplate orogeny in Australia. Geology 36, 495–498. https://doi.org/10.1130/G24536A.1

Faulds, J.E., Bouchot, V., Moeck, I., Oguz, K., 2009. Structural Controls on Geothermal Systems in Western Turkey: A Preliminary Report 33, 8.

Faulds, J.E., Henry, C.D., 2008. Tectonic influences on the spatial and temporal evolution of the Walker Lane: An incipient transform fault along the evolving Pacific – North American plate boundary 34.

Faulds, J.E., Henry, C.D., Hinz, N.H., 2005. Kinematics of the northern Walker Lane: An incipient transform fault along the Pacific–North American plate boundary. Geology 33, 505–508.

Frankel, K.L., Dolan, J.F., Finkel, R.C., Owen, L.A., Hoeft, J.S., 2007. Spatial variations in slip rate along the Death Valley-Fish Lake Valley fault system determined from LiDAR topographic data and cosmogenic 10Be geochronology. Geophys. Res. Lett. 34. https://doi.

org/10.1029/2007GL030549

Frankel, K.L., Dolan, J.F., Owen, L.A., Ganev, P., Finkel, R.C., 2011. Spatial and temporal constancy of seismic strain release along an evolving segment of the Pacific–North America plate boundary. Earth Planet. Sci. Lett. 304, 565–576. https://doi.org/10.1016/j.epsl.2011.02.034

Frankel, K.L., Owen, L.A., Dolan, J.F., Knott, J.R., Lifton, Z.M., Finkel, R.C., Wasklewicz, T., 2016. Timing and rates of Holocene normal faulting along the Black Mountains fault zone, Death Valley, USA. Lithosphere 8, 3–22. https://doi.org/10.1130/L464.1

Ganev, P.N., Dolan, J.F., Frankel, K.L., Finkel, R.C., 2010. Rates of extension along the Fish Lake Valley fault and transtensional deformation in the Eastern California shear zone–Walker Lane belt. Lithosphere 2, 33–49. https://doi.org/10.1130/L51.1

Gilbert, C.M., Reynolds, M.W., 1973. Character and Chronology of Basin Development, Western Margin of the Basin and Range Province. Geol. Soc. Am. Bull. 84, 2489. https://doi.org/10.1130/0016-7606(1973)84<2489:CACOBD>2.0.CO;2

Gold, R., dePolo, C., Briggs, R., Crone, A., Gosse, J., 2013. Late Quaternary Slip-Rate Variations along the Warm Springs Valley Fault System, Northern Walker Lane, California–Nevada Border. Bull. Seismol. Soc. Am. 103, 542–558. https://doi.org/10.1785/0120120020

Gold, R.D., Briggs, R.W., Crone, A.J., DuRoss, C.B., 2017. Refining fault slip rates using multiple displaced terrace risers—An example from the Honey Lake fault, NE California, USA. Earth Planet. Sci. Lett. 477, 134–146. https://doi.org/10.1016/j.epsl.2017.08.021

Gold, R.D., Briggs, R.W., Personius, S.F., Crone, A.J., Mahan, S.A., Angster, S.J., 2014. Latest Quaternary paleoseismology and evidence of distributed dextral shear along the Mohawk Valley fault zone, northern Walker Lane, California: Paleoseismology Mohawk Valley fault zone. J. Geophys. Res. Solid Earth 119, 5014–5032. https://doi.org/10.1002/2014JB010987

Gold, R.D., Reitman, N.G., Briggs, R.W., Barnhart, W.D., Hayes, G.P., Wilson, E., 2015. On- and off-fault deformation associated with the September 2013 Mw 7.7 Balochistan earthquake: Implications for geologic slip rate measurements. Tectonophysics. https://doi.org/10.1016/j.tecto.2015.08.019

Gold Ryan D., Stephenson William J., Odum Jack K., Briggs Richard W., Crone Anthony J., Angster Stephen J., 2013. Concealed Quaternary strike-slip fault resolved with airborne lidar

and seismic reflection: The Grizzly Valley fault system, northern Walker Lane, California. J. Geophys. Res. Solid Earth 118, 3753–3766. https://doi.org/10.1002/jgrb.50238

Gosse, J.C., Phillips, F.M., 2001. Terrestrial in situ cosmogenic nuclides: theory and application. Quat. Sci. Rev. 20, 1475–1560.

Gourmelen, N., Dixon, T.H., Amelung, F., Schmalzle, G., 2011. Acceleration and evolution of faults: An example from the Hunter Mountain–Panamint Valley fault zone, Eastern California. Earth Planet. Sci. Lett. 301, 337–344. https://doi.org/10.1016/j.epsl.2010.11.016

Guest, B., Niemi, N., Wernicke, B., 2007. Stateline fault system: A new component of the Miocene-Quaternary Eastern California shear zone. GSA Bull. 119, 1337–1347. https://doi.org/10.1130/0016-7606(2007)119[1337:SFSANC]2.0.CO;2

Haddon, E.K., Amos, C.B., Zielke, O., Jayko, A.S., Bürgmann, R., 2016. Surface slip during large Owens Valley earthquakes. Geochem. Geophys. Geosystems 17, 2239–2269. https://doi.org/10.1002/2015GC006033

Hamling, I.J., Hreinsdóttir, S., Clark, K., Elliott, J., Liang, C., Fielding, E., Litchfield, N., Villamor, P., Wallace, L., Wright, T.J., D'Anastasio, E., Bannister, S., Burbidge, D., Denys, P., Gentle, P., Howarth, J., Mueller, C., Palmer, N., Pearson, C., Power, W., Barnes, P., Barrell, D.J.A., Dissen, R.V., Langridge, R., Little, T., Nicol, A., Pettinga, J., Rowland, J., Stirling, M., 2017. Complex multifault rupture during the 2016 Mw 7.8 Kaikōura earthquake, New Zealand. Science 356, eaam7194. https://doi.org/10.1126/science.aam7194

Hammond, W.C., Blewitt, G., Kreemer, C., 2011. Block modeling of crustal deformation of the northern Walker Lane and Basin and Range from GPS velocities. J. Geophys. Res. 116. https://doi.org/10.1029/2010JB007817

Hammond, W.C., Thatcher, W., 2007. Crustal deformation across the Sierra Nevada, northern Walker Lane, Basin and Range transition, western United States measured with GPS, 2000–2004. J. Geophys. Res. 112. https://doi.org/10.1029/2006JB004625

Hammond, W.C., Thatcher, W., 2005. Northwest Basin and Range tectonic deformation observed with the Global Positioning System, 1999–2003. J. Geophys. Res. 110. https://doi.org/10.1029/2005JB003678

Hanks, T.C., Kanamori, H., 1979. A moment magnitude scale. J. Geophys. Res. Solid Earth 84,

2348–2350. https://doi.org/10.1029/JB084iB05p02348

Hatem, A.E., Cooke, M.L., Toeneboehn, K., 2017. Strain localization and evolving kinematic efficiency of initiating strike-slip faults within wet kaolin experiments. J. Struct. Geol. 101, 96–108. https://doi.org/10.1016/j.jsg.2017.06.011

Hecker, S., Dawson, T.E., Schwartz, D.P., 2010. Normal-Faulting Slip Maxima and Stress-Drop Variability: A Geological PerspectiveNormal-Faulting Slip Maxima and Stress-Drop Variability: A Geological Perspective. Bull. Seismol. Soc. Am. 100, 3130–3147. https://doi.org/10.1785/0120090356

Herbert, J.W., Cooke, M.L., Oskin, M., Difo, O., 2014. How much can off-fault deformation contribute to the slip rate discrepancy within the eastern California shear zone? Geology 42, 71–75. https://doi.org/10.1130/g34738.1

Hidy, A.J., Gosse, J.C., Pederson, J.L., Mattern, J.P., Finkel, R.C., 2010. A geologically constraint Monte Carlo approach to modeling exposure ages from profiles of cosmogenic nuclides: An example from Lees Ferry, Arizona. Geochem. Geophys. Geosystems 11. https://doi.org/10.1029/2010GC003084

Hunter, L.E., Howle, J.F., Rose, R.S., Bawden, G.W., 2011. LiDAR-Assisted Identification of an Active Fault near Truckee, California. Bull. Seismol. Soc. Am. 101, 1162–1181. https://doi.org/10.1785/0120090261

Kaneda, H., Okada, A., 2008. Long-Term Seismic Behavior of a Fault Involved in a Multiple-Fault Rupture: Insights from Tectonic Geomorphology along the Neodani Fault, Central Japan. Bull. Seismol. Soc. Am. 98, 2170–2190. https://doi.org/10.1785/0120070204

Kent, G.M., Babcock, J.M., Driscoll, N.W., Harding, A.J., Dingler, J.A., Seitz, G.G., Gardner, J.V., Mayer, L.A., Goldman, C.R., Heyvaert, A.C., Richards, R.C., Karlin, R., Morgan, C.W., Gayes, P.T., Owen, L.A., 2005. 60 k.y. record of extension across the western boundary of the Basin and Range province: Estimate of slip rates from offset shoreline terraces and a catastrophic slide beneath Lake Tahoe. Geology 33, 365–368. https://doi.org/10.1130/G21230.1

Kirby, E., Anandakrishnan, S., Phillips, F., Marrero, S., 2008. Late Pleistocene slip rate along the Owens Valley fault, eastern California. Geophys. Res. Lett. 35. https://doi.

org/10.1029/2007GL031970

Kirby, E., Burbank, D.W., Reheis, M., Phillips, F., 2006. Temporal variations in slip rate of the White Mountain Fault Zone, Eastern California. Earth Planet. Sci. Lett. 248, 168–185. https://doi.org/10.1016/j.epsl.2006.05.026

Koehler, R.D., Wesnousky, S.G., 2011. Late Pleistocene regional extension rate derived from earthquake geology of late Quaternary faults across the Great Basin, Nevada, between 38.5° N and 40° N latitude. Geol. Soc. Am. Bull. 123, 631–650.

Kohl, C.P., Nishiizumi, K., 1992. Chemical isolation of quartz for measurement of in-situ-produced cosmogenic nuclides. Geochim. Cosmochim. Acta 56, 3583–3587.

Lal, D., 1991. Cosmic ray labeling of erosion surfaces: in situ nuclide production rates and erosion models. Earth Planet. Sci. Lett. 104, 424–439.

Lee, J., Spencer, J., Owen, L., 2001. Holocene slip rates along the Owens Valley fault, California: Implications for the recent evolution of the Eastern California Shear Zone. Geology 29, 819–822. https://doi.org/10.1130/0091-7613(2001)029<0819:HSRATO>2.0.CO;2

Li, X., Huang, W., Pierce, I.K.D., Angster, S.J., Wesnousky, S.G., 2017. Characterizing the Quaternary expression of active faulting along the Olinghouse, Carson, and Wabuska lineaments of the Walker Lane. Geosphere 13, 2119–2136. https://doi.org/10.1130/GES01483.1

Lifton, N., 2016. Implications of two Holocene time-dependent geomagnetic models for cosmogenic nuclide production rate scaling. Earth Planet. Sci. Lett. 433, 257–268. https://doi.org/10.1016/j.epsl.2015.11.006

Link, M.H., Roberts, M.T., Newton, M.S., 1985. Walker Lake Basin, Nevada: An Example of Late Tertiary (?) to Recent Sedimentation in a Basin Adjacent to an Active Strike-Slip Fault, in: Strike-Slip Deformation, Basin Formation, and Sedimentation. Society for Sedimentary Geology.

Maloney, J.M., Noble, P.J., Driscoll, N.W., Kent, G.M., Smith, S.B., Schmauder, G.C., Babcock, J.M., Baskin, R.L., Karlin, R., Kell, A.M., Seitz, G.G., Zimmerman, S., Kleppe, J.A., 2013. Paleoseismic history of the Fallen Leaf segment of the West Tahoe-Dollar Point fault reconstructed from slide deposits in the Lake Tahoe Basin, California-Nevada. Geosphere 9, 1065–1090. https://doi.org/10.1130/GES00877.1

Mann, P., 2007. Global catalogue, classification and tectonic origins of restraining- and releasing bends on active and ancient strike-slip fault systems. Geol. Soc. Lond. Spec. Publ. 290, 13–142. https://doi.org/10.1144/SP290.2

Martin, L.C.P., Blard, P.-H., Balco, G., Lavé, J., Delunel, R., Lifton, N., Laurent, V., 2017. The CREp program and the ICE-D production rate calibration database: A fully parameterizable and updated online tool to compute cosmic-ray exposure ages. Quat. Geochronol. 38, 25–49. https://doi.org/10.1016/j.quageo.2016.11.006

Matenco, L., Bertotti, G., Leever, K., Cloetingh, S., Schmid, S.M., Tărăpoancă, M., Dinu, C., 2007. Large-scale deformation in a locked collisional boundary: Interplay between subsidence and uplift, intraplate stress, and inherited lithospheric structure in the late stage of the SE Carpathians evolution. Tectonics 26. https://doi.org/10.1029/2006TC001951

Molnar, P., 1988. Continental tectonics in the aftermath of plate tectonics. Nature 335, 131. https://doi.org/10.1038/335131a0

Myers, W.B., Hamilton, W., 1964. The Hebgen Lake, Montana, earthquake of August 17, 1959 (No. 435– I), Geological Survey Professional Paper.

Nishiizumi, K., Winterer, E.L., Kohl, C.P., Klein, J., Middleton, R., Lal, D., Arnold, J.R., 1989. Cosmic ray production rates of 10Be and 26Al in quartz from glacially polished rocks. J. Geophys. Res. Solid Earth 94, 17907–17915. https://doi.org/10.1029/JB094iB12p17907

Oskin, M.E., Arrowsmith, J.R., Corona, A.H., Elliott, A.J., Fletcher, J.M., Fielding, E.J., Gold, P.O., Garcia, J.J.G., Hudnut, K.W., Liu-Zeng, J., Teran, O.J., 2012. Near-Field Deformation from the El Mayor–Cucapah Earthquake Revealed by Differential LIDAR. Science 335, 702–705. https://doi.org/10.1126/science.1213778

Personius, S.F., Briggs, R.W., Maharrey, J.Z., Angster, S.J., Mahan, S.A., 2017. A paleoseismic transect across the northwestern Basin and Range Province, northwestern Nevada and northeastern California, USA. Geosphere 13, 782–810. https://doi.org/10.1130/GES01380.1

Pierce, I.K.D., Wesnousky, S.G., Owen, L.A., 2017. Terrestrial cosmogenic surface exposure dating of moraines at Lake Tahoe in the Sierra Nevada of California and slip rate estimate for the West Tahoe Fault. Geomorphology 298, 63–71. https://doi.org/10.1016/j.geomorph.2017.09.030

Raimondo, T., Hand, M., Collins, W.J., 2014. Compressional intracontinental orogens: Ancient and modern perspectives. Earth-Sci. Rev. 130, 128–153. https://doi.org/10.1016/j.earscirev.2013.11.009

Ramelli, A.R., Bell, J.W., dePolo, C.M., Yount, J.C., 1999. Large-magnitude, late Holocene earthquakes on the Genoa fault, west-central Nevada and eastern California. Bull. Seismol. Soc. Am. 89, 1458–1472.

Redwine, J., Wakabayashi, J., Sawyer, T., Bormann, J.M., Kemp, C., Humphrey, J., Unruh, J., Briggs, R.W., Adams, K.D., Ramelli, A.R., Gold, R.D., Burke, R.M., 2015. The 2015 Annual Pacific Cell Friends of the Pleistocene field trip. From Mohawk Valley to Caribou Junction Middle and North Forks of the Feather River, northeastern California (Field Trip Guide).

Reheis, M., 1999. Extent of Pleistocene Lakes in the Western Great Basin. Miscellaneous Field Studies.

Rittase, W.M., Kirby, E., McDonald, E., Walker, J.D., Gosse, J., Spencer, J.Q.G., Herrs, A.J., 2014. Temporal variations in Holocene slip rate along the central Garlock fault, Pilot Knob Valley, California. Lithosphere 6, 48–58. https://doi.org/10.1130/L286.1

Rood, D.H., Burbank, D.W., Finkel, R.C., 2011. Spatiotemporal patterns of fault slip rates across the Central Sierra Nevada frontal fault zone. Earth Planet. Sci. Lett. 301, 457–468. https://doi.org/10.1016/j.epsl.2010.11.006

Sarmiento, A.C., Wesnousky, S.G., Bormann, J.M., 2011. Paleoseismic Trenches across the Sierra Nevada and Carson Range Fronts in Antelope Valley, California, and Reno, Nevada. Bull. Seismol. Soc. Am. 101, 2542–2549. https://doi.org/10.1785/0120100176

Schreurs, G., 2003. Fault development and interaction in distributed strike-slip shear zones: an experimental approach. Geol. Soc. Lond. Spec. Publ. 210, 35–52. https://doi.org/10.1144/GSL.SP.2003.210.01.03

Seitz, G.G., Kent, G., 2014. Closing the Gap between on and Offshore Paleoseismic Records in the Lake Tahoe Basin (Final Technical Report), U.S. Geological Survey National Hazards Reduction Program.

Stauffer, H., 2003. Timing of the Last Highstand of Pluvial Lake Wellington, Smith Valley, Nevada (Master's Thesis). San Jose State University.

Stirling, M.W., Wesnousky, S.G., Shimazaki, K., 1996. Fault trace complexity, cumulative slip, and the shape of the magnitude-frequency distribution for strike-slip faults: a global survey. Geophys. J. Int. 124, 833–868. https://doi.org/10.1111/j.1365-246X.1996.tb05641.x

Stockli, D.F., Dumitru, T.A., McWilliams, M.O., Farley, K.A., 2003. Cenozoic tectonic evolution of the White Mountains, California and Nevada. Geol. Soc. Am. Bull. 115, 788–816.

Stone, J.O., 2000. Air pressure and cosmogenic isotope production. J. Geophys. Res. 105, 23,753-23,759.

Surpless, B., Kroeger, G., 2015. The unusual temporal and spatial slip history of the Wassuk Range normal fault, western Nevada (USA): Implications for seismic hazard and Walker Lane deformation. Geol. Soc. Am. Bull. 127, 737–758. https://doi.org/10.1130/B31159.1

Surpless, B.E., Stockli, D.F., Dumitru, T.A., Miller, E.L., 2002. Two-phase westward encroachment of Basin and Range extension into the northern Sierra Nevada. Tectonics 21, 2-1-2–10. https://doi.org/10.1029/2000tc001257

Tapponnier, P., Armijo, R., Manighetti, I., Courtillot, V., 1990. Bookshelf faulting and horizontal block rotations between overlapping rifts in southern Afar. Geophys. Res. Lett. 17, 1–4. https://doi.org/10.1029/GL017i001p00001

Thatcher, W., Foulger, G.R., Julian, B.R., Svarc, J., Quilty, E., Bawden, G.W., 1999. Present-Day Deformation Across the Basin and Range Province, Western United States. Science 283, 1714–1717.

Unruh, J., Humphrey, J., Barron, A., 2003. Transtensional model for the Sierra Nevada frontal fault system, eastern California. Geology 31, 327–330.

Uppala, S.M., KAllberg, P.W., Simmons, A.J., Andrae, U., Bechtold, V.D.C., Fiorino, M., Gibson, J.K., Haseler, J., Hernandez, A., Kelly, G.A., Li, X., Onogi, K., Saarinen, S., Sokka, N., Allan, R.P., Andersson, E., Arpe, K., Balmaseda, M.A., Beljaars, A.C.M., Berg, L.V.D., Bidlot, J., Bormann, N., Caires, S., Chevallier, F., Dethof, A., Dragosavac, M., Fisher, M., Fuentes, M., Hagemann, S., H?lm, E., Hoskins, B.J., Isaksen, L., Janssen, P.A.E.M., Jenne, R., Mcnally, A.P., Mahfouf, J.-F., Morcrette, J.-J., Rayner, N.A., Saunders, R.W., Simon, P., Sterl, A., Trenberth, K.E., Untch, A., Vasiljevic, D., Viterbo, P., Woollen, J., 2005. The ERA-40 re-analysis. Q. J. R. Meteorol. Soc. 131, 2961–3012. https://doi.org/10.1256/qj.04.176

Wesnousky, S.G., 2008. Displacement and Geometrical Characteristics of Earthquake Surface Ruptures: Issues and Implications for Seismic-Hazard Analysis and the Process of Earthquake Rupture. Bull. Seismol. Soc. Am. 98, 1609–1632. https://doi.org/10.1785/0120070111

Wesnousky, S.G., 2005. Active faulting in the Walker Lane. Tectonics 24, 35 pp. https://doi.org/10.1029/2004TC001645

Wesnousky, S.G., 1988. Seismological and structural evolution of strike-slip faults. Nature 335, 340. https://doi.org/10.1038/335340a0

Wesnousky, S.G., Bormann, J.M., Kreemer, C., Hammond, W.C., Brune, J.N., 2012. Neotectonics, geodesy, and seismic hazard in the Northern Walker Lane of Western North America: Thirty kilometers of crustal shear and no strike-slip? Earth Planet. Sci. Lett. 329–330, 133–140. https://doi.org/10.1016/j.epsl.2012.02.018

Wesnousky, S.G., Caffee, M., 2011. Range-Bounding Normal Fault of Smith Valley, Nevada: Limits on Age of Last Surface-Rupture Earthquake and Late Pleistocene Rate of Displacement. Bull. Seismol. Soc. Am. 101, 1431–1437. https://doi.org/10.1785/0120100238

Wilcox, R.E., Harding, T.P., Seely, D.R., 1973. Basic wrench tectonics. AAPG Bull. 57, 74–96.

Wintle, A.G., Murray, A.S., 2006. A review of quartz optically stimulated luminescence characteristics and their relevance in single-aliquot regeneration dating protocols. Radiat. Meas. 41, 369–391. https://doi.org/10.1016/j.radmeas.2005.11.001

Xu, X., Ma, X., Deng, Q., 1993. Neotectonic activity along the Shanxi rift system, China. Tectonophysics 219, 305–325. https://doi.org/10.1016/0040-1951(93)90180-R

Zechar, J.D., Frankel, K.L., 2009. Incorporating and reporting uncertainties in fault slip rates. J. Geophys. Res. Solid Earth 114, B12407. https://doi.org/10.1029/2009JB006325

Zhao, B., Zhang, C., Wang, D., Huang, Y., Tan, K., Du, R., Liu, J., 2017. Contemporary kinematics of the Ordos block, North China and its adjacent rift systems constraint by dense GPS observations. J. Asian Earth Sci. 135, 257–267. https://doi.org/10.1016/j.jseaes.2016.12.045

Ziegler, P.A., van Wees, J.-D., Cloetingh, S., 1998. Mechanical controls on collision-related compressional intraplate deformation. Tectonophysics 300, 103–129. https://doi.org/10.1016/S0040-1951(98)00236-4

Zinke, R., Dolan, J.F., Dissen, R.V., Grenader, J.R., Rhodes, E.J., McGuire, C.P., Langridge, R.M.,

Nicol, A., Hatem, A.E., 2015. Evolution and progressive geomorphic manifestation of surface faulting: A comparison of the Wairau and Awatere faults, South Island, New Zealand. Geology 43, 1019–1022. https://doi.org/10.1130/G37065.1

Zuza, A.V., Yin, A., Lin, J., Sun, M., 2017. Spacing and strength of active continental strike-slip faults. Earth Planet. Sci. Lett. 457, 49–62. https://doi.org/10.1016/j.epsl.2016.09.041

Appendix

Contents:

1. TCN Geochronology Laboratory Methods

^{10}Be

All samples were processed at the Cosmogenic Dating Preparation Laboratories at the University of Cincinnati following the methods of Kohl and Nishiizumi (1992). Samples were first crushed and sieved to acquire the 250-500 μm size fraction. These were rinsed in recycled aqua regia to remove any organics or carbonates. Next, samples were etched in a 5% HF solution to remove meteoric beryllium as well as anything else that readily dissolves in HF. The samples were run through a Frantz magnetic separator to remove magnetic minerals. Finally, LST heavy liquid columns were used to separate quartz from any remaining minerals.

Pure quartz from each sample was then rinsed in 1% HF, massed, and ~15g of quartz per sample was dissolved in concentrated HF and spiked with a ^{9}Be carrier of known concentration and mass. Blanks were created at this point to control for background ^{10}Be. Aliquots were separated at this point in case the samples need to be analyzed for aluminum.

The samples were then dried and fumed with $HClO_4$ to remove fluorides introduced by the HF. The samples were dried again and dissolved in HCl and ran through cation and anion columns. This purified and separated beryllium via ion exchange chromatography. Next beryllium was precipitated using H_2O_2 and NH_3 and oxidized to BeO at ~700 °C in a quartz crucible. Finally the samples were mixed with Nb metal and mounted to AMS targets and sent to the PRIME lab at Purdue University for AMS determination of ^{10}Be/^{9}Be ratios.

The measured isotope ratios were converted to ^{10}Be concentrations in quartz using the total Be in the samples and the sample weights, and concentrations of blanks were subtracted from the measured ratios to remove any background ^{10}Be. A local production rate from Twin Lakes was used with the CREp calculator to calculate ages. All relevant metadata for age calculation and laboratory processing are listed in **Appendix 2.**

^{36}Cl

The ^{36}Cl samples were processed at the PRIME Laboratory at Purdue University. The six boulder samples from the Walker Fan were crushed and sieved to obtain the 125 – 250μm size fraction.

Approximately 80 to 100g of each sample was subjected to a sequence of leaches with 10% HNO_3 TMG. Samples were then decanted and rinsed using deionized water and then dried. About

30 g of this leached sample was weighed and then spike with ^{35}Cl and before being dissolved in a HF/ HNO_3 TMG solution. Cl is isolated from the solution, through a sequence of precipitation of AgCl, by the addition of $AgNO_3$ and by passing the sample through anion columns. The final product is dried and target into copper tubes and analyzed at the PRIME Lab AMS to determine the $^{36}Cl/^{35}Cl$ ratio.

Aliquots of each sample analyzed for major elements and U and Th as well as gamma emission spectrometry of B and Gd, which is needed for the age calculations. Ages are calculated using the CRONUS calculator for ^{36}Cl.

Sample name	Date Collected	Lithology	Size of sampled rock	Depth of	Location		Elevation	Thickness	Shielding	^{10}Be concentration[a,f,g]	+/-	^{10}Be/^{9}Be[d,e]	Quartz[c]	Be carrier	Be carrier	CREP age		CREP age	
			a/b/c axes c-axis = height	Sample	latitude	longitude	above sea level	(cm)	factor	atoms/g SiO_2	atoms/g	x 10^{-13}	(g)	mass	concentration	LSD / ERA 40 / Lifton VDM 2016	1s error	Lal/ Stone	1s error
			(cm)	cm	(°N)	(°W)	(m)							(mg)	(µg/g)	(ka)	(ka)	(ka)	(ka)
Mason Valley																			
Upper Yerington fan surface																			
MVS1	19-Mar-2014	Granite	270/220/90	0	38.9669	119.2012	1424	1	1.0000	4.7235E+06	1.3340E+05	28.604 ± 0.807	14.5495	0.3506	1025.5	451.1	37.2	441.1	35.9
MVS2	19-Mar-2014	Granodiorite	100/85/25	0	38.9661	119.2019	1430	3	1.0000	1.0208E+06	2.4450E+04	10.593 ± 0.254	24.8750	0.3498	1025.5	93.3	6.6	91.1	6.7
MVS3	19-Mar-2014	Granodiorite	60/40/25	0	38.9660	119.2034	857	2	1.0000	1.2824E+06	4.1600E+04	7.020 ± 0.228	13.1176	0.3497	1025.5	183.5	13.5	175.8	13.7
MVS4	19-Mar-2014	Granodiorite	110/50/15	0	38.9653	119.2028	1431	2	1.0000	9.9780E+05	3.5100E+04	1.621 ± 0.075	3.9100	0.3505	1025.5	90.5	6.9	88.3	6.9
Depth Profile																			
M1 - Pit - 20	19-Mar-2014	Fanglomerate	Sand	20 ± 5	38.9669	119.2012	1425	5	1.0000	9.5590E+05	1.0420E+05	6.899 ± 0.075	17.2417	0.3494	1023.2	-	-	-	-
M1 - Pit - 40	19-Mar-2014	Fanglomerate	Sand	40 ± 5	38.9669	119.2012	1425	5	1.0000	1.2900E+05	1.1200E+05	7.847 ± 0.068	14.6023	0.3510	1023.2	-	-	-	-
M1 - Pit - 100	19-Mar-2014	Fanglomerate	Sand	100 ± 5	38.9669	119.2012	1425	5	1.0000	6.4340E+05	9.0800E+04	3.919 ± 0.055	14.5966	0.3504	1023.2	-	-	-	-
M1 - Pit - 160	19-Mar-2014	Fanglomerate	Sand	160 ± 5	38.9669	119.2012	1425	5	1.0000	3.0250E+05	6.7700E+04	2.241 ± 0.0502	17.7308	0.3500	1023.2	-	-	-	-
Smith Valley																			
Artesia Fan - oldest surface																			
SF1	20-Mar-2014	Granite	100/80/55	0	38.8908	119.4158	1494	1	0.9920	3.5660E+05	1.4100E+04	2.486 ± 0.098	16.7696	0.3510	1025.5	30.2	2.6	29.6	2.5
SF2	20-Mar-2014	Granodiorite	60/35/30	0	38.8909	119.4163	1497	4	0.9913	2.1390E+05	1.2000E+04	1.365 ± 0.077	15.3773	0.3515	1025.5	19.3	1.6	18.8	1.6
SF3	20-Mar-2014	Granite	70/60/20	0	38.8903	119.4158	1491	1	0.9923	4.7710E+05	0.0000E+00	1.427 ± 0.013	7.2053	0.3516	1025.5	40.4	2.8	39.7	2.8
Artesia Fan - oldest surface (Wesnousky and Caffee, 2011)																			
CWL-2	07-Aug-2008	Granite	65/50/25	0	38.8907	119.4150	1480	2	0.9922	3.7400E+05	1.9100E+04	-	-	-	-	32.5	3.0	31.7	2.9
CWL-3	07-Aug-2008	Granite	110/90/35	0	38.8907	119.4148	1470	2	0.9922	4.6900E+05	3.2400E+04	-	-	-	-	40.7	3.7	40.0	3.7
CWL-4	07-Aug-2008	Granite	80/70/60	0	38.8907	119.4148	1480	3	0.9933	7.9000E+05	4.2700E+04	-	-	-	-	69.9	6.3	68.2	6.1
Artesia Fan - younger surface																			
SF4	20-Mar-2014	Granite	170/100/30	0	38.8892	119.4164	1494	2	0.9929	2.4230E+05	1.9300E+04	3.147 ± 0.025	31.2170	0.3507	1025.5	21.3	2.0	20.8	2.0
SF5	20-Mar-2014	Granite	150/80/25	0	38.8892	119.4165	1494	1	0.9929	1.3260E+05	1.7500E+04	1.386 ± 0.018	25.1032	0.3511	1023.2	12.1	1.7	11.6	1.7
SF6	20-Mar-2014	Granite	185/140/65	0	38.8893	119.4171	1500	2	0.9917	4.0440E+05	1.3900E+04	3.331 ± 0.011	19.8597	0.3519	1025.5	34.7	2.9	34.0	2.8
Artesia Fan - lower younger surface																			
SF8	20-Mar-2014	Granite	220/165/30	0	38.8892	119.4149	1468	2	0.9950	3.1340E+05	2.1100E+04	3.899 ± 0.026	29.7777	0.3501	1023.2	27.4	2.6	26.8	2.5
SF9	20-Mar-2014	Granite	115/65/35	0	38.8892	119.4148	1472	2	0.9940	3.0460E+05	2.9500E+04	3.471 ± 0.034	27.3961	0.3515	1023.2	26.6	3.0	26.0	3.0
SF10	20-Mar-2014	Granite	95/60/25	0	38.8894	119.4145	1458	2	0.9939	1.4170E+05	2.1400E+04	1.273 ± 0.019	21.6136	0.3507	1025.5	13.4	2.1	12.8	2.0
SF11	20-Mar-2014	Granite	130/70/55	0	38.8888	119.4142	1450	5	0.9963	1.0450E+05	1.1700E+04	0.969 ± 0.011	22.2642	0.3502	1025.5	10.3	1.3	9.9	1.3

[a]Constant (time-invariant) local production rate based on Lal (1991) and Stone (2000). Nearby twin lakes production rate used.
[b]Constant (time-invariant) local production rate based on Heisinger et al. (2002a,b).
[c]A density of 2.7 g cm^{-3} , std elv/pressure conditions, and the KNSTD standard were used for all samples.
[d]Isotope ratios were normalized to ^{10}Be standards prepared by Nishiizumi et al. (2007) with a value of 2.85 x 10^{-12} and using a ^{10}Be half life of 1.36 x 10^{6} years.
[e]Uncertainties are reported at the 1σ confidence level. A denundation rate of 0 mm/a is used in the age calculation.
[g]Propagated uncertainities include error in the blank, carrier mass (1%), and counting statistics.
[h]Uncertainty is expressed as internal and external (in parenthesis).
[i]Propagated error in the model ages include a 6% uncertainty in the production rate of ^{10}Be and a 4% uncertainty in the ^{10}Be decay constant.
[j]Beryllium-10 model ages were calculated with the CREP online calculator, (Martin et al., 2016; http://crep.crpg.cnrs-nancy.fr/#/).

2. Data and results summary: ^{10}Be terrestrial cosmogenic geochronology.

3. Sample Photos

Mason Valley

MVS1

MVS2

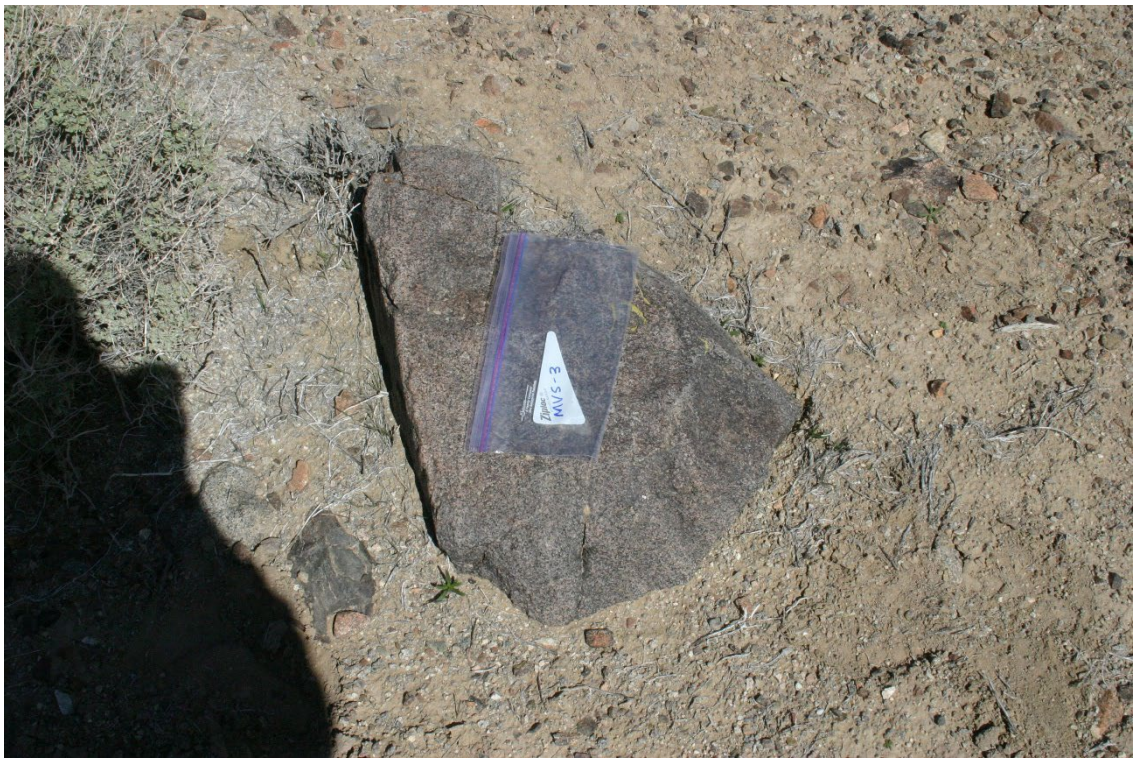

MVS3

MVS4

M1 Depth Profile

Smith Valley

SF1

SF2

SF3

SF4

SF5

SF6

SF8

SF9

SF10

SF11

Antelope Valley

CWL-5

CWL-6


CWL-7
Burial
Dimension
35x70
cm
breadth
30 cm
height
4 cm sample
Thickness

CWL-7

CWL-8

CWL-9

CWL-10

4. Profile Analyzer Python Code

This is a python code that analyzes topographic profiles of fault scarps to facilitate measurement of scarp heights. The profiles are generated using ArcGIS or similar and column headers must be removed. The code iterates through the profiles in a folder and for each profile the user selects two points for each of the hangingwall, footwall, and scarp. The profile fits a regression to each of these three surfaces between the two points selected. The three regressions are used as a simplifiation of each profile, and then the height of each scarp is measured between the hangingwall and footwall at the horizontal midpoint between the intersection of the fault scarp with the hangingwall and footwall. The code records this value then moves to the next profile.

```
#Profile Analyzer v0.1
#(c) 2019 Ian KD Pierce

import numpy
import os
import matplotlib.pyplot as plt
import matplotlib.axes
import csv
import pandas as pd

#set working directory, folder with profiles with headers stripped
wd='J:/School/Smith_Mason_Project/Figures/Wassuks/Wassuk_Profiles'
os.chdir(wd)

num_profs=71 #set number of profiles to be analyzed
ShowPlot=1 #set to 1 to show intermediate plots, 0 for not



#fig, ax = plt.subplots(nrows=num_profs, ncols=1)
#fig.set_size_inches(20,20)
#fig.subplots_adjust(left=4, bottom=4, right=5, top= 5, wspace=.5, hspace=.5)



#A=numpy.zeros((num_profs,11))
A = [[0] * 15 for i in range(num_profs)]
VO=[[0]*1 for i in range(num_profs)] #initialize Vert Offset stat bin
#Filenames=string[num_profs]

k=0
for file in os.listdir(wd): #load files
```

```
   if file.endswith(".txt"):
      print file
      prof_num= file
      A[k][0]= prof_num
      points = numpy.loadtxt(file, comments="#", delimiter="\t", unpack=False)
#initialize profiles

      x = points[:,0] #initialize all x values

      A[k][1]= x
      z = points[:,1] #initialize all z values
      A[k][2]= z
     # print(index.item((k,1)))



#define HW/FW/Fault with mouse
#HW
#determine index of HW initial point
      figc = plt.figure()
      axc = figc.add_subplot(111)
      axc.set_title('click on initial point of hangingwall; close when happy')
      line, = axc.plot(x, z, '', picker=5)
      def onpick(event):
         thisline = event.artist
         xdata = thisline.get_xdata()
         ydata=thisline.get_ydata()
         ind=event.ind
         points= x[ind],z[ind]
         print('Hw initial=', x[numpy.amin(ind)])
         global hwi
         hwi=numpy.amin(ind)
      figc.canvas.mpl_connect('pick_event', onpick)
      plt.show()

#determine index of HW final point
      figc = plt.figure()
      axc = figc.add_subplot(111)
      axc.set_title('click on final point of hangingwall; close when happy')
```

```
    line, = axc.plot(x, z, '', picker=5)
    def onpick(event):
      thisline = event.artist
      xdata = thisline.get_xdata()
      ydata=thisline.get_ydata()
      ind=event.ind
      points= x[ind],z[ind]
      print('HW Final =', x[numpy.amin(ind)])
      global hwf
      hwf=numpy.amin(ind)
    figc.canvas.mpl_connect('pick_event', onpick)
    plt.show()
    hwd=hwf-hwi


    hwx=x[hwi:hwf] #initializing variables
    hwz=z[hwi:hwf]

#FW
    #determine index of FW initial point
    figc = plt.figure()
    axc = figc.add_subplot(111)
    axc.set_title('click on initial point of footwall; close when happy')
    line, = axc.plot(x, z, '', picker=5)
    def onpick(event):
      thisline = event.artist
      xdata = thisline.get_xdata()
      ydata=thisline.get_ydata()
      ind=event.ind
      points= x[ind],z[ind]
      print('FW initial =', x[numpy.amin(ind)])
      global fwi
      fwi=numpy.amin(ind)
    figc.canvas.mpl_connect('pick_event', onpick)
    plt.show()

#determine index of FW final point
    figc = plt.figure()
```

```
    axc = figc.add_subplot(111)
    axc.set_title('click on final point of footwall; close when happy')
    line, = axc.plot(x, z, '', picker=5)
    def onpick(event):
      thisline = event.artist
      xdata = thisline.get_xdata()
      ydata=thisline.get_ydata()
      ind=event.ind
      points= x[ind],z[ind]
      print('FW Final =', x[numpy.amin(ind)])
      global fwf
      fwf=numpy.amin(ind)
    figc.canvas.mpl_connect('pick_event', onpick)
    plt.show()
    fwd=fwf-fwi


    fwx=x[fwi:fwf] #initializing variables
    fwz=z[fwi:fwf]
#Fault
    #determine index of Fault scarp initial point
    figc = plt.figure()
    axc = figc.add_subplot(111)
    axc.set_title('click on initial point of scarp; close when happy')
    line, = axc.plot(x, z, '', picker=5)
    def onpick(event):
      thisline = event.artist
      xdata = thisline.get_xdata()
      ydata=thisline.get_ydata()
      ind=event.ind
      points= x[ind],z[ind]
      print('Fault initial =', x[numpy.amin(ind)])
      global fi
      fi=numpy.amin(ind)
    figc.canvas.mpl_connect('pick_event', onpick)
    plt.show()

#determine index of fault final point
```

```
figc = plt.figure()
axc = figc.add_subplot(111)
axc.set_title('click on final point of scarp; close when happy')
line, = axc.plot(x, z, '', picker=5)
def onpick(event):
   thisline = event.artist
   xdata = thisline.get_xdata()
   ydata=thisline.get_ydata()
   ind=event.ind
   points= x[ind],z[ind]
   print('Scarp Final =', x[numpy.amin(ind)])
   global ff
   ff=numpy.amin(ind)
figc.canvas.mpl_connect('pick_event', onpick)
plt.show()
fd=ff-fi
fx=x[fi:ff] #initialize fault
fz=z[fi:ff]
#  fm=int((ff+fi)/2)#find average (midpoint) as integer of fault scarp points in index
form

print('width of fault =',x[ff]-x[fi])
#      print('fault midpoint index=',fm)
#      print('elevation of fault midpoint',z[fm])

# find least squares solutions


#least squares
fwA=numpy.vstack([fwx, numpy.ones(len(fwx))]).T
fwm,fwb=numpy.linalg.lstsq(fwA,fwz)[0]
A[k][3]= fwm
A[k][4]= fwb
print('equation for footwall: y=', fwm, 'x +', fwb)
print('slope of footwall', numpy.rad2deg(numpy.arctan(fwm)))
print('number of points used for fw regression:',fwd)

hwA=numpy.vstack([hwx, numpy.ones(len(hwx))]).T
```

```
hwm,hwb=numpy.linalg.lstsq(hwA,hwz)[0]
A[k][5]= hwm
A[k][6]= hwb
print('equation for hangingwall: y=', hwm, 'x +', hwb)
print('slope of hangingwall', numpy.rad2deg(numpy.arctan(hwm)))
print('number of points used for hw regression:',hwd)

print('regression skew=', numpy.rad2deg(numpy.arctan(hwm)-numpy.arctan(fw-
m)),'(degrees) - positive value indicates steeper hw than fw')#show positive or negative skew  of
regressions in degrees.

#fault least squares and intersection points (true start, true end) with HW/Fw regres-
sions
fA=numpy.vstack([fx, numpy.ones(len(fx))]).T
fslope,fb=numpy.linalg.lstsq(fA,fz)[0]
A[k][11]= fslope
A[k][12]= fb
#fault intersection points
xfhw=(fb-hwb)/(hwm-fslope) #intersection of hangingwall and fault x coordinate
xffw=(fb-fwb)/(fwm-fslope) #intersection of footwall and fault x coordinate
zfhw=hwm*xfhw+hwb #z coord of intersection
zffw=fwm*xffw+fwb #z coord of intersectio
A[k][13]=(xfhw, xffw)
A[k][14]=(zfhw, zffw)

#mid point of fault x coordinate
fm=(xfhw+xffw)/2 #this is in X values not indices as following equations are currently
A[k][10]= fm
print('fault midpoint x value is %.2f' %fm)
#solve for vert offset at midpoint, print
fwfm=fm*fwm+fwb #z value of footwall evaluated at fault midpoint
hwfm=fm*hwm+hwb #z value of hw evaluated at fault midpoint
A[k][8]= fwfm
A[k][9]= hwfm

fm_vo=(fwfm-hwfm) #fault midpoint vert offset
A[k][7]=fm_vo
print('vertical offset at midpoint of fault scarp is %f m' %fm_vo)
```

```
        #plot results
            if ShowPlot == 1:
                fig = plt.figure()
                ax = fig.add_subplot(111)
                ax.plot(x, z, 'k.', label=file)
                ax.plot(x, fwm*x + fwb, 'k-', label='Footwall Regression')
                ax.plot(x, hwm*x + hwb, 'k-', label='Hangingwall Regression')
                ax.plot(x, fslope*x +fb, 'r-', label='Footwall Regression')
                ax.vlines(x=fm, ymin=hwfm, ymax=fwfm) #plot vert offset line -> changed to x
format
                ax.annotate('%.2f m' %fm_vo, xy=(fm,(fwfm+hwfm)/2), xytext=(fm+numpy.
max(x)/8,(fwfm)),arrowprops=dict(facecolor='black', shrink=0.05),) #label Vert offset #chhanged
to x format
                #determine range of axes for setting VE

                #Vert exag was defined at top of program as VE
                ax.axis('equal')

                #set title / scale bars etc.
                ax.set_title('Profile %s' %prof_num)
            # ymin=hwfm, ymax=fwfm,
          #next find R^2 for each regression and print on figure; and plot vertical line between
regressions solved for midpoint of fault scarp (line plot? function? )

            k+=1



        #plot all profiles on same figure
         #initialize figure
        fig, axes = plt.subplots(nrows=num_profs, sharex=True)
        axS = axes.ravel()
        for i in range(num_profs):
            axS[i].plot(A[i][1], A[i][2], 'k.', label=file) #plot profile
            axS[i].plot(A[i][1], A[i][3]*A[i][1] + A[i][4], 'k-', label='Footwall Regression')
            axS[i].plot(A[i][1], A[i][5]*A[i][1] + A[i][6], 'k-', label='Hangingwall Regression')
            axS[i].plot(A[i][13], A[i][14], 'rx', linestyle='-', label='Fault Points')
            axS[i].vlines(x=A[i][10], ymin=A[i][9], ymax=A[i][8]) #plot vert offset line
            axS[i].annotate('%.2f m' %A[i][7], xy=(A[i][10],(A[i][8]+A[i][9])/2), xytext=(A[i]
```

```
[10]+numpy.max(A[i][1])/8,(A[i][8])),arrowprops=dict(facecolor='black', shrink=0.05),) #label
Vert offset
            axS[i].set_title('Profile %s' %A[i][0])
            axS[i].axis('equal')
            axS[i].set_ylabel('Elevation (m)')

            VO[i]=A[i][7]

        #VO Stats
        print('Minimum VO = %f' %min(VO))
        print('Maximum VO = %f' %max(VO))
        print('Average VO = %f' %numpy.mean(VO))
        print('Std VO = %f' %numpy.std(VO))

        plt.show()
```

5. Oxcal Inputs

In this section are listed the inputs used for the OxCal modeling. Copying each of these inputs into OxCal will produce the plots that were used in the analysis in chapter 1. The ages used are pulled from the respective technical reports and manuscripts that are listed in the text.

Antelope Valley:

```
Options()
 {
  BCAD=FALSE;
 };
 Plot()
 {
  Sequence("AntelopeV")
  {
   Boundary("Bottom");
   Date("PE");
   Phase("1")
   {
    R_Date("AV5-SGW-BULK", 5440, 30);
    R_Date("AV2-SGW-BULK", 1495, 25);
   };
   Date("MRE");
   Boundary("TOP");
  };
 };
```

C-Hill

```
Options()
 {
  BCAD=FALSE;
  PlusMinus=FALSE;
 };
 Plot()
 {
  Sequence("C-Hill")
  {
   Boundary("Bottom", base);
   Phase("1")
   {
    R_Date("CC-02", 7140, 400);
    R_Date("CH-5", 2590, 130);
   };
   Date("MRE");
   Phase("2")
   {
    R_Date("CH-3", 390, 40);
   };
   Boundary("Top");
  };
 };
```

Davis Creek Park

```
Options()
 {
  BCAD=FALSE;
  PlusMinus=FALSE;
 };
 Plot()
 {
  Sequence("DavisCreek1")
  {
   Boundary("Bottom", base);
   Phase("1")
   {
    R_Date("DCP1-1A", 1780, 60);
    R_Date("DCP1-25A", 1770, 60);
   };
   Date("PE");
   Phase("2")
   {
    R_Date("DCP1-7C", 2070, 60);
   };
   Date("MRE");
   Phase("3")
   {
    R_Date("DCP1-3", 50, 40);
   };
   Boundary("Top");
  };
 };
```

East Carson Valley

```
Options()
 {
  BCAD=FALSE;
  PlusMinus=FALSE;
 };
 Plot()
 {
  Sequence("ECVFZ")
  {
   Boundary("Bottom", base);
   Phase("1")
   {
    R_Date("T2-RC4", 870, 70);
   };
   Date("MRE");
   Phase("2")
   {
    R_Date("T2-RC3", 650, 80);
   };
   Boundary("Top");
  };
```

Fay Canyon

```
Options()
 {
  BCAD=FALSE;
  PlusMinus=FALSE;
 };
 Plot()
 {
  Sequence("FayCanyon")
  {
   Boundary("Base",base);
   Phase("Oldest")
   {
    R_Date("FL1-4", 2360, 30);
   };
   Date("PE");
   Phase("Intermediate")
   {
    R_Date("FL1-31", 2055, 30);
    R_Date("FL1-22", 2050, 30);
    R_Date("FL1-6", 1990, 30);
    R_Date("FL1-32", 1885, 30);
    R_Date("FL1-25", 1670, 30);
    R_Date("FL1-41", 1605, 35);
    R_Date("FL2-9", 1360, 35);
    R_Date("FL2-1", 465, 35);
    R_Date("FL2-3", 405, 30);
   };
   Date("MRE");
   Phase("TOP")
   {
    R_Date("FL2-12", 430, 30);
    R_Date("FL2-11", 380, 30);
    R_Date("FL2-10", 380, 30);
    R_Date("FL2-4", 320, 30);
   };
   Boundary("Top");
  };
 };
```

Jacks Valley

```
Options()
 {
  BCAD=FALSE;
  PlusMinus=FALSE;
 };
 Plot()
 {
  Sequence("JacksValley")
  {
   Boundary("Base", base);
   Date("PE");
   Phase("1")
   {
    R_Date("JV-1-1", 2100, 125);
    R_Date("JV-4-4", 1760, 120);
    R_Date("JV-6-2", 1270, 105);
    R_Date("JV-8-3", 870, 95);
    R_Date("JV-8-2", 755, 100);
    R_Date("JV-8-4", 525, 120);
   };
   Date("PE");
   Phase("2")
   {
    R_Date("JV-9-3", 580, 110);
    R_Date("JV-9-2", 390, 115);
   };
   Boundary("Top");
  };
 };
```

Kings Canyon

```
Options()
 {
  BCAD=FALSE;
 };
 Plot()
 {
  Sequence("KingsCanyon_T2")
  {
   Boundary("Base", base);
   Phase("1")
   {
    R_Date("KC2-R1", 5540, 35);
    C_Date("KC2-L1", 5170, 220);
    C_Date("KC2-L2", 3490, 400);
   };
   Date("MRE");
   Phase("2")
   {
    C_Date("KC2-L3", 1700, 120);
   };
   Boundary("Top");
  };
  Sequence("KingsCanyon_T3")
  {
   Boundary("Base", base);
   Phase("1")
   {
    C_Date("KC3-L1", 5310, 290);
    C_Date("KC3-L2", 4840, 420);
   };
   Date("PE2");
   Phase("2")
   {
    C_Date("KC3-L3", 3120, 180);
    C_Date("KC3-L4", 1920, 60);
    C_Date("KC3-L5", 1680, 70);
   };
   Date("PE1");
   Phase("3")
   {
    C_Date("KC3-L6", 1660, 80);
    R_Date("KC3-R4", 1450, 55);
    R_Date("KC3-R1", 1630, 25);
   };
   Date("MRE");
   Phase("4")
   {
    R_Date("KC3-R3", 1550, 40);
```

```
  C_Date("KC3-L7", 1440, 50);
  R_Date("KC3-R2", 855, 25);
 };
 Boundary("Top");
};
};
```

Mt. Rose Fan

```
Options()
 {
  BCAD=FALSE;
 };
 Plot()
 {
  Sequence(“MRF”)
  {
   Boundary(“Bottom”, base);
   Phase(“1”)
   {
    R_Date(“WC-T1”, 910, 70);
   };
   Date(“MRE”);
   Phase(“2”)
   {
    R_Date(“CRT-12”, 930, 60);
    R_Date(“CRT-15”, 1060, 70);
   };
   Boundary(“Top”);
  };
 };
```

Smith Valley

```
Plot()
 {
  Sequence("1")
  {
   Boundary("Base");
   Phase("UC2")
   {
    R_Date("UC2", 5176, 130);
   };
   Date("MRE");
   Phase("UC7")
   {
    R_Date("UC7", 3530, 82);
   };
   Boundary("top");
  };
 };
```

Sturgis

```
Options()
 {
  BCAD=FALSE;
 };
 Plot()
 {
  Sequence("Sturgis")
  {
   Boundary("Base", base);
   Phase("1")
   {
    R_Date("ST-7", 3095, 155);
    R_Date("ST-14", 2290, 110);
   };
   Date("PE");
   Phase("2")
   {
    R_Date("ST-18", 1965, 105);
    R_Date("ST-16", 1815, 90);
    R_Date("ST-20", 1370, 120);
   };
   Date("MRE");
   Phase("3")
   {
    R_Date("ST-3", 1025, 315);
    R_Date("ST-5", 580, 115);
   };
   Boundary("Top");
  };
 };
```

Walleys

```
Options()
 {
  BCAD=FALSE;
 };
 Plot()
 {
  Sequence(“Walleys”)
  {
   Boundary(“Base”, base);
   Phase(“1”)
   {
    R_Date(“W-3”, 295, 175);
    R_Date(“W-1”, 225, 90);
   };
   Date(“PE”);
   Date(“MRE”);
   Boundary(“Top”);
  };
 };
```